

**MICROFABRICATION OF ORGANIC ELECTRONIC DEVICES:
ORGANIC PHOTOVOLTAIC MODULE WITH HIGH TOTAL-AREA
EFFICIENCY**

A Dissertation
Presented to
The Academic Faculty

By

Amir Dindar

In Partial Fulfillment
Of the Requirements for the Degree
Doctor of Philosophy in the
School of Electrical and Computer Engineering

Georgia Institute of Technology
May 2015

Copyright © Amir Dindar 2015

**MICROFABRICATION OF ORGANIC ELECTRONIC DEVICES:
ORGANIC PHOTOVOLTAIC MODULE WITH HIGH TOTAL-AREA
EFFICIENCY**

Approved by:

Dr. Bernard Kippelen, Advisor
School of Electrical and Computer
Engineering
Georgia Institute of Technology

Dr. David S. Citrin
School of Electrical and Computer
Engineering
Georgia Institute of Technology

Dr. Oliver Brand
School of Electrical and Computer
Engineering
Georgia Institute of Technology

Dr. Jeffery A. Davis
School of Electrical and Computer
Engineering
Georgia Institute of Technology

Dr. Samuel Graham
School of Mechanical Engineering
Georgia Institute of Technology

Date Approved: March 30, 2015

Dedicated to:

All who pursue their educations despite all the hardships of life.

ACKNOWLEDGEMENT

This work is a result of an invaluable teamwork, collaboration and generous support from my colleagues, friends and family. At first I would like to express my gratitude to my advisor Dr. Kippelen for his guidance, encouragement, and support that he provided me in this research. His high professional and scientific standards have had great impact in shaping my academic studies, as well as my personal and professional perspective in life, and for that I am very thankful to him.

I would also like to thank Dr. Oliver Brand, Dr. Samuel Graham, Dr. David S. Citrin and Dr. Jeffery A. Davis for their valuable time and effective participation in my PhD committee and for reviewing and evaluating this work.

I am very much indebted to many of the members in Kippelen Research Group. At first I would like to extend my special thanks to Dr. Canek Fuentes-Hernandez for his mentorship, his professionalism, and more importantly for his friendship. I am very thankful to Dr. Kim Jungbae, and Dr. Shree Prakash Tiwari for being my first trainers in the group and for making me familiar with fundamentals of several fabrication processes and experimental setups. I am also very grateful to Dr. Mathieu Fenoll for his friendship and for teaching me the inkjet printing and ink formulation processing. I must thank Dr. Yinhua Zhou for his original contribution to this work.

I also wish to thank all my past and present colleague for their assistance and support in last few years: Dr. Jae Won Shim, Talha M. Khan, Dr. Do Kyung Hwang, Dr. Hyeunseok Cheun, Dr. Seungkeun Choi, Dr. Raghunath Dasari, Dr. Asha Sharma,

Cheng-Yin Wang, Dr. James Hsu, Michael Gaj, and Vladimir Kolesov, Dr. Anuradha Bulusu, and Dr. Emily Blackburn.

Main part of this work has been done in The Institute for Electronics and Nanotechnology (IEN) and I would also like to extend my gratitude to the staff and management of IEN especially Mr. Gary Spinner for all the help and endless support.

This work was funded by Office of Naval Research (ONR), Bay Area Photovoltaic Consortium (BAPVC), Center for Interface Science: Solar Electric Materials (CIS:SEM) an Energy Frontier Research Center (EFRC) under Department of Energy, and the Technological Innovation: Generating Economic Results (TI:GER[®]) program in Georgia Institute of Technology school of business.

Last but not least, my deepest gratitude goes to my family for their endless love and support. Their presence and excitement in every single day and in all the ups and downs of this journey provided me with an invaluable and empowering support that energized and motivated me throughout my studies. My special thanks go to my parents for all the hardship they endured during all these years to give me enough confidence to pursue my dreams. I must also thank my grandparents for inspiring me with their kindness toward me for many years. At last I would like to thank all my friends who believed in me and always encouraged me.

TABLE OF CONTENTS

ACKNOWLEDGEMENT	iv
LIST OF TABLES	ix
LIST OF FIGURES	xi
LIST OF SYMBOLS AND ABBREVIATIONS	xvii
SUMMARY	xx
CHAPTER 1: INTRODUCTION.....	1
1.1 Energy Consumption and Sustainability.....	1
1.2 Renewable Energies.....	1
1.3 Photovoltaics.....	2
1.3.1 Solar Energy.....	4
1.3.2 Solar Cell Operation	5
1.3.3 Equivalent Circuit	6
1.3.4 Performance Metrics.....	8
1.3.5 Existing Technologies.....	10
1.4 Organic Photovoltaics.....	15
1.4.1 Evolution of OPV	16
1.4.2 Organic Semiconductors.....	18
1.4.3 OPV Cells	28
1.4.4 OPV Operation.....	29

1.4.5	OPV Device Structures: Conventional vs. Inverted	31
CHAPTER 2:	LARGE AREA PV SYSTEMS: SOLAR CELL MODULES	35
2.1	Early Photovoltaic Modules.....	37
2.2	Conventional Thin-film PV Modules: The Stripe Geometry	37
2.2.1	Major Challenges	39
2.3	OPV Module.....	43
2.3.1	OPV Module in Literature	43
2.3.2	Scalable Fabrication: Printed Electronics	48
CHAPTER 3:	ORGANIC PHOTOVOLTAIC MODULE.....	54
3.1	Proposed OPV Module	54
3.2	Geometry and Operation.....	54
3.3	Losses in New Geometry	58
3.4	Module Efficiency Definitions	61
CHAPTER 4:	OPV MODULE MICROFABRICATION	62
4.1	Trial 1: OPV Module: Proof of Concept	62
4.1.1	Microfabrication of Module.....	63
4.1.2	Results and Discussion	65
4.2	Trial 2: OPV Module: Photolithography	66
4.2.1	Photolithography Recipe for OSCoR 2312 Photoresist.....	69
4.2.2	Patterning PEDOT:PSS Layer	70

4.2.3	PEIE Layer and Contamination Issues	73
4.3	Trial 3: OPV Module: Solution Processing	76
4.3.1	Single Cell Fabrication	77
4.3.2	Four-Cell Module.....	80
4.4	Trial 4: OPV Module: Inkjet Printing.....	83
4.4.1	PEDOT Ink Formulation.....	83
4.4.2	OPV Module with Printed PEDOT:PSS Layer	89
4.4.3	Discussion	95
4.5	Trial 5: OPV Module: Reactive Ion Etching (RIE)	96
4.5.1	Single Cell Fabrication	98
4.5.2	Four-Cell Module.....	100
4.5.3	Eight-Cell Module	107
4.5.4	Discussion.....	109
CHAPTER 5: CONCLUSION		112
5.1	Recommendations for Future Work	113
5.1.1	Design: Reducing the Gap Size	113
5.1.2	Material: Other Photoactive Materials.....	113
5.1.3	Material: Other Interlayers.....	114
5.1.4	Fabrication Method: Other Printing Methods.....	114
REFERENCES		116

LIST OF TABLES

Table 1: Chronological list of pioneer work in development of photovoltaic technology [14].....	3
Table 2: Confirmed terrestrial single cell efficiencies measured under global AM1.5 spectrum (1000W/m ²) at 25°C.....	11
Table 3: The highest PCE values for OPV technology reported in literature until 2013.	17
Table 4: Work function of conducting materials with and without polymer modifiers, as independently measured by Kelvin probe in air and by UPS. Empty cells indicate no measurement for the corresponding sample [60].....	34
Table 5: PV performance of the four-cell module and its inverted (ITO/PEIE/P3HT:ICBA/MoOx/Ag) and conventional (ITO/MoOx/P3HT:ICBA/PEIE/Ag) sub-cells under AM 1.5 100 mW/cm ² illumination.	66
Table 6: Kelvin probe measurement results on three PEDOT:PSS films. The results indicates that the contaminations due to photoresist residues eliminates the effect of PEIE	75
Table 7: PV performance of inverted and conventional single cells under AM 1.5 100 mW/cm ² illumination (averaged over 4 devices).....	79
Table 8: Photovoltaic performance of solution processed four-cell module, and its inverted and conventional sub-cells, under AM 1.5 100 mW/cm ² illumination.	82
Table 9: List of different modified PEDOT:PSS PH1000 solutions. Water was the main additive to decrease the viscosity, while the surfactants were used to reduce the surface tension, and solvents were used to improve the conductivity of PEDOT:PSS.....	87

Table 10: Photovoltaic performance of the four-cell module with its inverted and conventional sub-cells (printed PEDOT:PSS interlayer).....	94
Table 11: Photovoltaic performance of inverted and conventional single cells under AM 1.5 100 mW/cm ² illumination. (averaged over 6 devices).....	99
Table 12: PV performance of the four-cell module and its inverted and conventional sub-cells under AM 1.5 100 mW/cm ² illumination.....	106
Table 13: PV performance of the eight-cell module and its inverted and conventional sub-cells under AM 1.5 100 mW/cm ² illumination.....	109
Table 14: Performance comparison between current state-of-the-art OPV modules.....	110

LIST OF FIGURES

Figure 2-1: Spectral distribution of sunlight at AM0 and at AM1.5 (i.e., sun at 48.19° zenith angle) radiation..... 4

Figure 2-2: Simplified principle operation of an inorganic solar cell, a) photo-generation of electron-hole pairs inside the depletion region, b) energy level diagram (non-equilibrium) showing the generation of electron-hole pairs inside the space-charge region. Charge carriers then swept away toward their favorable energy levels and accumulate at the electrodes. Small arrows represent the direction of free charges movement..... 6

Figure 2-3: a) Equivalent circuit of a solar cells with total active area equal to A, b) the J - V characteristic of a solar cell at dark and under illumination [18]..... 7

Figure 2-4: Power and current density as a function of voltage for a solar cell under illumination. 8

Figure 2-5: Existing PV technologies and their corresponding efficiency values (from NREL [20]) 10

Figure 2-6: LCOE of different technologies 12

Figure 2-7: Representation of s and p atomic orbitals. 19

Figure 2-8: Representation of $2s$ and $2p$ orbital hybridization in methane..... 20

Figure 2-9: Schematic of σ -bond and π -bond in ethylene (C_2H_4). 21

Figure 2-10: Schematic of σ -bond and π -bond in conjugated polymer polyacetylene (PA)..... 22

Figure 2-11: Schematic representation of exciton formation in (a) perfectly ordered crystalline inorganic material, and (b) in disordered organic material. 25

Figure 2-12: Simplified energy diagram of a donor/acceptor interface.	26
Figure 2-13: Chemical structures of commonly used (a) donor and (b) acceptors organic semiconductors in PV.	27
Figure 2-14: Schematic of typical OPV cell structures: (a) bilayer cell in which the acceptor and donor materials are deposited separately, and (b) bulk hetero-junction cell in which the acceptor and donor materials are mixed and deposit together.	28
Figure 2-15: Energy diagram of a typical OPV cell composed of: hole collecting electrode (HCE), donor organic semiconductor, acceptor organic semiconductor, and electron collecting electrode (ECE). The vacuum is the reference to measure the ionization potential (IP) of the donor material and the electron affinity (EA) of acceptor material.	29
Figure 2-16: OPV Operation: Starting from top left: Photo absorption leads to an exciton formation (shown only in donor side), then exciton migrates toward the donor/acceptor interface. At the interface electron and hole dissociates and then each migrates toward the corresponding electrodes.	30
Figure 2-17: Two typical geometries of an OPV cells: a) conventional, b) inverted	32
Figure 2-18: Polyethylenimine ethoxylated (PEIE): (a) the chemical structure, (b) the shift in vacuum due to the dipole moment created by PEIE molecule	33
Figure 3-1: Transition from a single solar cell to a solar cell panel.....	35
Figure 3-2: Production process for typical commercial crystalline silicon solar cells. ...	36
Figure 3-3: Schematic of a PV module with “stripe” geometry: a) Three dimensional representation of the unit cell, b) Shading length vs active length, c) Circuit diagram of the module.....	38
Figure 3-4: Effect of the AR_S on organic photovoltaic performance [70].....	41
Figure 3-5: Schematic of the OPV module made by Yoo et al., a) top and side views, b) Output characteristic of the module consisting of a series connection of N individual cells (N = 1, 2, 3, and 4) measured in air under illumination (AM1.5 G, 85 mW/cm ²) [76]....	44

Figure 3-6: The <i>I-V</i> characteristics of “wrap through” singles cells reported by Zimmermann et al.	45
Figure 3-7: Module reported by Lewis at al., a) <i>J-V</i> characteristic of an array of 9 cells connected in series, b) schematic of the interdigitated array of 20 single cells, and c) picture of fabricated array [80].	46
Figure 3-8: Linear pixel array of OPV module reported by Liao et. al, a) schematic of two linear pixel arrays made of 5 and 8 cells with areas of 4 and 1 mm ² respectively, and b) <i>I-V</i> characteristics of the 5 cell array.	47
Figure 3-9: Illustration of screen printing processes: (a) flat-bed, and (b) rotary techniques.	50
Figure 3-10: Illustration of gravure printing method.	51
Figure 3-11: Illustration of inkjet printing techniques: (a) drop-on-demand, and (b) continuous techniques.	52
Figure 4-1: Schematic of the proposed OPV-module: a) Three dimensional representation of a 4-cell module, b) Active length vs. gap length of the unit cell, c) Circuit diagram of the OPV-module.	55
Figure 4-2: Schematic of a two different PV modules: a) conventional “stripe” geometry and b) the alternative geometry consisting of adjacent solar cells with alternating polarities.	56
Figure 4-3: Schematic of the proposed new geometry as it is planned for fabrication....	57
Figure 4-4: Schematic comparison between (a) module with stripe geometry, and (b) module with new geometry. In new geometry the shading losses become independent of the active area length and the interconnection losses are completely avoided.	58
Figure 4-5: Schematic of the module and its sub-cell.	59
Figure 5-1: The proof of concept module using thermally evaporated MoO _x (through shadow mask) and spin-coated PEIE (patterned using PDMS film)	62

Figure 5-2: <i>J-V</i> characteristic of the proof-of-concept four-cell module under AM 1.5 100 mW/cm ² illumination. The inset is a picture of the module.	65
Figure 5-3: Chemical structure of 1,1,1,2,3,3-Hexafluoro-4-(1,1,2,3,3,3-Hexafluoropropoxy) pentane.	67
Figure 5-4: (a) The cross sectional schematic of the module structure designed for photolithography, and (b) the top view of the design.	68
Figure 5-5: (a) Lift-off process for patterning PEDOT:PSS film using OSCoR 2312 Photoresist and (b) its final result.	71
Figure 5-6: (a) dry-etching process for patterning PEDOT:PSS film using OSCoR 2312 Photoresist and (b) its final result. The blue stripes (pattern on the left) are PEDOT films on top of ITO, and the yellow stripes (patterns on the right) are ITO contact lines.	73
Figure 5-7: XPS analysis of PEDOT/PEIE film exposed to fluorinated photoresist. The strong fluorine 1s peak is an indication of severe photoresist contamination.	75
Figure 5-8: Schematic of the new geometry and its constituent inverted and conventional sub-cells for solution processing.	77
Figure 5-9: <i>J-V</i> characteristic of (a) an inverted single cell (glass/ITO/PEIE/P3HT:ICBA/PEDOT:PSS/Al) and (b) a conventional single cell (glass/ITO/PEDOT:PSS/P3HT:ICBA/PEIE/Al) in the dark and under AM 1.5 100 mW/cm ² illumination.	80
Figure 5-10: <i>J-V</i> characteristic of the solution processed four-cell module the in dark and under AM 1.5 100 mW/cm ² illumination.	82
Figure 5-11: Schematic of (a) the morphology of a typical PEDOT:PSS thin-film, where PEDOT particles are shown as solid short lines, surrounded by PSS-rich surface layers (dashed lines), and (b) the chemical structure of PEDOT and PSS chains. (adopted from [101]).	84
Figure 5-12: Surface tension vs. viscosity of water, PEDOT:PSS PH1000 and the acceptable range of these values for Dimatix DMP-2831inkjet printer.	86

Figure 5-13: Viscosity vs. shear rate for a number of PEDOT:PSS formulations for Dimatix DMP-2831 inkjet printer.....	88
Figure 5-14: An example of a printed PEDOT:PSS pattern on Polyethersulfone (PES) substrate using in-house formulated PEDOT:PSS ink and Dimatix DMP-2831 inkjet printer.....	89
Figure 5-15: Schematic of the modified design of a four-cell module with inkjet printed PEDOT:PSS interlayers, along with its constituent inverted and conventional sub-cells.....	90
Figure 5-16: Picture of the four-cell module with printed PEDOT:PSS interlayers on glass.....	93
Figure 5-17: <i>J-V</i> characteristics of the printed four-cell module under AM 1.5 100 mW/cm ² illumination. The active area of the module is 400 mm ² and the total area is 440 mm ² (four 5 mm by 20 mm cells, with 500 μm gaps between them).....	94
Figure 5-18: Schematic of the new geometry four-cell module and its inverted and conventional sub-cells for scalable fabrication.....	97
Figure 5-19: <i>J-V</i> characteristic of (a) an inverted single solar cell (glass/ITO/PEIE/P3HT:ICBA/ PEDOT:PSS/Ag) and (b) a conventional solar cell (glass/ITO/PEDOT:PSS/P3HT:ICBA/PEIE/PEDOT:PSS/Ag) in the dark and under AM 1.5 100 mW/cm ² illumination.....	99
Figure 5-20: Illustration of major fabrication steps for four-cell and eight-cell OPV module.....	102
Figure 5-21: Picture of the four-cell module fabricated on a glass substrate.	105
Figure 5-22: (a) <i>J-V</i> characteristics of a four-cell module in the dark and under AM 1.5 100 mW/cm ² illumination. Inset displays the <i>J-V</i> characteristics of the module in the dark and under AM1.5 100 mW/cm ² illumination in semi logarithmic scale. (b) <i>I-V</i> characteristics of inverted and conventional sub-cells and the four-cell module under illumination. The active area of the module is 80 mm ² and the total area is 90 mm ² (four 2 mm by 10 mm cells, with 500 μm gaps between them)	106

Figure 5-23: Picture of the eight-cell module fabricated on a glass substrate. 107

Figure 5-24: (a) *J-V* characteristics of an eight-cell module in the dark and under AM 1.5 100 mW/cm² illumination. Inset displays the *J-V* characteristics of the module in the dark and under AM1.5 100 mW/cm² illumination in semi logarithmic scale. (b) *I-V* characteristics of inverted and conventional sub-cells and the eight-cell module under illumination. The active area of the module is 160 mm² and the total area is 180 mm² (eight 2 mm by 10 mm cells, with 500 μm gaps between them) 108

LIST OF SYMBOLS AND ABBREVIATIONS

α -Si	Amorphous silicon
AFM	Atomic force microscopy
ALD	Atomic layer deposition
AM	Air mass
CdTe	Cadmium telluride
CIGS	Copper indium gallium arsenide
CV	Cyclic voltammetry
DCB	1, 2-dichlorobenzene
DMSO	Dimethyl sulfoxide
DSDC	Dye-sensitized solar cell
EA	Electron affinity
ECE	Electron collecting electrode
EPBT	Energy payback time
FF	Fill factor
GaAs	Gallium arsenide
GHG	Greenhouse gas

HCE	Hole collecting electrode
HOMO	Highest occupied molecular orbital
ICBA	Indene-C ₆₀ bis-adduct
IE	Ionization energy
IPES	Inverse photoemission spectroscopy
ITO	Indium tin oxide
J_{ph}	Photocurrent density
J_{sc}	Short circuit current density
LCOE	Levelized cost of energy
LUMO	Lowest unoccupied molecular orbital
MO	Molecular orbital
MoO _x	Molybdenum oxide
OPV	Organic photovoltaics
OSC	Organic solar cell
P3HT	Poly(3-hexylthiophene-2,5-diyl)
PA	Polyacetylene
PCE	Power conversion efficiency
PDMS	Polydimethylsiloxane
PDTSTTz	Dithieno[3,2-b:2',3'-d]silole (DTS)-dithienylthiazolo[5,4- d]thiazole (TTz)
PEDOT:PSS	Poly(3,4-ethylenedioxythiophene) polystyrene sulfonate

PEI	Polyethylenimine
PEIE	Polyethylenimine ethoxylated
P_{max}	Maximum power density
PV	Photovoltaics
UPS	Ultraviolet photoelectron spectroscopy
UV-Vis	Ultraviolet-visible
V_{oc}	Open circuit voltage
WF	Work function
XPS	X-ray photoelectron spectroscopy

SUMMARY

In the quest for finding renewable and sustainable sources of energy, photovoltaics (PV) is potentially one of the best renewable energy technology due to the abundance of solar energy and the potential for PV to have the lowest environmental impact when compared with other energy sources. Amongst existing and emerging PV technologies, and despite currently achieving power conversion efficiency (PCE) values that are lower than other thin-film PV technologies, organic PV (OPV) is very attractive because estimates suggest that a mature OPV technology could yield the lowest energy payback-times (EPBT) and greenhouse gas (GHG) emissions of all other renewable energy sources.

Transformation of OPV from laboratory into economically feasible products, requires fabrication of modules. Achieving module-level PCE values that are comparable to values displayed by single cells is a critical challenge due to the impact that module-level PCE values have in reducing the levelized cost of energy (LCOE) of photovoltaic (PV) technologies, and consequently on the economic viability of solar energy.

A current paradigm of PV technology is that the PCE values displayed by commercial PV modules are typically smaller than 80% of the values displayed by single PV cells. This problem is particularly severe in thin-film PV technologies where challenging tradeoff exists between minimizing PCE losses at the module-level and increased fabrication cost due to the need for cost-intensive techniques such as lithography, laser patterning, etc., that seldom can be scaled-up economically to large areas. This tradeoff

arises as a direct consequence of the conventional configuration used to connect PV cells in series, the so-called “stripe geometry.” Modules with this configuration inherit two major loss mechanisms: shading and parasitic resistance losses.

In this dissertation, a new module geometry is proposed. This module geometry has the potential to alleviate the intrinsic tradeoffs introduced by use of the stripe-geometry and has the potential to be adapted to scalable and cost-efficient all-additive fabrication processes since it avoids patterning of the active layer. Developing the necessary techniques to pattern functional organic materials for fabrication of this novel OPV module and performing theoretical and experimental validation of the proposed structure through modeling and fabrication, are the primary objectives of this dissertation. The realization of this new novel module architecture relies on developing the ability to fabricate OPV cells with opposite polarities that display comparable performance. The selection of the right interlayers to tune the work function of electrodes to enable electrons and holes to be collected on adjacent areas of one electrode was a critical component towards this goal.

The proposed OPV module geometry enabled the demonstration of polymeric photovoltaic modules with unprecedented performance. 4-cell and 8-cell modules display fill-factor (FF) and PCE values that are comparable to the values displayed by constituent sub-cells. Fabrication of an inkjet printed OPV module is also demonstrated, representing a significant step towards the all-additive fabrication of OPV modules.

CHAPTER 1: INTRODUCTION

1.1 Energy Consumption and Sustainability

Environmental sustainability and growing global demand for energy, due to socio-economic developments, are among the most challenging problems of this century [1, 2]. According to the U.S. Energy Information Administration (EIA), the world energy consumption will grow by 56% by 2040 (from 520 to 820 quadrillion Btu) [3]. These estimations are based on certain assumptions, such as continuous growth in world economy, etc. that might not hold in a long term; nonetheless, fossil-based resources (oil, coal, natural gas) are today's main sources of energy in all major economies, as well as developing countries around the world.

Fossil-based energy sources are non-renewable and limited natural resources, the continuous growth in energy demand has been raising concerns about the depletion of these conventional sources of energy, accelerating the need for finding alternative renewable sources of energy to satisfy the growing global demand. In addition, the use of fossil-based energy sources has resulted in the emission of unsustainable levels of greenhouse gases into the atmosphere leading to considerable impacts upon the environment by affecting the climate, water, land and wildlife [4-6].

1.2 Renewable Energies

The non-renewable nature of fossil-based energy sources, their increasing high-cost, and concerns over their environmental impact, have created a global momentum to find

environmental friendly sources of energy. In this regard, there has been an intense effort to find efficient ways to utilize environmentally sustainable sources of energy, known as “renewable”. These renewable resources of energy are those that can be replenished by nature: sunlight, wind, and geothermal heat are the most widely used examples of such resources. “Renewable energy technologies” are the technologies that generate useful and reliable forms of energy – mainly electricity – from renewable resources.

Shifting from traditional fossil-based energies to renewable alternatives will help us meet the goals of reducing greenhouse gas emissions, and ensuring reliable and efficient energy sources for the future [7].

1.3 Photovoltaics

Quest to find viable alternative sources of energy has made photovoltaics (PV) potentially one of the best renewable energy technologies [1, 8-10]. Photovoltaics is the direct conversion of solar radiative energy into electricity, using semiconducting materials.

A.E. Becquerel is credited for the discovery of the photovoltaic effect in 1839 as result of his studies on liquid electrolytes [11]. This discovery attracted a lot of attention, and 40 years later, in 1876, the first solid-state photovoltaic device based on selenium was reported by W. Adams and R. Day. Later in 1883, C. Fritts made one of the first large area selenium-based solar cells with a PCE of about 1%. Although all the early work in photovoltaics were essential in the overall development of the photovoltaic field, it was not until 1954 when D.M. Chapin and colleagues at Bell labs reported the invention of the first practical silicon-based single p-n junction solar cell with a PCE of

about 6% [12]; significantly improving the outlook of photovoltaics as a feasible technology [13]. Table 1 summarizes major pioneer work in early development of the photovoltaic technology [14].

Table 1: Chronological list of pioneer work in development of photovoltaic technology [14]

Scientist and innovation	Year
Becquerel discovers the photovoltaic effect	1839
Adams and Day notice photovoltaic effect in selenium	1876
Planck claims the quantum nature of light	1900
Wilson proposes Quantum theory of solids	1930
Mott and Schottky develop the theory of solid-state rectifier (diode)	1940
Bardeen, Brattain and Schockley invent the transistor	1949
Charpin, Fuller and Pearson announce 6% efficient silicon solar cell	1954
Reynolds et al. highlight solar cell based on cadmium sulphide	1954
First use of solar cells on an orbiting satellite (Vanguard 1)	1958

Compare to fossil-based resources, solar energy provides compelling environmental benefits. Solar energy is abundant (potentially infinite), safe, free, and the photovoltaic process used to convert light into electricity causes no direct water or air pollution during the conversion process.

In recent years, the global PV capacity has been steadily increasing, with cumulative installed PVs reported to be 134 GW globally, and an average growth of 38 GW just in year 2013 [2]. Therefore, alongside other renewable energy technologies, photovoltaic technology is expected to have a considerable share in the future global energy portfolio.

1.3.1 Solar Energy

The source of sun's energy is a continuous nuclear fusion reaction at its center [15] which heats the surface of sun close to 6000 K. This hot surface, according to Plank's black body radiation law, radiates a continuous spectrum of electromagnetic radiation (see Figure 1-1). The radiant power per unit area perpendicular to the direction of the sun outside the earth's atmosphere and at the mean earth-sun distance is a constant having a value of 1.353 kW/m^2 and referred to as "solar constant" or "air mass zero" (AM0) [15]. As the sun radiation passes through the atmosphere, it gets attenuated due to scattering and absorption and its intensity and spectral composition changes.

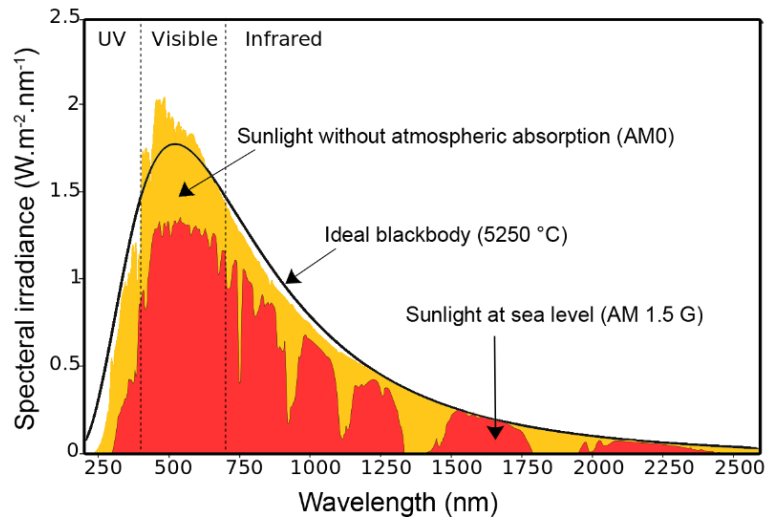


Figure 1-1: Spectral distribution of sunlight at AM0 and at AM1.5 (i.e., sun at 48.19° zenith angle) radiation

The magnitude of this attenuation depends on how far sun light travels through the atmosphere. The minimum path length is when the sun is directly overhead. The ratio of

any actual path length to this minimum path length is called “optical air mass” and is defined by:

$$Air\ mass = \frac{1}{\cos \theta} \quad \text{Equation 1}$$

Where θ is the zenith angle (angle between the overhead and sun). Using this definition, AM1.5 (i.e., sun at 48.19° zenith angle) is the most widely used standard test condition for measuring solar cell performance. At this condition, the total power density at the earth’s surface is 1 kW/m^2 [15].

It is worth to mention that the spectral composition of sunlight is far more complicated than what is presented here, therefore for an in-depth and comprehensive discussion reader should consult other resources [15-17].

1.3.2 Solar Cell Operation

A photovoltaic cell, also known as solar cell (hereon will used interchangeably), is the building block of the photovoltaic technology. In a very simplified description, a conventional inorganic solar cell is a two-terminal p-n junction device, composed of photoactive p-type and n-type semiconducting materials (see Figure 1-2-a). The fundamental operation mechanisms and governing equations of this device is defined by crystalline semiconductor physics. The nearly perfect crystalline structure creates well-defined energy bands, and highly delocalized electronic excitations [15].

When light illuminates a solar cell, incident photons with an average energy larger than the semiconductor band gap energy can create an electron-hole pair by exciting

electrons from top of the valence band to the bottom of the conduction band (photo-excitation). These free charges then move toward their favorable energy levels through a combination of drift (field driven in depletion region) and diffusion (gradient driven in n- and p- regions), and until finally reach to the terminals (electrodes) of the device (see Figure 1-2-b). The combination photo-generated voltage and current result in an output power for a PV cell.

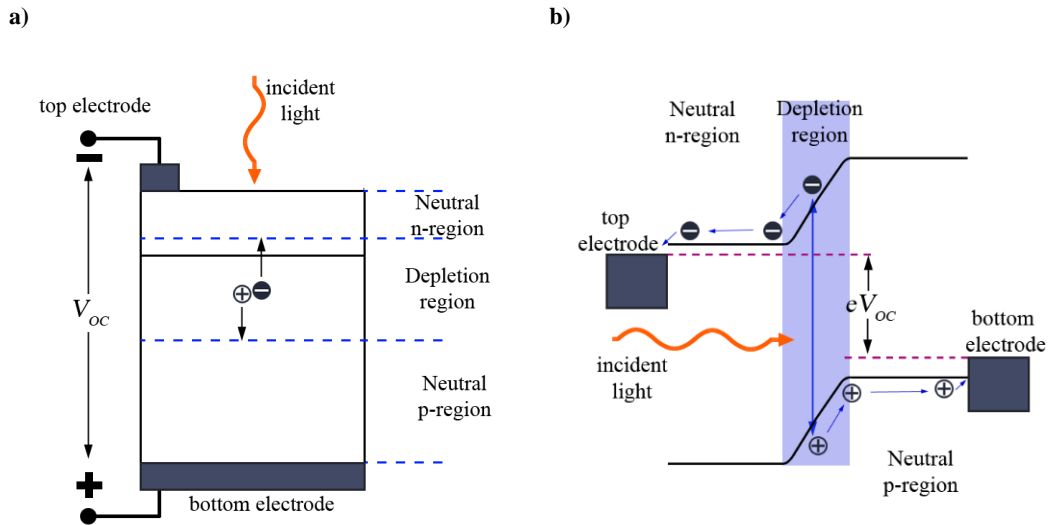


Figure 1-2: Simplified principle operation of an inorganic solar cell, a) photo-generation of electron-hole pairs inside the depletion region, b) energy level diagram (non-equilibrium) showing the generation of electron-hole pairs inside the space-charge region. Charge carriers then swept away toward their favorable energy levels and accumulate at the electrodes. Small arrows represent the direction of free charges movement.

1.3.3 Equivalent Circuit

The current-voltage characteristics of a solar cell can be described using an equivalent circuit depicted in Figure 3 where the DC current source represents the

photocurrent density (J_{ph}), the diode represents an ideal solar cell in the dark (J_0 is the reverse saturation current, n is ideality factor), the shunt resistance (R_P) represents leakage, and R_S is the series resistance. R_P and R_S are referred to as the parasitic resistances.

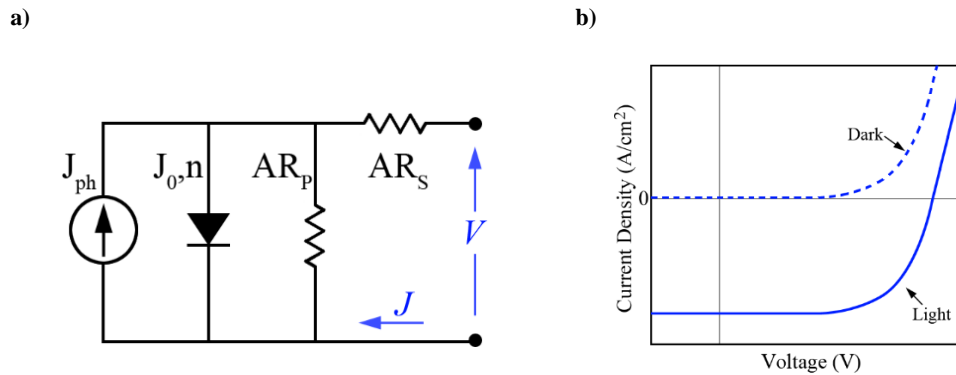


Figure 1-3: a) Equivalent circuit of a solar cells with total active area equal to A , b) the J - V characteristic of a solar cell at dark and under illumination [18].

The operation of a solar cell, namely its J - V characteristic in the dark and under illumination as depicted in Figure 1-3 with its equivalent circuit is analytically described by the following characteristic equation which is based on a Shockley diode [18]:

$$J = \frac{1}{1 + R_S/R_P} \left\{ J_0 \left[\exp \left(\frac{V - JR_S A}{nkT/q} \right) - 1 \right] - \left(J_{ph} - \frac{V}{R_P A} \right) \right\} , A/cm^2 \quad \text{Equation 2}$$

Where A is the effective area of the cell, k is the Boltzmann constant, T is the device temperature, q is the elementary charge, and n is the ideality factor.

1.3.4 Performance Metrics

The typical parameters used to characterize a solar cell are extracted from the J - V characteristic curve under illumination. These parameters are the open-circuit voltage (V_{OC}), short-circuit current (J_{SC}), and the maximum power density (P_{max}) [19], as shown in Figure 1-4.

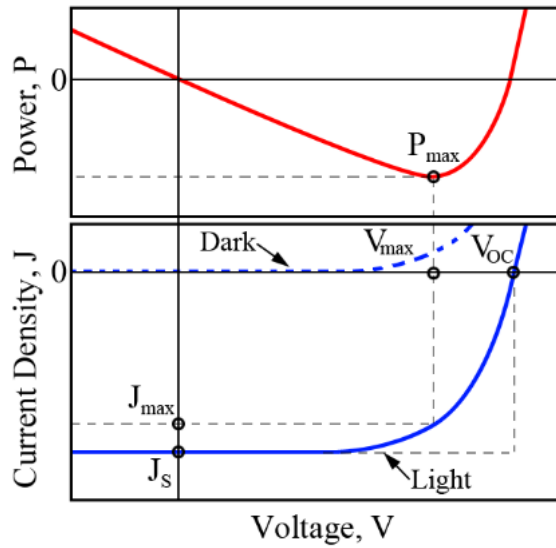


Figure 1-4: Power and current density as a function of voltage for a solar cell under illumination.

The V_{OC} is the maximum extractable voltage from the solar cell under illumination with zero-current flow. V_{OC} is defined by the level of illumination and the properties of the photoactive semiconductors and is also defined by the difference between quasi Fermi level energies of electrons and holes in the n-type and p-type semiconductor regions, respectively.

The J_{SC} is the maximum current density drawn from a solar cell under illumination. J_{SC} is a direct representation of photo-generated current in a solar cell.

Analytically, the V_{OC} and J_{SC} can also be calculated using the following expressions:

$$V_{OC} = \frac{nkT}{q} \ln \left[1 + \frac{J_{ph}}{J_0} \left(1 - \frac{V_{OC}}{J_{ph}R_pA} \right) \right] , V \quad \text{Equation 3}$$

$$J_{SC} = -\frac{1}{1 + \frac{R_S}{R_p}} \left\{ J_{ph} - J_0 \left[\exp \left(\frac{|J_{SC}|R_S A}{\frac{nkT}{q}} \right) - 1 \right] \right\} , A/cm^2 \quad \text{Equation 4}$$

Another important performance metric is the fill factor (FF), a normalized parameter that is calculated using the following expression:

$$FF = \frac{V_{max} I_{max}}{V_{OC} I_{SC}} \quad \text{Equation 5}$$

Where I_{max} and V_{max} are the current and voltage at which the maximum power is generated (also shown in Figure 1-4).

The power conversion efficiency (PCE), the most important performance indicator of a solar cell, is calculated using the following expressions:

$$PCE = \frac{V_{max} I_{max}}{P_{IN}} = \frac{V_{OC} I_{SC}}{P_{IN}} FF = \frac{V_{OC} J_{SC}}{I} FF \quad \text{Equation 6}$$

Where P_{IN} is the incident power ($Watt$), and I is the irradiance of the incident light ($Watt/cm^2$).

1.3.5 Existing Technologies

A variety of different semiconductor materials and device architectures have been used over the years to produce solar cells, as it is shown in Figure 1-5 [20].

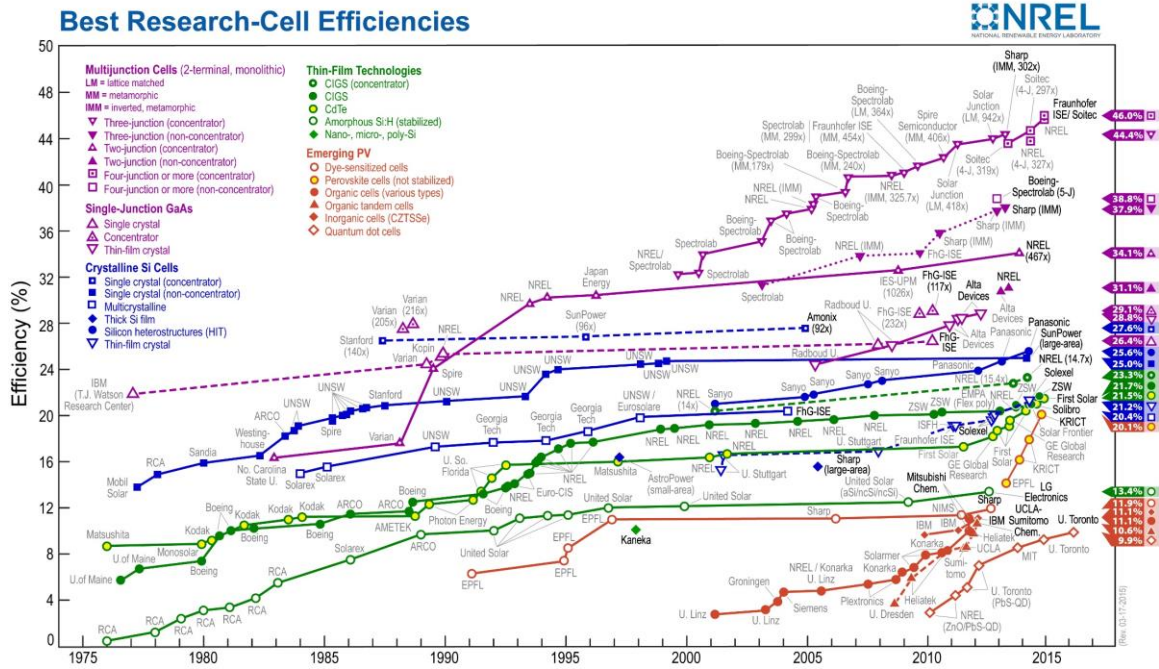


Figure 1-5: Existing PV technologies and their corresponding efficiency values (from NREL [20])

The classifications used in Figure 5, are mainly based on type of semiconducting material and solar cell configuration used. A list of most recent single solar cells and modules (an array of connected single cells) from different PV technologies with record high efficiencies are shown in Table 2 (adopted from reference [21]):

Table 2: Confirmed terrestrial single cell efficiencies measured under global AM1.5 spectrum (1000W/m²) at 25°C

Classification		Single cell		Module	
Technology	Material	Efficiency (%)	Note	Efficiency (%)	Note
Crystalline	Si	25.6	Panasonic HIT	22.4	SunPower
Thin-film	α -Si	10.2	ASIT	-	-
Thin-film	CIGS	20.5	Solibro	17.5	Solar Frontier
Thin-film	CdTe	21.4	First order	17.5	First Solar
Emerging	Dye	11.9	Sharp	N/A	-
Emerging	Organic	11.0	Toshiba	8.7	Toshiba
Emerging	Perovskite	11.1	Mitsubishi Chemical	-	-

As it is shown in this table, efficiencies largely vary between different PV technologies. It is also evident from this data that between a single solar cell and a solar module, there is a considerable drop in efficiency. This issue will be discussed in more detail in the following chapter. But at a first glance, crystalline silicon with highest power conversion efficiency, both for single cell and module, may seem the best solution today for the PV industry.

There is no doubt that efficiency is an important metric, but from economical perspective, there are also other components that contribute to the overall cost of a technology [22].

Levelized cost of energy (LCOE) is an economic metric representing the cost in dollars per kilowatt-hour (\$/kWh) to build and operate an energy generating system (mainly electricity power plants) over an assumed financial lifetime and duty cycle. Key inputs to calculating LCOE include capital costs, fuel costs, fixed and variable operations and maintenance costs, and financing costs [23, 24].

LCOE is widely used to make comparison between different energy generating technologies. Figure 1-6 shows an example of such calculations reported by the U.S. Energy Information Administration (EIA) in their 2014 annual report [3]. For PV technology to be economically feasible, it must reach to a LCOE that is comparable or lower than LCOE of fossil-based energies [25].

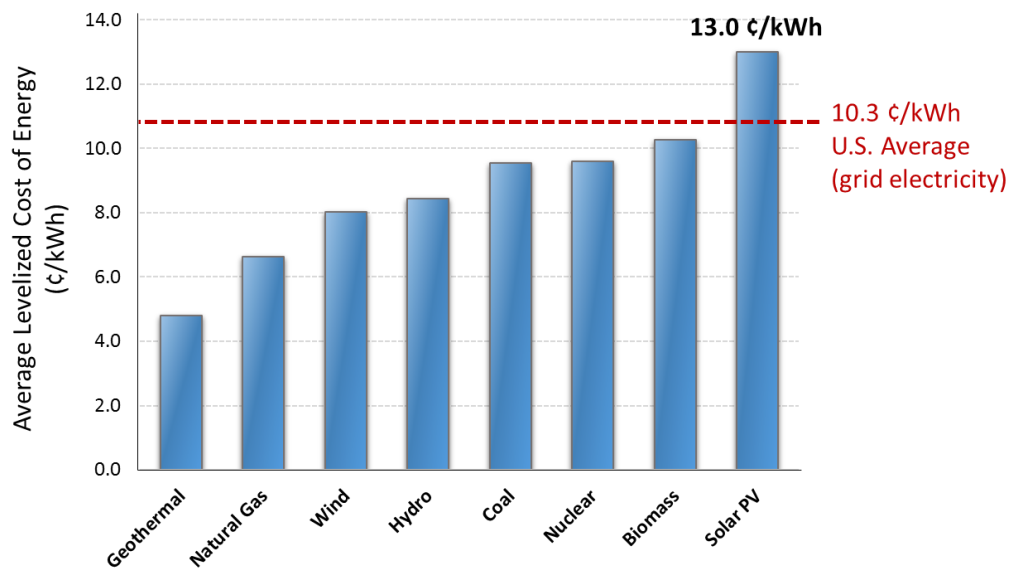


Figure 1-6: LCOE of different renewable technologies

However, from environmental sustainability standpoint, LCOE does not consider or associate any cost for activities that harm the environment, such as greenhouse gas (GHG) emissions. Inclusion of such environmental aspects in the LCOE calculations can drastically change the competitive scene for all renewable energies in their economic battle with traditional fossil-based sources of energy.

The energy payback time (EPBT) of an energy generating system is another relevant metric for cross comparison between different technologies. EPBT is the total time (typically expressed in years) that an energy generating system requires to generate as much energy as was consumed for production of that system [26, 27].

These all said, the lack of clarity in reporting assumptions, justifications and degree of completeness in LCOE and EPBT calculations, have created contradictory results and a lot of debates over the validity and comprehensiveness of such assessments [7, 23].

This dissertation is not going to treat these economic assessment topics in details. Nonetheless, besides the importance of addressing key cost items in aforementioned LCOE, it is critical for PV technology to find ways to increase the efficiency, and reduce the cost of material and manufacturing, for it to become competitive alternative to fossil-based resources [22, 23, 28].

In the following sections we briefly introduce and survey three PV technologies: crystalline silicon, thin-film, and emerging PV. This section is mainly focused on the advantages and associated challenges of each technology.

1.3.5.1 Crystalline Silicon PV

Crystalline silicon-based solar cell is the first generation and the most mature and widely used PV technology. Mono-crystalline and poly-crystalline are the main two classes of crystalline silicon used to produce these PVs.

Mono-crystalline silicon PV accounts for 80% of today's total PV market, displaying single-cell PCE values of 25% [29]. These solar cells are crystalline silicon p-n junction

that are manufactured from a single crystal ingot using the Czochralski method [14, 15]. Although this technology offers high PCE values, it also has a high associated manufacturing costs, because achieving high yields and reliable solar cells requires highly specialized facilities and virtually defect-free fabrication processes that are very energy intensive, which requires considerable capital investments.

Polycrystalline solar cell technology offers lower PCE values, typically below 20% [30] but allows for reductions in the cost of manufacturing compared to mono-crystalline silicon solar cells [14, 15, 31]. Although silicon-based PV solar cells remain the dominant player in the PV market due to its high efficiency, their fabrication processes are very complex and energy-intensive which over the years has made the cost-of-energy produced by this technology typically uncompetitive with conventional sources such as fossil fuels.

Although in recent years, governmental subsidies and incentives have made the cost-of-electricity of silicon solar cells competitive with conventional sources of energy in certain markets, fabrication complexities and associated costs of silicon PV lead also to long EPBT of a few years, and undesirably high GHG emissions [25, 32-34], making them a less appealing long-term solution from a sustainability perspective. These disadvantages of silicon PV are the main reason for the research community and industry to explore alternative materials for solar energy generation [35].

1.3.5.2 Alternative PV Solutions

Thin-film solar cells are the second generation of photovoltaic technology. These devices are composed of thin layers of semiconductor materials stacked on top of each

other. The main objective of the thin-film technology is to reduce the cost of PV system by lowering the cost of materials used and manufacturing. Thinner films, less expensive deposition techniques (such as sputtering, ink printing and electroplating), and possibility scaling into large inexpensive substrates are the major advantages of this technology over conventional crystalline silicon [36]. Leading thin-film solar cell technologies with commercial importance are: amorphous silicon (α -Si), poly-crystalline silicon (poly-si), cadmium telluride (CdTe), and variations of copper indium (such as copper indium gallium selenide: CIGS).

Thin-film photovoltaics have been less efficient than crystalline silicon counterparts [14]; however they have the potential of leading to significantly lower cost production costs and lower EPBT and GHG emissions. Today, the main focus of the research in this field is on processing optimization to improve the performance and yield. Third-generation solar cells are made from different class of semiconducting materials. Dye-sensitized solar cells (DSSC), and organic solar cells (OSC) are examples of this class of photovoltaic devices that use light absorbing organic semiconducting compound. Amongst all the alternative PV solutions, organic photovoltaics (OPV) is the most promising one because of its material diversity and low cost manufacturing [35, 37]. The focus of this dissertation is on this group of photovoltaic materials.

1.4 Organic Photovoltaics

Organic photovoltaics (OPV) is a class of PV devices based on conjugated organic molecules and polymers. The strongpoints and major advantages of OPV over other existing technologies are in two areas: materials and manufacturing.

From material perspective, OPV uses a wide variety of synthesized materials that can be processed in air, at room temperature, and on recyclable substrates and materials [38, 39]. The importance of this aspect of OPV is that the physical and chemical properties of the organic semiconductors such as energy levels, optical absorption, solubility, etc. can be tailored by modifying the chemical structure of the molecules [39].

High degree of disorder in organic semiconductors along with weak electronic coupling (will be explained later) and electron-vibration coupling result in charge-carrier mobility values - how easy charge carriers can move in the bulk of material under applied electric field - with orders of magnitudes lower than inorganic semiconductors [13]. On the other hand, organic semiconductors have a relatively strong absorption coefficients usually in the range of 10^5 cm^{-1} . . This feature generally leads to OPV devices with very small thicknesses ($< 200 \text{ nm}$) [40].

From a manufacturing perspective, flexibility on tailoring the material properties enables utilization of high throughput, low-material-consuming fabrication methods such as all-additive printing [41, 42] and roll-to-roll printing [43, 44]. To illustrate the difference, some studies suggest that it would take one year for a silicon-based manufacturing to make the same total area OPV systems fabricated in only one day by an industrial screen printing [42]. In a similar manner, the EPBT could scale down from a few years for silicon PV to a few days for OPVs.

1.4.1 Evolution of OPV

The very first organic-based photovoltaic effect was reported in 1958 by Kearns and Calvin [45]. Their device was made of a magnesium phthalocynine (MgPh) disk coated

with a thin film of air-oxidized tetramethyl *p*-phenylenediamine (TM ϕ D) with maximum output voltage of 200 mV and power output of 3×10^{-12} W [45]. However, active interest in the research community did not really start until 1986, when Tang, et al. reported a single hetero-junction organic photovoltaic cell with a power conversion efficiency of about 1% [46].

Such a major improvement was a result of the development of highly-pure synthesized small organic molecules as well as advancements in physical vapor deposition (PVD) techniques at room temperature during early 1980's [13]. Since then, and mainly in last ten years, the field of organic photovoltaic has progressed significantly as a potential candidate for affordable renewable energy production [47]. The following table is a summary of prior-art reports on OPV single cells with the highest PCE values:

Table 3: The highest PCE values for OPV technology reported in literature until 2013

	Device type	J_{sc} (mA/cm ²)	V_{oc} (V)	FF (%)	PCE (%)	Active area (cm ²)	Reference
Polymer	Single junction	17.5	0.75	70	9.2	0.16	[48]
	Tandem	10.1	1.53	68.5	10.6	0.1	[49]
Small molecule	Single junction	15.5	0.8	72.4	8.94	0.05	[50]
	Tandem	6.2	1.97	54	6.6	NA	[51]
Polymer processed in air on flexible substrate	Single junction	8.9	0.68	57	3.5	1	[33]
	Tandem	5.11	1.02	35.8	1.3	1	[52]

1.4.2 Organic Semiconductors

To understand the operation mechanism of organic solar cells, it is necessary to understand the fundamental physics and chemistry of organic materials. Organic semiconductors are a group of carbon-based materials with optoelectronic properties that originate from carbon atomic orbitals and specific bonding with other atoms, and can be synthesized and modified using chemistry techniques.

Organic semiconductors are classified as polymers or small molecules. Small molecules are chemical compounds with specific molecular weight, while polymers exist in a form of long chains of repeating molecular sub-units, without a specific (well-defined) molecular weight. To make organic thin-films, polymers are typically solution processed (i.e. spin-coating), while small molecule compounds can either be solution processed or thermally evaporated.

In contrast to crystalline silicon where the nearly perfect crystalline structure creates a well-defined energy band formation and highly delocalized electronic excitations [15], solid-state organic thin-films contain disorder, with weak interactions between adjacent molecules, and highly localized electronic excitations. Therefore packing of the molecules and morphology of the films have vital effect on the electronic properties [39, 53]. This makes the optimization of fabrication processing a critical step to make efficient organic devices.

1.4.2.1 Atomic Orbitals

The optoelectronic properties of organic semiconductors are determined by the electronic configurations of the atoms and molecules that form the film and by the electronic coupling between them. Such a description on a molecular scale is the realm of

quantum mechanics. The Schrödinger equation is a partial differential equation that describes how the wave-function of a physical system evolves over time. Solutions of the Schrödinger equation for an electron in an atom, provide electron wave-functions and allowable energy states. These allowable energy states for an electron around a nucleus are also called “atomic orbitals.” These atomic orbitals have a specific spatial distribution, energy level, and orientation. Figure 1-7 shows *s* and *p* orbital. As it is shown, the *s* orbital has a symmetric spherical shape, whereas the *p* orbitals have a dumbbell shape.

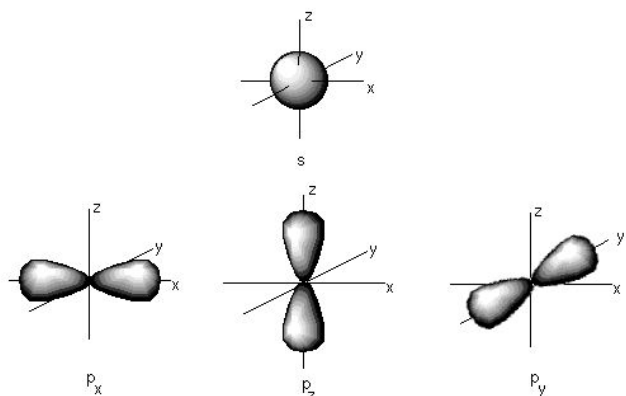


Figure 1-7: Representation of *s* and *p* atomic orbitals.

1.4.2.2 Bonding

In a neutral carbon atom, there are six electrons represented as $1s^2 2s^2 2p^2$. The preceding numeric labels, 1 and 2, are called “principal quantum number” (conventionally shown by *n*). This number corresponds to the level of energy of that orbital. The higher the quantum number of an orbital, the higher the energy of that orbital. An orbital with the highest principal quantum number in an atom is the furthest orbital from the nucleus (also called outer shell).

Out of six electrons of carbon atom, two are in the $1s$ orbital, and the other four in the $2s$ and $2p$ orbitals. These four electrons in the outermost orbital ($n = 2$), $2s^2 2p^2$, are called valence electrons and are involved in forming covalent bonds with other atoms. Covalent bond is a chemical bonding in which atoms share a pair of valence electrons (one electron from each atom).

Considering the spatial shape and orientation, the four valence orbitals of carbon atom are: $2s$, $2p_x$, $2p_y$, and $2p_z$.

In the case of methane (CH_4), valence electrons of carbon couple with valence electrons ($1s^1$) of four hydrogen atoms and form four covalent bonds, in which one electron from carbon and one electron from hydrogen are shared. According to “hybridized orbital theory” when carbon atoms have identical single bonds with other atoms (as is the case in CH_4), a carbon $2s$ orbital hybridizes with three $2p$ orbitals to form four equal (in terms of shape and energy) sp^3 hybridized orbitals [39].

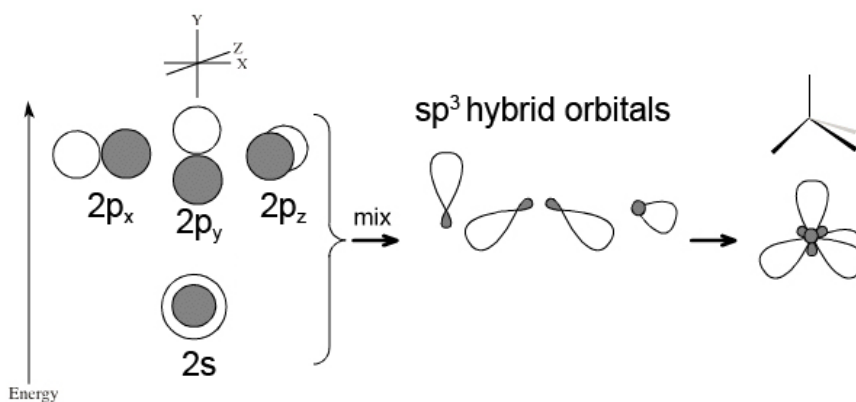


Figure 1-8: Representation of $2s$ and $2p$ orbital hybridization in methane.

A carbon atom can undergo another kind of hybridization when it binds to another carbon atom such as in ethylene.

In a case of ethylene, where carbon atoms bonds to three others atoms, the $2s$ orbital and two of the $2p$ orbitals (p_x and p_y) are involved in the creation of three new orbitals called sp^2 hybridized orbitals. After sp^2 hybridization, a single remaining un-hybridized p orbital (p_z) stays perpendicular to the plane containing the sp^2 orbitals (shown in Figure 1-9). These two un-hybridized p_z orbitals can overlap, and form a so-called π -bond. Therefore the two carbon atoms will have a covalent double bond (four electrons are shared between two atoms) composed of one π -bond and one σ -bond.

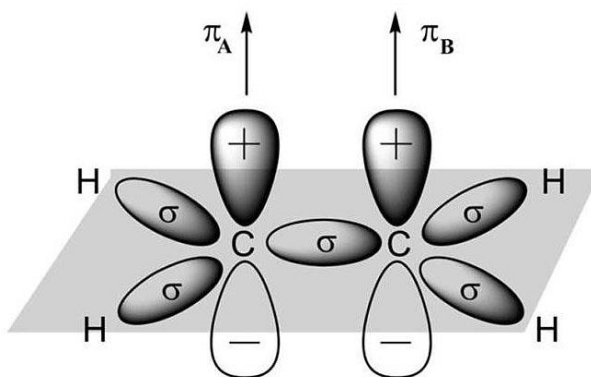


Figure 1-9: Schematic of σ -bond and π -bond in ethylene (C₂H₄).

The strength of a σ -bond is much greater than that of a π -bond; consequently, the electrons forming the π -bond (known as π -electrons) are less tightly bound to nucleus and more delocalized in space.

1.4.2.3 Conjugated Molecular Systems

Molecules with a series of multiple alternating single and double bonds are called conjugated. For example in polyacetylene (PA) each carbon on PA backbone uses three hybridized sp^2 orbitals and form three σ -bond with one hydrogen and two other carbons. All p_z orbitals on the other hand stay normal to the σ -bond plane and overlap. This overlap leads to long range delocalization of these π -electrons across the PA chain.

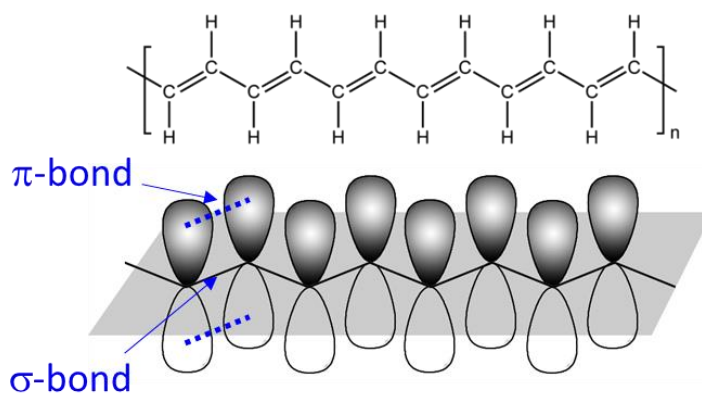


Figure 1-10: Schematic of σ -bond and π -bond in conjugated polymer polyacetylene (PA).

These loosely bound π -electrons in organic systems, are the origin of the electrical and optical properties in organic semiconductors.

1.4.2.4 Molecular Orbitals

As we discussed the covalent bonding, when two atoms get close, their atomic orbitals overlap to form a covalent bond. However, the two shared electrons cannot have the same energy levels (Pauli exclusion principle) therefore the two overlapped atomic

orbitals split into two new different orbitals (in terms of energy and shape) called “molecular orbitals” (MOs). These MOs are linear combination of atomic orbitals. Linear combination of the wave function of two atomic orbital, generates pair of molecular orbitals, one with an energy level below the original atomic orbital level, called bonding molecular orbital, and one with a higher energy level, called anti-bonding molecular orbital. For example the overlap of the two p_z orbitals of two carbon atoms in ethylene (Figure 1-9) results in one bonding (π) and one anti-bonding (π^*) orbital. When there is no perturbation the two electrons (opposite spins) reside in the bonding (π) orbital which has a lower total energy (stable). Therefore since the bonding (π) orbital is the filled with the valence electrons (electrons in the outer shell with the highest energy), in this two-atom system, this is called the highest occupied molecular orbital (HOMO). The same concept holds for the anti-bonding (π^*) and it is called the lowest unoccupied molecular orbital (LUMO). The HOMO and LUMO are known as the “frontier orbitals”.

All discussed up to this point was based on one-electron wave-function. In a real case, what is measured upon excitation (ionization) is the energy difference between the N -electron ground state of the molecule and the N -electron excited state (the $N\pm 1$ -electron ionized state) [54].

For the purpose of calculations, it is however assumed that the HOMO level is minus the energy of the ionization energy (IE) and the LUMO is minus the energy of the electron affinity (EA) [54]. Ionization energy (IE) defined as the minimum amount of energy required to remove an electron, and electron affinity (EA) defined as the amount of energy released by adding an electron to a molecular system. The difference between these two is often called the transport gap or fundamental gap:

$$E_{fund} = IP - EA \quad \text{Equation 7}$$

The frontier orbital levels can be estimated by using a number of spectroscopic techniques, such as x-ray photoemission spectroscopy (XPS), ultraviolet photoemission (UPS), and inverse photoemission spectroscopy (IPES) on thin-films. Also electrochemical analysis such as cyclic voltammetry (CV) in combination with UV-Vis optical absorption is common to measure the frontier molecular orbitals in ionic solution.

In molecular systems, optical gap (E_{Opt}) of a molecule (lowest electronic transition due to absorption of single photon) is substantially lower than the fundamental gap. The reason is that the excited electron and the corresponding hole are electrostatically bound. This binding energy, (E_B) can be calculated using the following formula:

$$E_B = E_{fund} - E_{Opt} \quad \text{Equation 8}$$

1.4.2.5 Excitons

The excited electron and its associated hole are initially bound to each other through coulombic forces. This bound state of an electron and hole pair is called “exciton” [39, 53]. In π -conjugated molecules, the exciton binding energy is typically on the order of a 0.1 - 0.5 eV. This high exciton bonding energy is mainly related to the low dielectric constant ($\epsilon_r < 5$) of these materials, the electron-electron and electron-vibration interactions. In contrary, in conventional crystalline inorganic semiconductors with a well-defined crystalline structure, the exciton binding energy is in the order of 0.01 eV which is much lower than thermal energy at room temperature (0.025 eV). Therefore

optical excitation even at room temperature can result in free carrier formation [40, 47].

The schematic of excitons in crystalline vs. disorders system is illustrated in Figure 1-11.

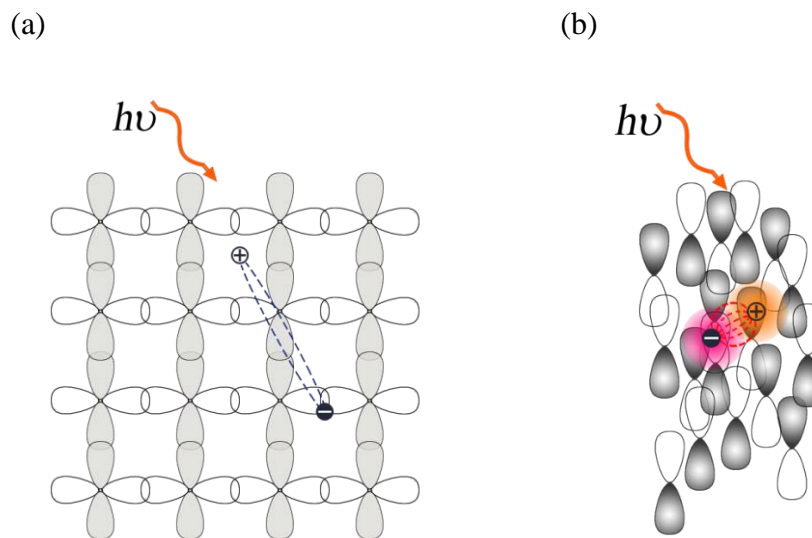


Figure 1-11: Schematic representation of exciton formation in (a) perfectly ordered crystalline inorganic material, and (b) in disordered organic material.

Excitons are an intermediate species in organic photovoltaic energy conversion process, but their high binding energy impedes the formation of free-charge carriers. Therefore a driving force is required to break them into free charge carriers [40].

A “donor” material has low HOMO energy (low ionization energy: IE) and is suitable for hole injection/collection from high work function electrodes, whereas an “acceptor” material has a high LUMO energy (high electron affinity: EA) and suitable for electron injection/collection from low work function electrodes [13, 39, 53].

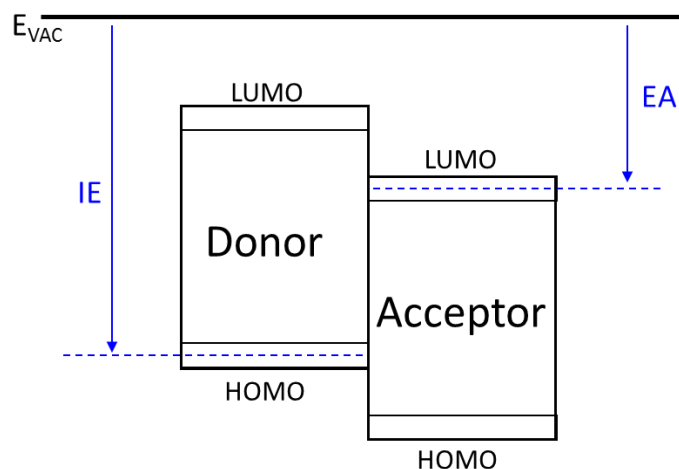
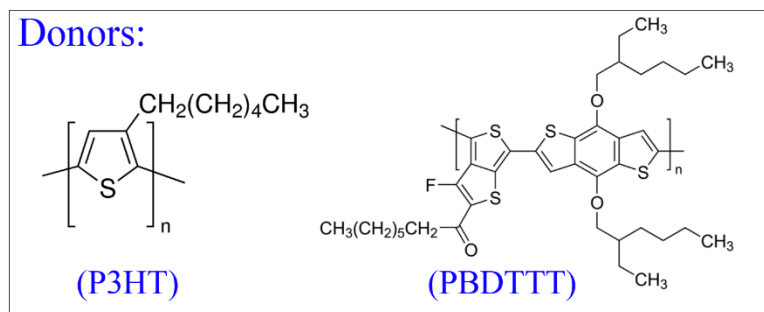


Figure 1-12: Simplified energy diagram of a donor/acceptor interface.

When a donor and an acceptor are brought together and form an interface, the offsets between their energy levels creates a driving force that can facilitate the dissociation of excitons [47]. As of today, there is no clear explanation to describe exciton dissociation at donor acceptor interfaces as several factors can come into play and complicate this dissociation process [13].

A number of widely used donor and acceptor organic photoactive semiconductors are shown in Figure 1-13.

(a)



(b)

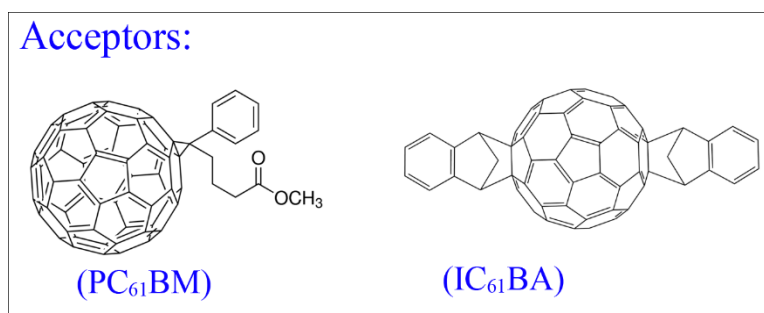


Figure 1-13: Chemical structures of commonly used (a) donor and (b) acceptors organic semiconductors in PV.

1.4.2.6 Charge Transport

In materials that are highly-ordered, like inorganic crystalline materials, the electronic wave-functions are delocalized over the whole system, resulting in a band regime behavior in which the charge carriers can freely move over the entire structure [55].

In organic (polymeric) materials, weaker intermolecular interactions cause the energy levels to broaden into electronic bands with widths determined by the strength of the intermolecular interactions. In disordered configurations like in organic thin-films,

due to a very weak coupling, the wave functions are localized over a few surrounding molecules. In such highly disordered systems, transport generally proceeds through hopping and is thermally activated [56].

1.4.3 OPV Cells

OPVs are typically built on transparent substrates (such as glass) having a layer of a transparent conducting metal oxide (such as indium tin oxide) as bottom electrode, a stack of organic layers including the photoactive organic semiconductor, and a back metal contact. The photoactive layer is typically composed of a combination of an electron-donor (donor) with an electron-acceptor (acceptor). These donor and acceptor materials can either be stacked as separate layers (bi-layer hetero-junction), or mixed together as one single layer, called bulk hetero-junction as shown in Figure 1-14. The focus of this dissertation is on bulk hetero-junction OPV cells.

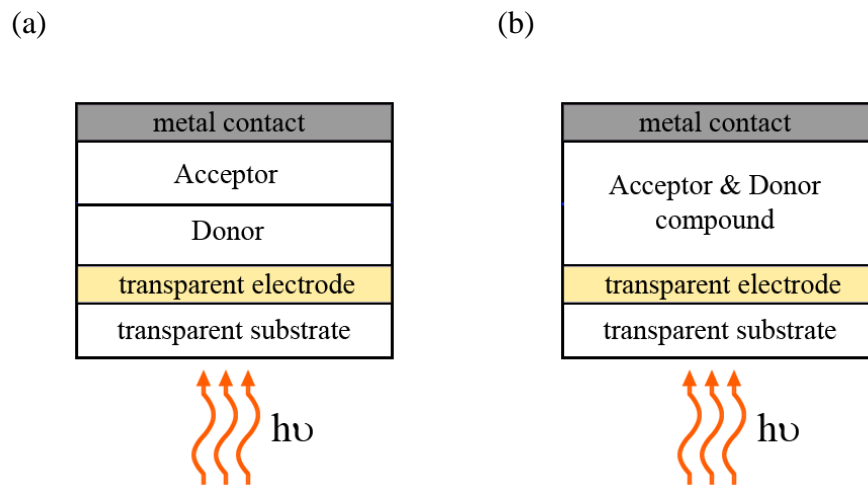


Figure 1-14: Schematic of typical OPV cell structures: (a) bilayer cell in which the acceptor and donor materials are deposited separately, and (b) bulk hetero-junction cell in which the acceptor and donor materials are mixed and deposit together.

The photoactive layer is generally sandwiched between a hole-collecting electrode (HCE) with high work function and an electron-collecting electrode (ECE) with low work function.

The energy levels of these organic layers along with the position of their corresponding electrodes in a simplified energy diagram are shown in Figure 1-15.

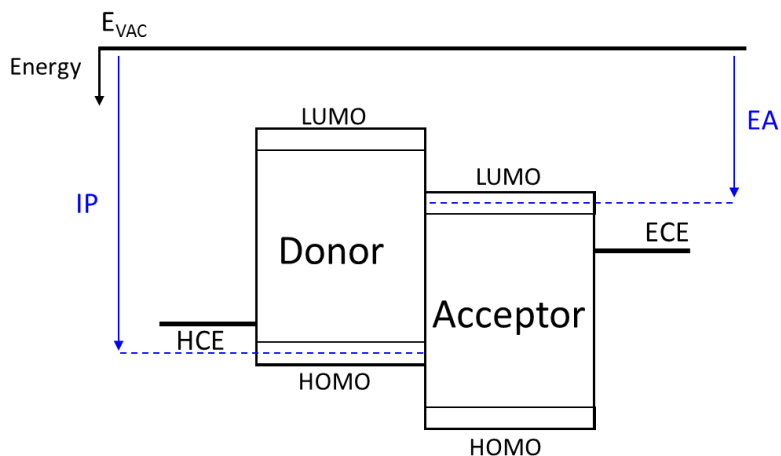


Figure 1-15: Energy diagram of a typical OPV cell composed of: hole collecting electrode (HCE), donor organic semiconductor, acceptor organic semiconductor, and electron collecting electrode (ECE). The vacuum is the reference to measure the ionization potential (IP) of the donor material and the electron affinity (EA) of acceptor material.

1.4.4 OPV Operation

At this point, it is worth mentioning that a detailed picture of the operation of an OPV cell is still an active area of research and a subject of debate in the community. However; in this section, a high-level picture of commonly accepted principles of operation will be briefly discussed.

When light illuminates an OPV device, photons with an energy larger than the optical band-gap of the photoactive organic layer are absorbed forming an exciton [57]. As discussed before, an exciton in an organic semiconductor has a binding energy on the order of 0.1 to 0.5 eV. This high exciton binding energy does not allow easy dissociation at room temperature ($kT = 0.025$ eV at $T = 300$ K). We have to remember that excitons are neutral species that diffuse through random hops [13, 57]. Excitons that reach a donor/acceptor interface, will have a chance to dissociate through an electron transfer reaction between a donor and an acceptor molecule.. The difference in energy between the frontier orbitals at the interface provides a driving force for a transfer of the electron on the acceptor molecule and hole on the donor molecule [57], as depicted in Figure 1-16. It is also worth to mention that excitons have a short lifetime, and short diffusion lengths before they decay, therefore, the nanoscopic morphology of the photoactive material is critical for the operation of an OPV cell [58, 59].

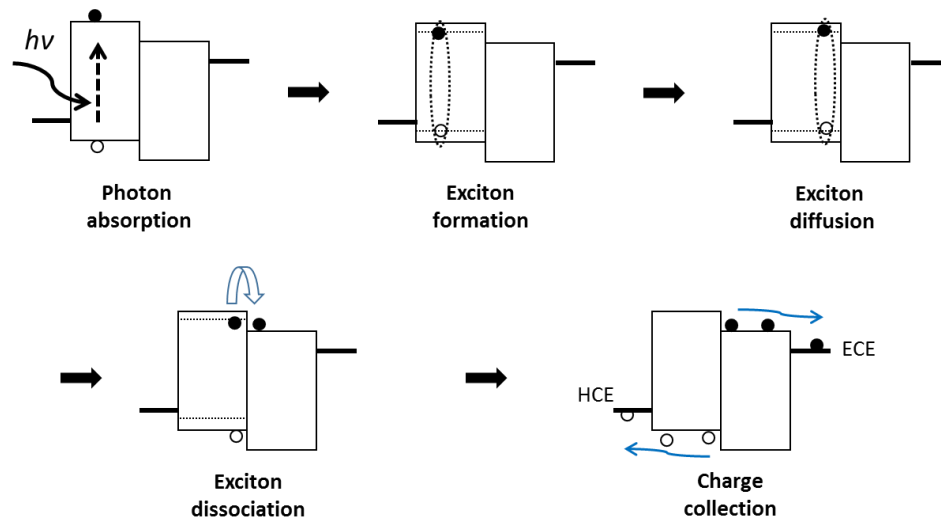


Figure 1-16: OPV Operation: Starting from top left: Photo absorption leads to an exciton formation (shown only in donor side), then exciton migrates toward the donor/acceptor interface. At the interface electron and hole dissociates and then each migrates toward the corresponding electrodes.

When electron and holes are separated, these charge carriers have a chance to move toward their corresponding electrodes. The migration of free charge carriers toward collecting electrodes is influenced by many factors such as degree of energetic disorder and vibrational coupling. Therefore the transport of these charge carriers is governed by a hopping mechanism [56].

Finally, those charge carriers that have reached to the electrodes/semiconductor interface before recombining will have a chance of getting collected and contribute to the overall current. All the aforementioned steps are summarized in Figure 1-16.

To enable efficient charge collection at the electrodes, one must select electrode materials and interfaces that yield a work-function that matches the EA of the acceptor, and a WF that matches the IE of the donor material as shown in Figure 1-15.

1.4.5 OPV Device Structures: Conventional vs. Inverted

OPV cells are fabricated based on two device geometries having different polarity: conventional and inverted. These configurations are shown in Figure 1-17. In OPV cells with conventional geometry, the HCE is at the bottom and the ECE is on top of the device. The ECEs are typically low work function metals such as LiF/Al, Ca/Al, etc. thus are very reactive and gets oxidized in the presence of ambient oxygen and water. Until recently, this limited the air stability and overall lifetime of OPV cells with conventional geometry. To address the air-stability issue due to low WF reactive-metal top contacts, “inverted” OPV cell is used as an alternative structure (Figure 1-17-b). In this geometry the ECE is placed at the bottom of the OPV cell and HCE goes on top. The low WF ECE

is typically an indium tin oxide (ITO) layer that is covered with low WF electron-collecting interlayer.

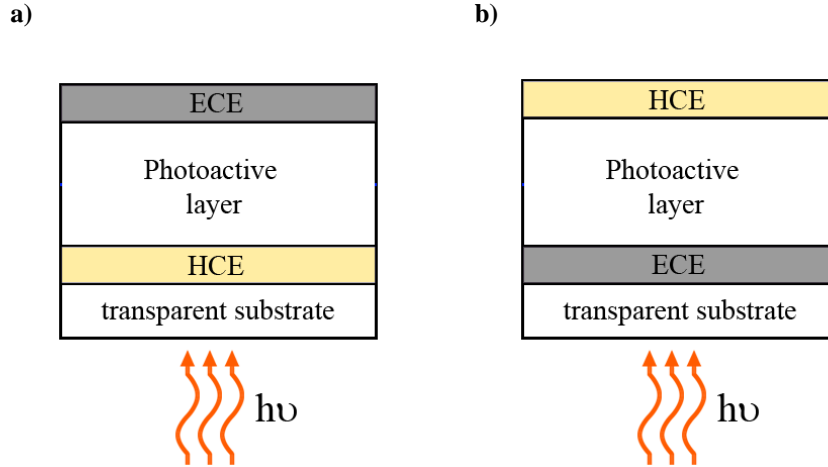


Figure 1-17: Two typical geometries of an OPV cells: a) conventional, b) inverted

Recently, we have shown that surface modifiers based on aliphatic amine polymers can be used as interlayers to very significantly reduce the WF traditional high WF electrodes. In fact, we have shown that this group of materials can substantially reduce the WF of variety of different conductors such as metals, conductive metal oxides, conducting polymers, etc. This WF reduction originates from physisorption of the neutral polymer and the creation of an interfacial surface dipole, which turns the modified conductors into efficient ECEs. These polymer surface modifiers are processed in air from solution, providing an appealing alternative to reactive low-WF metals. Polyethylenimine ethoxylated (PEIE) is an example of such polymers (Figure 1-18-a). A thin layer of PEIE reduces the WF of ITO from 4.4 eV down to 3.3 eV (UPS measurements) [60]. PEIE is an insulator, but the amine groups in its structure allows for electrons to be partially displaced or transferred towards the surface of a conductor, thus

creating a dipole moment on the modified surface which in turn results in a strong shift in vacuum level. This shift in vacuum level corresponds to a decrease of the WF (Figure 1-18-b).

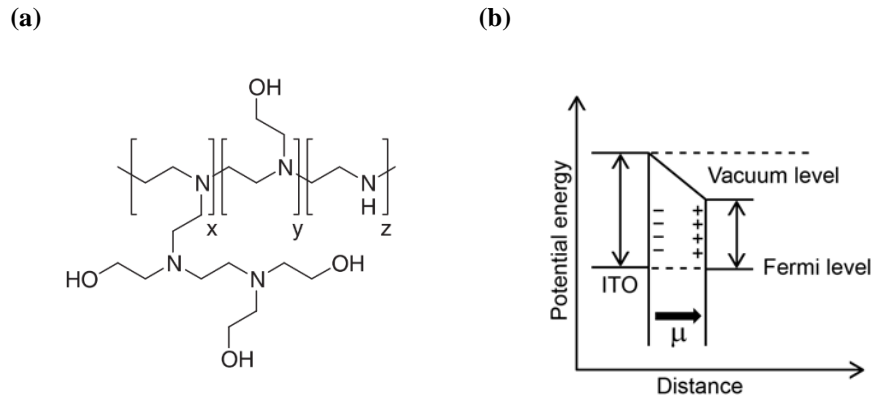


Figure 1-18: Polyethylenimine ethoxylated (PEIE): (a) the chemical structure, (b) the shift in vacuum due to the dipole moment created by PEIE molecule

Shown in Table 4 is a list of different metals and conductive metal oxides that are treated with PEIE and PEI. Of particular important, is the fact that PEIE or PEI significantly modify the WF of organic semiconductors such as Poly(3,4-ethylenedioxythiophene) Polystyrene sulfonate (PEDOT:PSS) and graphene, opening the door for all plastic polymeric single and tandem OPVs and significantly improving the outlook for improving the environmental stability of OPV devices in both, inverted and conventional geometries.

Table 4: Work function of conducting materials with and without polymer modifiers, as independently measured by Kelvin probe in air and by UPS. Empty cells indicate no measurement for the corresponding sample [60].

Electrodes	Work function (eV)					
	Kelvin probe in air			UPS		
	Pristine	With PEIE	With PEI	Pristine	With PEIE	With PEI
Metal oxides						
ITO	4.62 ± 0.06	3.60 ± 0.06	3.50 ± 0.06	4.40	3.30	3.27
	$5.16 \pm 0.06^*$	$3.60 \pm 0.06^*$	—	5.00*	3.30*	—
ZnO	4.26 ± 0.06	3.28 ± 0.06	3.10 ± 0.06	3.96	3.55	3.17
FTO	4.68 ± 0.06	3.80 ± 0.06	3.60 ± 0.06	—	—	—
Metals						
Au	5.10 ± 0.10	3.90 ± 0.06	3.94 ± 0.06	4.70	3.40	—
Ag	4.60 ± 0.06	3.70 ± 0.06	3.60 ± 0.06	—	—	—
Al	3.40 ± 0.06	2.75 ± 0.06	—	—	—	—
PEDOT:PSS	4.90 ± 0.06	3.58 ± 0.06	3.88 ± 0.06	4.95	3.32	3.16
Graphene	4.60 ± 0.06	3.80 ± 0.10	—	—	—	—

*Substrate was treated with an O₂ plasma for 2 min prior to measurements or polymer modifier deposition.

CHAPTER 2: LARGE AREA PV SYSTEMS: SOLAR CELL MODULES

A single solar cell produces limited electrical power and low voltage which are both too small for practical purposes. Thus, to generate useful amounts of electrical power, single solar cells need to be connected, typically in series, to make what is called a “solar cell module.” These modular units can then be connected together to form “solar cell panels” (arrays) to produce the desired power output (Figure 2-1).

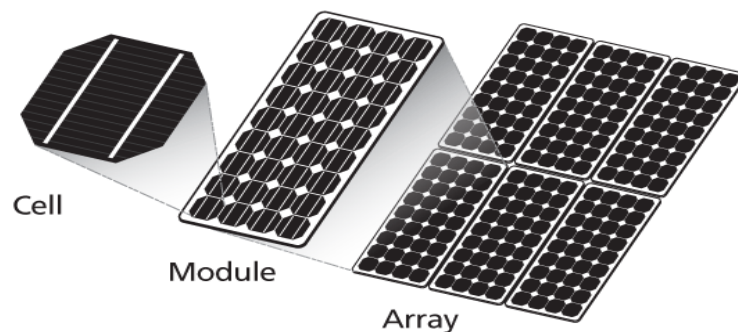


Figure 2-1: Transition from a single solar cell to a solar cell panel

The integration of single PV cells into a module varies between PV technologies and can be a costly operation. The typical processing steps for manufacturing of crystalline silicon PV technology are shown in Figure 2-2. In the case of crystalline silicon PV modules, module cost is primarily driven by the high-cost associated with the production and slicing of high-quality crystalline Si ingots [22].

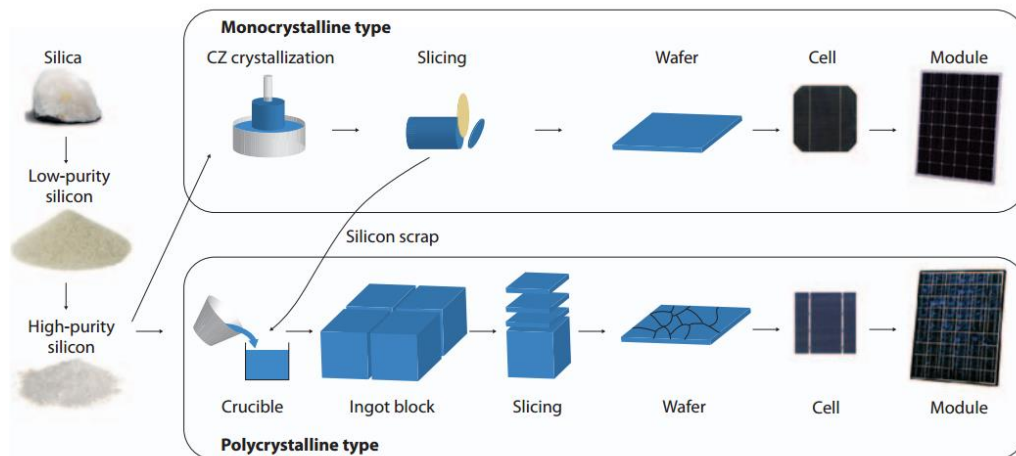


Figure 2-2: Production process for typical commercial crystalline silicon solar cells.

Cost reduction of PV technology, in particular crystalline Si PVs, has been achieved by constantly increasing efficiency, lowering manufacturing costs, as well as by governmental regulations and incentives [22, 61].

To turn any new PV technology into a competing alternative to fossil-based resources, there are three main areas of interest:

- 1) Reducing costs of material
- 2) Reducing cost of manufacturing
- 3) Improving module efficiency

The major cost-reduction strategies in module manufacturing industry are, but not limited to [61]:

- 1) implementation of streamlined and high throughput fabrication techniques
- 2) increasing process automation
- 3) fabricating large area solar cells

As it was discussed in section 1.3.5, the main objective of all the alternative PV technologies - including OPV - is to reduce its levelized cost-of-energy, energy payback times and green-house emissions. Despite currently displaying lower PCE values, thin-film PVs are perceived as the future of PV technology because they require less active materials and use unconventional and less energy-intensive manufacturing methods which could significantly improve the economic and environmental outlook of PVs compared to what can be realistically achieved with crystalline silicon PVs [62-65].

2.1 Early Photovoltaic Modules

Because single solar cells had low output voltage and currents, connecting them in parallel or series – called solar cell module - is the most effective way of using them. Vanguard1, the first solar powered satellite, was equipped with six small solar panels and launched in 1958 [66], and shortly after the Sharp Corporation produced one of the first practical silicon PV modules in 1963 and started the mass production of solar cells modules.

2.2 Conventional Thin-film PV Modules: The Stripe Geometry

Despite enormous progress in thin-film PV material optimization, large area PV-module technologies heavily suffer from electrical losses. These electrical losses can be classified into two main categories: shading losses and resistive losses [67, 68]. These power losses in a module are the direct consequence of conventional structure of the modules, the so-called “stripe geometry” (see Figure 2-3).

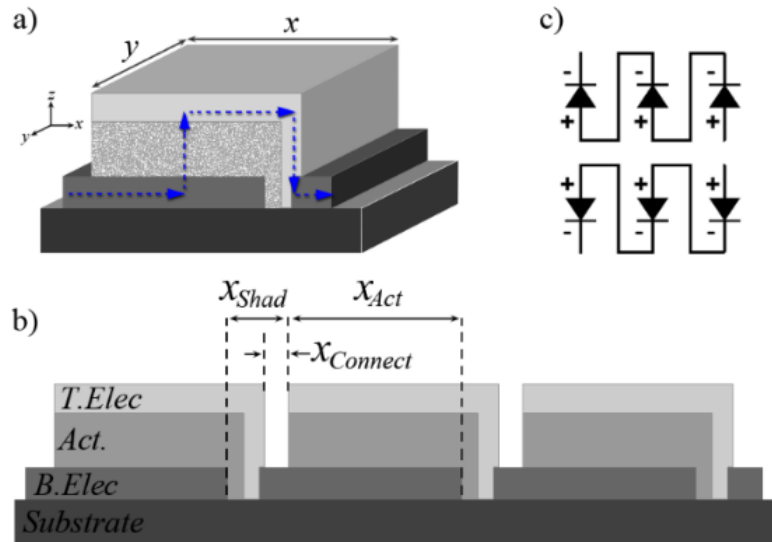


Figure 2-3: Schematic of a PV module with “stripe” geometry: a) Three dimensional representation of the unit cell, b) Shading length vs active length, c) Circuit diagram of the module.

The shading losses occur because areas of the individual cells in a module are shaded by interconnects or inter-cell gaps. This shaded regions of the cells cannot contribute to the photocurrent and therefore result in a loss of the total area J_{SC} [69].

Resistive losses are intrinsic to any solar cell or module structure, however the effects of parasitic shunt and series resistances should be minimized at the module level to preserve single-cell performance. In this regard, interconnects between adjacent cells increase the total series resistance of the module and in turn, lower the overall FF and PCE [67, 70].

2.2.1 Major Challenges

2.2.1.1 Losses in Stripe Geometry

The total power loss density in each cell (photo-generated power divided by total area) in a PV module with N cells connected in series (Figure 2-3) can be written as [67, 68, 70]:

$$P_{Total/Area} = \frac{P_{Total}}{A} = \frac{P_{Total}}{x \times y} = \text{Equation 9}$$

$$= \sum_N (P_{Shad,i} + P_{T.Elec,i} + P_{Act,i} + P_{B.Elec,i} + P_{Connect,i} + P_{Contact,i})$$

The subscribes denote power losses due to shading, top electrode, active layer, bottom electrode, interconnect, and contact between interfaces, respectively; from left to right of the equation. Also x is the length, y is the width and A is the total area of each cell in the module ($A_i = x_i y_i$). In optimized single cells, the power loss of the top electrode (metallic in general), $P_{T.Elec}$, and of the contacts, $P_{Contact}$, are negligible compared to the other losses. The remaining individual power losses (per area), expressed at the maximum output power of the cell, can be written as:

$$P_{Shad} = J_{max} V_{max} x_{shad}/x_{cell} \quad \text{Equation 10}$$

$$P_{BE} = (J_{max}^2 x_{cell}^2 R_{sheet})/3 \quad \text{Equation 11}$$

$$P_{Act} = J_{max}^2 \rho_{Act} t_{Act} \quad \text{Equation 12}$$

$$P_{connect} = J_{max}^2 R_{sheet} x_{cell} x_{connect} \quad \text{Equation 13}$$

Where x_{shad} and x_{cell} are the length of the shading and the length of each cell (module pitch), respectively, R_{sheet} is the sheet resistance of the non-metallic contact (typically ITO), ρ_{Act} is the resistivity and t is the thickness of the active layer, and $x_{connect}$ is the length of interconnect.

The shading losses are directly connected to the need for interconnects from the top electrode of one cell to the bottom electrode of its adjacent cell (Figure 2-3). Although it is tempting to decrease the shading loss by increasing the length of the cell, x_{cell} , (Equation 10), this increases the total power dissipation as $P_R \propto AR_S$ (Equation 14). Also the connection loss increases linearly with the area, thus it can only be reduced by making $x_{connect}$ as small as the fabrication methods allow [67, 68]. Consequently, reducing the shading losses result in increasing manufacturing costs due to the need for micro-patterning active layer and metal interconnects over large areas.

2.2.1.2 Resistive Losses in Large Area PV

One of the most important quantities to optimize the PCE of a solar cell, especially for large-area solar cells, is the total resistive power loss per unit area, P_R , which is given by [70]:

$$P_R = \frac{R_S I_{max}^2}{A} = \frac{R_S (J_{max} A)^2}{A} = A R_S J_{max}^2 \quad \text{Equation 14}$$

Evidently, the resistive power loss per unit area is directly proportional to the total area of the device as well as its series resistance. A previous study by Choi, et al. [70]

suggests that as AR_S increases, J_{SC} , J_{max} and V_{max} all are substantially lowered, therefore causing a lower maximum power output and FF , thereby lowering the PCE in a single solar cell (see Figure 2-4).

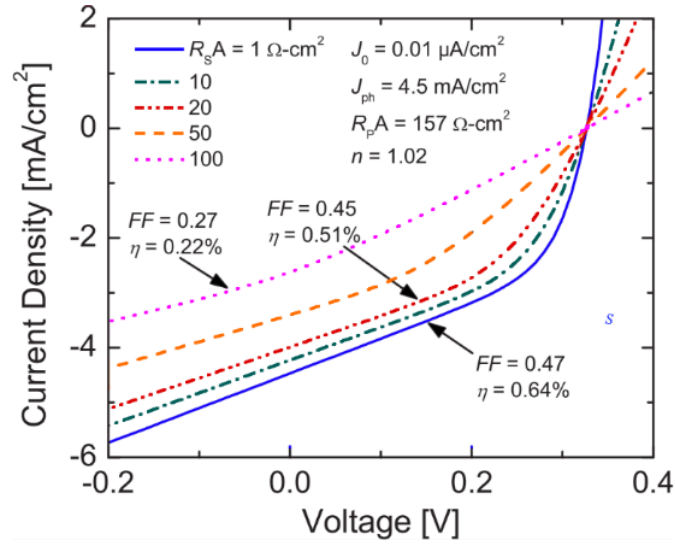


Figure 2-4: Effect of the AR_S on organic photovoltaic performance [70].

To this end, knowing where the power is lost and how the geometry and structure can affect the losses is very critical in designing of large-area PV systems.

2.2.1.3 Drop in Efficiency

As it was shown in Table 2 in section 1.3.5 (repeated here), one important issue with PV modules is that the efficiency of the modules are typically at least 20% lower than the single cell efficiency.

Table 2: Confirmed terrestrial single cell efficiencies measured under global AM1.5 spectrum (1000W/m²) at 25°C

Classification		Single cell		Module	
Technology	Material	Efficiency (%)	Note	Efficiency (%)	Note
Crystalline	Si	25.6	Panasonic HIT	22.4	SunPower
Thin-film	α -Si	10.2	ASIT	-	-
Thin-film	CIGS	20.5	Solibro	17.5	Solar Frontier
Thin-film	CdTe	21.4	First order	17.5	First Solar
Emerging	Dye	11.9	Sharp	N/A	-
Emerging	Organic	11.0	Toshiba	8.7	Toshiba
Emerging	Perovskite	20.1	Mitsubishi Chemical	-	-

This problem is particularly severe in thin-film PV technologies where minimizing power losses at the module-level require use of high-cost fabrication techniques (such as lithography, laser patterning, etc.) that seldom can be scaled-up economically to large areas. As a consequence, commercial thin-film PV modules, produced with scalable fabrication methods, typically display significant PCE losses (>20%) with respect to their single cell counterparts. Since this problem is mainly attributed to the stripe geometry, finding a better geometry for PV modules is inevitable, especially for thin-film technology.

2.3 OPV Module

Reducing shading and resistive loss mechanisms is essential to improve the PCE of large-area modules [67, 68, 71]. As these two losses are intrinsic to the arrangement of the cells, it is evident that changing the geometry is an inevitable solution to overcome these limitations. One of the main advantages of OPVs stems primarily from the promise of ease of processing through all-additive manufacturing techniques [72]. To this end, OPV can potentially address the issues, through processing and fabrication techniques that can result into OPV modules with high large-area efficiency. Since most of the layers in an OPV cell are solution processed, conventional fabrication methods such as shadow masking and photolithography cannot be easily implemented, and ultimately are not desirable to be used from a cost-reduction perspective.

Considering the complexity of a stripe-geometry PV-module, the major challenge in fabrication of an OPV-module is with no doubt the patterning of the thin-film organic layers.

2.3.1 OPV Module in Literature

Although OPV have been subject to a great amount of research [13, 47] , it is only within the last decade that OPV devices with an acceptable performance metrics (PCE higher than 4%) were achieved [73, 74]. Most of the reports on OPV modules before 2005 are therefore mainly limited to unexamined claims [75] or incomplete reports rather than actual working modules. However, in 2006 our group reported one of the very first OPV module concepts when Yoo et al. [76] demonstrated an OPV module made of 4 single cells, each with average area of 0.26 cm^2 , connected in series as it is shown in

Figure 2-5-a. In this module standard photolithography was used to pattern the bottom ITO electrodes, and shadow mask was used to define the Al top electrodes. The PEDOT:PSS layer was spin-coated without any patterning. The grade of PEDOT:PSS used in this device had a sheet resistance on the order of $10^9 \Omega/\text{sq}$. which was large enough to avoid shorting the connected cells. In this device the active layer was manually wiped-off after spin-coating to allow the metal electrodes of one cell to be connected to the ITO electrode of the adjacent cell.

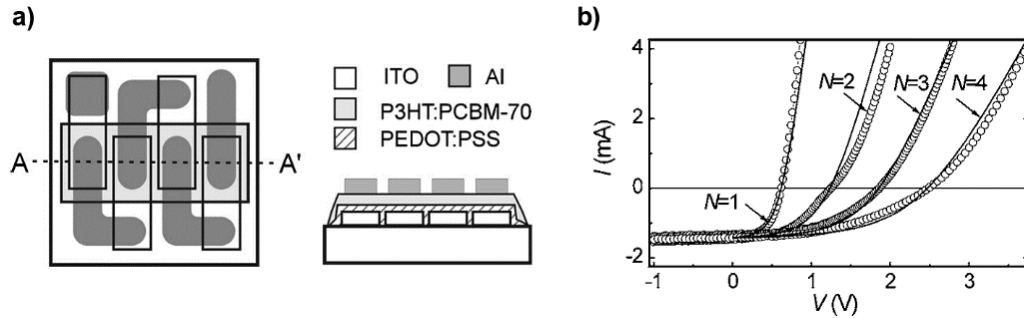


Figure 2-5: Schematic of the OPV module made by Yoo et al., a) top and side views, b) Output characteristic of the module consisting of a series connection of N individual cells ($N = 1, 2, 3,$ and 4) measured in air under illumination (AM1.5 G, $85 \text{ mW}/\text{cm}^2$) [76]

As it is shown in Figure 2-5-b, the V_{OC} scales linearly with the number of series connected cells, while I_{SC} stays almost constant. As the number of series connected cells increase, the measured FF (and PCE) decreases from 0.53 (2.2%) for $N=1$ to 0.44 (1.7%) for $N=4$. The PCE value of the 4-cell module, 1.7%, is much lower than the efficiency of 6.6% for smaller size (0.01 cm^2) reported in the same study [76]. These large losses are mainly due to the fact that the configuration of this module is the same as the conventional stripe geometry (refer to Figure 2-3) with large overall series resistance. In

2007 our group reported on encapsulation of the same OPV module using ALD deposition of Al_2O_3 which showed an acceptable air stability of the module. The ALD process also improved the V_{OC} and PCE of the device because of extra thermal annealing during deposition [77].

In 2007, Zimmermann et al. reported a new geometry called “wrap through organic solar cell” as a conceptual design for reel-to-reel production of OPV modules [78]. A series connection of 2 cells is shown in Figure 2-6. Their proposed geometry, once again, greatly suffers from the effects of a high series resistance which resulted in 50% reduction in efficiency for only 2-cell module.

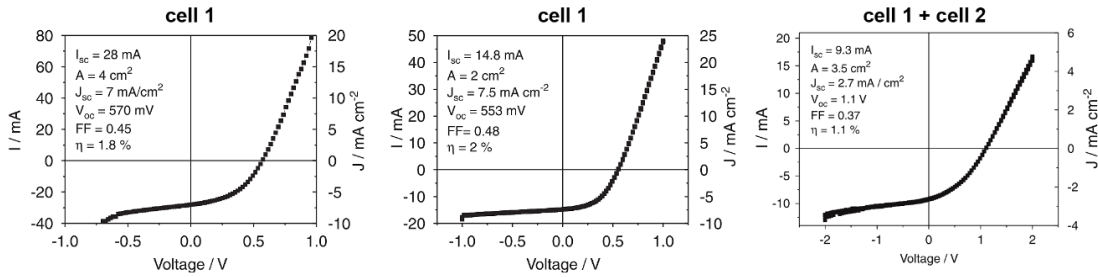


Figure 2-6: The I - V characteristics of “wrap through” single cells reported by Zimmermann et al.

In 2011 Zimmermann et al. dropped this original idea and focused on conventional stripe geometry, however they did not disclose any details of their module [79]. Later in 2009 Lewis et al. reported an interdigitated organic solar cell array made patterned bottom ITO electrode, spin-coated P3HT:PCBM and thermally evaporated top Al electrodes using shadow mask with single cell size of 0.1 mm^2 [80]. This device (shown in Figure 2-7) also suffered from a high series resistance – because of the stripe geometry – and resulted in a PCE value of less than 0.06% for 18 cells in series. Although no

specific value was reported, poor FF and high series resistance is evident from the shape of the I - V characteristics (Figure 2-7a).

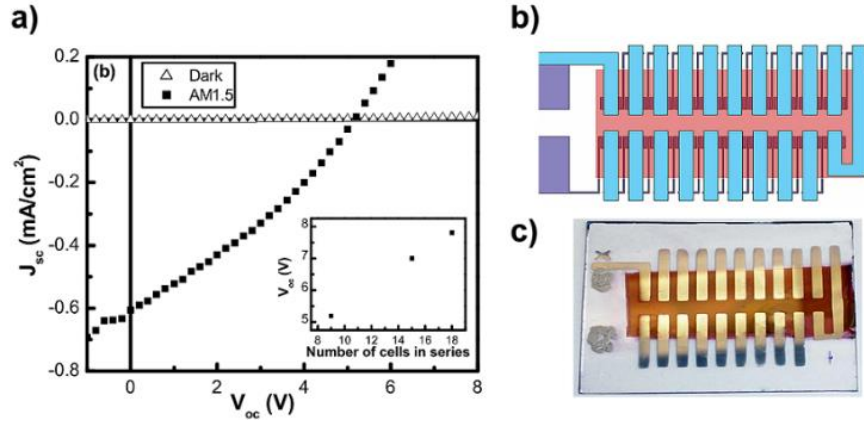


Figure 2-7: Module reported by Lewis et al., a) J - V characteristic of an array of 9 cells connected in series, b) schematic of the interdigitated array of 20 single cells, and c) picture of fabricated array [80].

Hauch et al. demonstrated another OPV module made of P3HT:PCBM with stripe geometry with more than 1 year of outdoor lifetime [81], however they did not report on any performance metric values of their module. In 2009, Tipnis et al. from Plextronics Inc. reported on an encapsulated large area NREL certified OPV module made of P3HT:PCBM with 233 cm² total area (108 cm² actual active area). This module exhibited 1.1% total area efficiency (2.4% active area efficiency) which is much lower than typical P3HT:ICBA single cell devices [65].

Overall, majority of the reported OPV modules in the literature are based on conventional stripe geometry [65, 69, 82, 83] with low PCE values which is a result of high power loss mainly because of the high series resistance and shadowing effects. A number of studies have been done on area-scaling of organic solar cells [70] as well as

modeling of electrical power losses for large area monolithic OPV modules [67, 68, 71, 84]. Choi et al. studied the effect of cell size on the overall performance by comparing heterojunction organic solar cell devices based on pentacene/C₆₀ with areas ranging from 0.13 to 7 cm². This study showed that smaller area devices had a FF of 0.54 and a PCE of 1.2%, whereas the FF of the larger cells decreased by 50% to 0.29 (compared to 0.54 of the small-size cell) and the PCE significantly decreased to 0.41% [70].

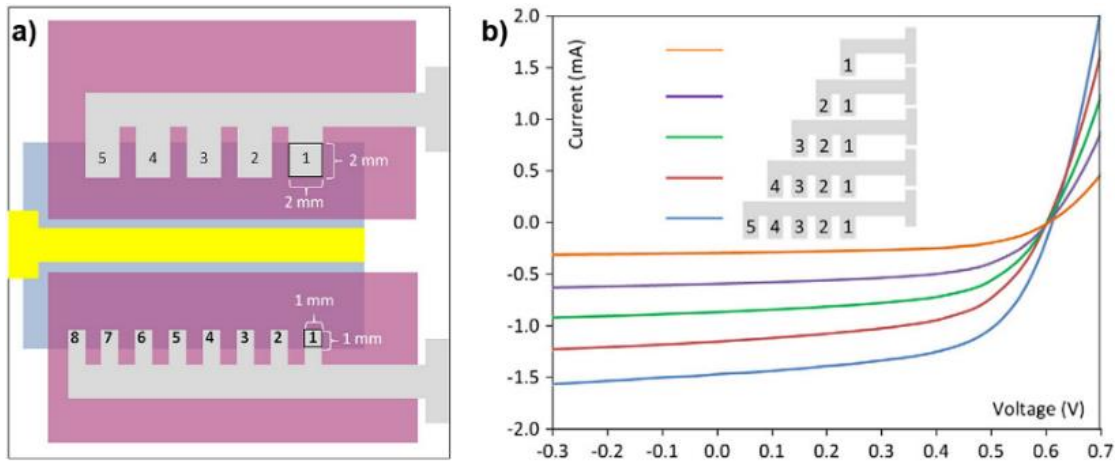


Figure 2-8: Linear pixel array of OPV module reported by Liao et. al, a) schematic of two linear pixel arrays made of 5 and 8 cells with areas of 4 and 1 mm² respectively, and b) *I-V* characteristics of the 5 cell array.

In regard to use of fabrication techniques that are more in line with printed electronics technology, there are a number of reports on partially inkjet [85] or gravure [43, 86] printed OPV modules. To address the energy loss in large area OPV cells which is due to series resistance, Liao et al. in 2011 reported a concept OPV module based on a linear pixel array of small OPV cells [87]. As it is shown in their OPV module made of a parallel connection of small-size individual cells. Their module exhibited an average PCE

of about 2.6% with V_{OC} of 0.61 V, J_{SC} of 7.8 mA/cm² and FF of 0.55. The main drawback of their design however is the poor utilization of the substrate (the actual active area versus the overall area of the substrate).

In another effort, Kang et al. recently reported a number of OPV modules with focus on the effect of cell size (wide vs. narrow cells) on the overall performance of the module [88]. Although a number of size variations is demonstrated in this study, the overall PCE in these OPV modules are slightly above 1% with FF values below 0.43. Using an industrial gravure printing machine, Yang et al. reported a highly reproducible roll-to-roll OPV module made of P3HT:PCBM with 5 cells in series (stripe geometry) with overall PCE of over 1.0%, module V_{OC} of 2.74 V, J_{SC} of 7.14 mA/cm² and FF of 0.26 [86].

The current state of the art OPV module, and the closest (in terms of geometry) to what is being proposed in this document is the one reported by Lee et al. in 2013 [89]. In this module an array of alternating conventional and inverted individual organic solar cells are serially connected. Their device showed an efficiency of 4.24% for the large-area module which is 82% of the small-size single cell (with 5.19% PCE).

2.3.2 Scalable Fabrication: Printed Electronics

The traditional micro-fabrication technology based on crystalline rigid materials has several practical limitations. Complexity of the processes, limited range of compatible materials, difficulty of patterning large areas, rigidity of substrates and overall high cost are examples of the limiting factors [90, 91].

Organic electronics however is based on solution processing and has several advantages over the traditional micro-fabrication techniques. Compatibility with light weight, flexible and large area applications, as well as low cost, low energy fabrication method are some the most important advantages of such techniques [44, 91]. As a result of all these advantages, multidisciplinary field of printed electronics has come to existence with an aim to provide an efficient and high throughput processing for large area, low cost and low energy fabrication. Fabrication of electronic devices and complex electronics structure requires precise patterning of semiconductor, conductor and dielectric materials and to achieve this, printed electronic utilizes variety of different printing techniques such as screen printing, gravure printing, and inkjet printing.

2.3.2.1 Screen Printing

There are two types of screen-printing methods: flat bed and rotary, with their operation principle shown in Figure 2-9. In both methods, the screen contains the opening for the pattern, and squeegee moves against this screen and presses the “ink paste” through the pattern openings into substrate. The key elements in this technique are, but not limited to: ink viscosity, substrate wetting, and speed. While in flat-bed printing large areas of up to 10 m² can be printed, the rotary technique is a real “role-to-role.” This method can have the resolution down to 70 μm [90]. Screen printing is very attractive due to its simplicity, and compatibility with a large group of organic inks, and allows for low-cost printing on flexible substrates. This technique has been used for printing solar cells and organic field-effect transistors (OFETs) [92, 93].

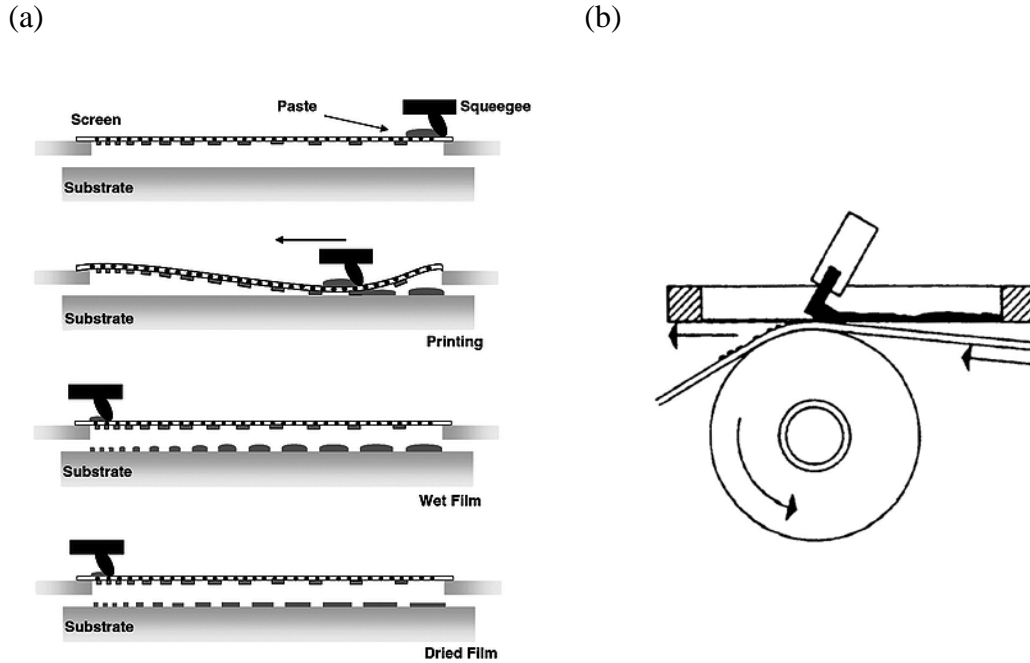


Figure 2-9: Illustration of screen printing processes: (a) flat-bed, and (b) rotary techniques.

2.3.2.2 Gravure Printing

In gravure printing, the desired pattern is engraved on a cylinder. This cylinder is continuously rotates in the ink bath and the ink is doctored in the engraved patterns. It then rotates against another cylinder that feeds the substrate, therefore the ink will be transferred to the substrate. The operation principle of this technique is shown in Figure 2-10. Gravure printing is one of the most cost-effective techniques due to its high speed (typically up to 1 m.s^{-1}) [43, 91]. The resolution could also be from tens of micrometers down to few nanometers. The properties of the gravure cylinder, such as cell density, screen angle, depth width and stylus angle have great impact on the quality of the printed pattern. The inks used in this technique must have a very low viscosity ($0.05 - 0.2 \text{ Pa.s}$) [94].

Like rotary screen printing, the gravure printing is a real role-to-role fabrication method and has been used in fabrication of variety of organic electronic devices [43, 44, 86, 95].

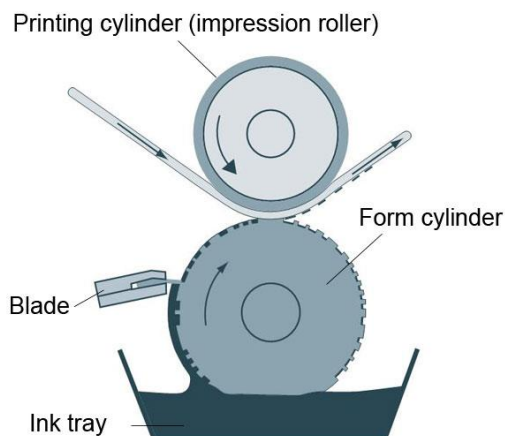


Figure 2-10: Illustration of gravure printing method.

2.3.2.3 Inkjet Printing

Inkjet printing of organic materials has been one of the most attractive techniques for industrial and academic applications. In contrast to the other two aforementioned printing techniques, ink jet printing is a “mask-less” and “non-contact” method, thus offers a real-time design modification, and reduces the substrate contaminations [90, 95, 96]. Inkjet printing also offers an accurate deposition of wide range of organic materials for large-area and low cost manufacturing.

The two main modes of inkjet printing are “drop-on-demand” (DOD) and “continuous.” In continuous mode, a steady stream of ink is ejected from the nozzle and forms a liquid jet. The surface tension of the ink material breaks this stream into a

uniformly spaced and sized droplets (see Figure 2-11). In DOD mode, acoustic pulses - generated either by heat or by piezoelectric - pumps the ink through a nozzle and forms droplets. DOD inkjet printing provides a smaller droplets and higher accuracy [90].

In thermal inkjet printing, the ink temperature inside the reservoir is increased to create expanding bubbles that in turn pump the ink out of the nozzle. In piezoelectric-based inkjet printing, a train of electrical pulses are applied to the piezo element to generate impulses that change the volume of the ink chamber inside the nozzle. The main advantage of piezo-based nozzles is that there is no need to extra heat and this allows for using a wide variety of solvents.

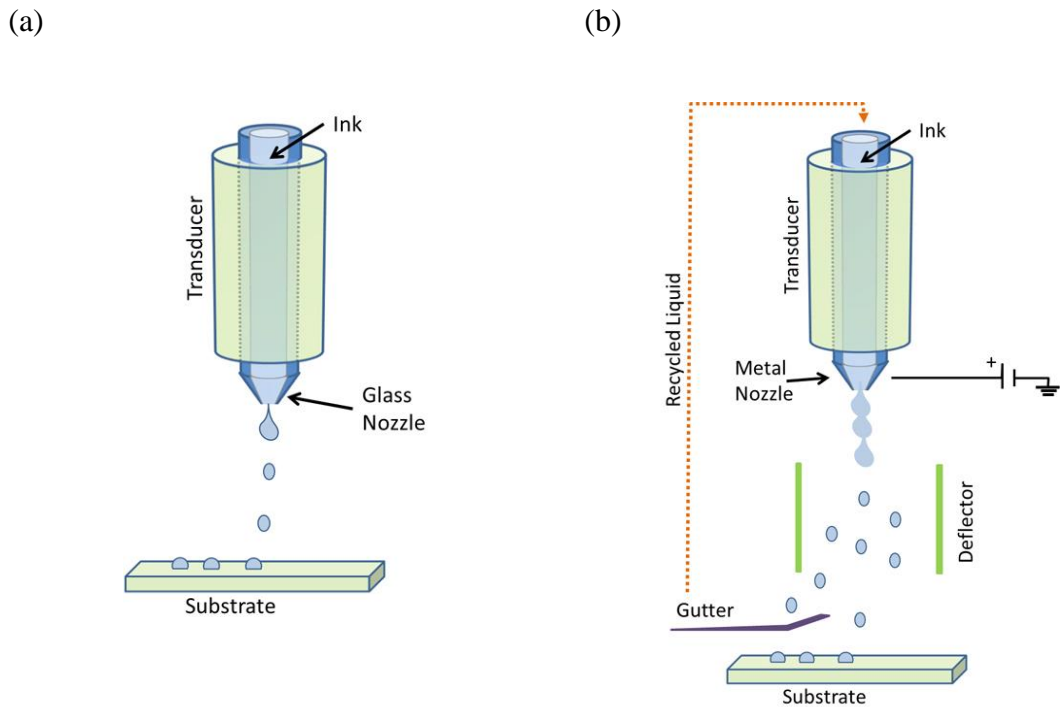


Figure 2-11: Illustration of inkjet printing techniques: (a) drop-on-demand, and (b) continuous techniques.

Stability of ink and drop formation (jet-ability) are two the most important factors determining the quality and resolution of inkjet printed patterns. The resolution of this technique is typically 30-100 μm [90, 95].

Inks used in inkjet printing must meet very restrictive criteria. For inks to be jet-able, inkjet printers typically require a very narrow range of viscosity (2-25 mPa.s) and surface tensions (30-35 mN/m) [90]. This makes the formulation of inks a very critical and important step in inkjet printing process. Moreover, the compatibility of solvents, and wetting of substrates can make the formulation of ink a quite challenging task.

CHAPTER 3: ORGANIC PHOTOVOLTAIC MODULE

3.1 Proposed OPV Module

With the goal of minimizing the power losses that currently limit the power conversion efficiency in PV modules with conventional geometry (stripe geometry), in this section an OPV module with a new geometry is demonstrated that could potentially result in a near zero efficiency drop from single cell to module. This can be realized by exclusive patterning of the interlayers and electrodes and by avoiding patterning of the active layer

3.2 Geometry and Operation

As it was discussed before, the shading and series resistance are two of the most important losses in a PV module with stripe geometry [15]. In recent years, variety of different techniques and geometries have been reported with an aim to minimize losses and improve techniques for fabrication of PV modules [65, 76, 78-80, 86-88]. Kippelen et al. [97], and Hall et al. [98], have independently invented a module geometry that can fundamentally transform the stripe geometry into a different configuration with the potential of significantly reducing losses in PV modules. Figure 3-1 shows schematics of this new geometry.

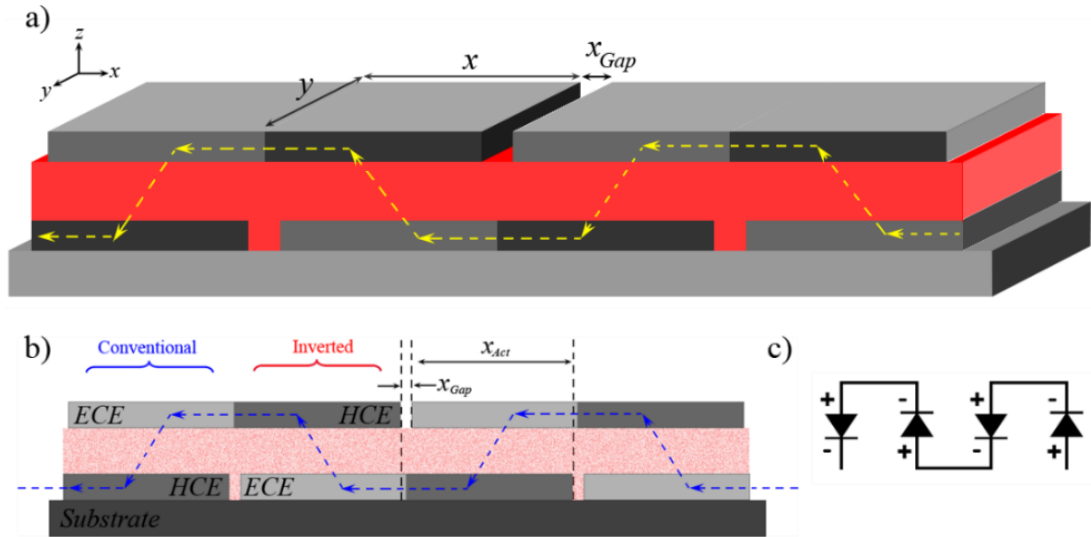


Figure 3-1: Schematic of the proposed OPV-module: a) Three dimensional representation of a 4-cell module, b) Active length vs. gap length of the unit cell, c) Circuit diagram of the OPV-module.

In this geometry, the polarity of adjacent cells is engineered to be opposite and alternating. Herein, the polarity of a cell is defined by the direction in which holes and electrons are collected with respect to the substrate. In this module configuration, each electrode (top and bottom) is shared between two adjacent cells with opposite polarities; in other words, a cell with a conventional geometry (having a hole-collecting electrode at the bottom) is followed by a cell with an inverted geometry (with an electron-collecting electrode at the bottom), and so on.

The most important advantages of this geometry versus the conventional stripe geometry are (see Figure 3-2):

- a) The inter-plane interconnects are avoided and consequently “dead areas” and parasitic resistance effects are greatly minimized,

- b) losses due to inter-cell gaps can be reduced arbitrarily within the intrinsic resolution and constrains of the fabrication process of the electrodes, making it aesthetically more appealing for building-integrated PV applications, and
- c) the active layer does not need to be patterned, which could reduce fabrication costs and prevent other parasitic effects.

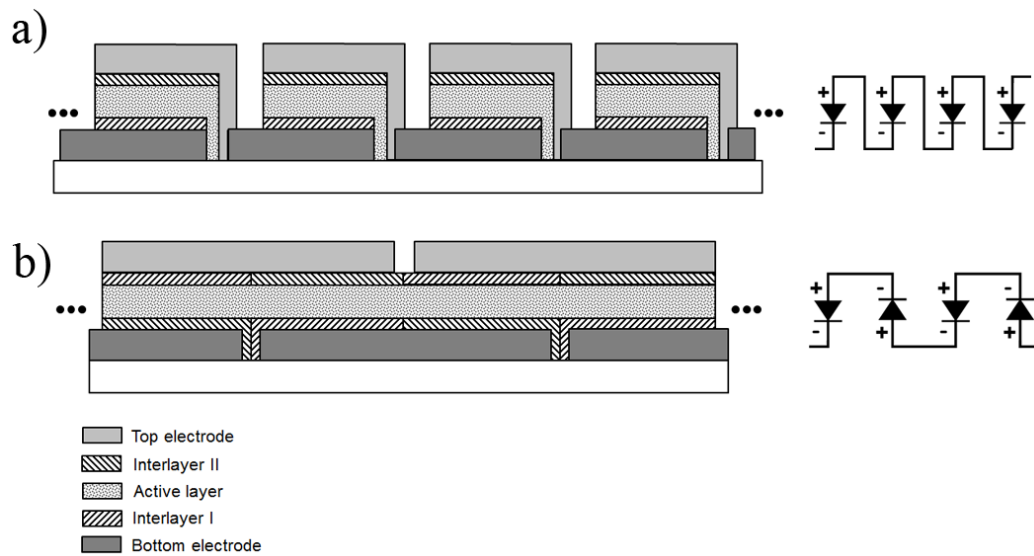


Figure 3-2: Schematic of a two different PV modules: a) conventional “stripe” geometry and b) the alternative geometry consisting of adjacent solar cells with alternating polarities.

The realization of such architecture, depends upon realization of PV cells with opposite polarities (inverted and conventional) with comparable performances. Consequently, the selection of the right interlayers to tune the work function of electrodes to enable electrons and holes to be collected on adjacent areas of one electrode is critical. Recently, we have demonstrated that the combination of Poly(3,4-ethylenedioxythiophene):poly(styrenesulfonate) (PEDOT:PSS) and ethoxylated

polyethylenimine (PEIE) can lead to high-efficiency single cell and tandem organic PV devices in both conventional and inverted geometries [60, 99].

The final module configuration that we plan to fabricate is shown in Figure 3-3:

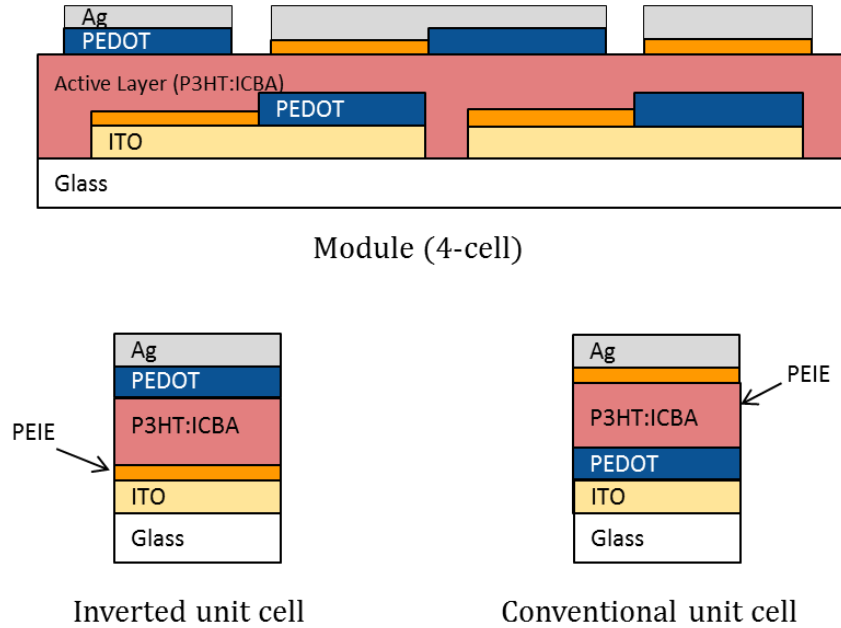


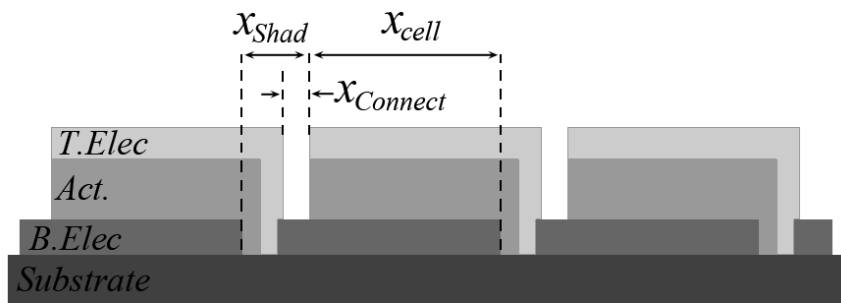
Figure 3-3: Schematic of the proposed new geometry as it is planned for fabrication

This device is a four-cell module composed of an alternative arrangement of inverted (ITO/PEIE/P3HT:ICBA/PEDOT/Ag) and conventional (ITO/PEDOT/P3HT:ICBA/PEIE/Ag) fabricated on a glass substrate. As it is evident from Figure 3-3 schematic, patterning of different layers is the key to realize this geometry.

3.3 Losses in New Geometry

To analyze losses, a side by side comparison between a module with stripe geometry and a module with the new geometry would be helpful. As it is shown in Figure 3-4, in the new geometry the shading losses become independent of the active area length and the interconnection losses are completely avoided.

(a)



(b)

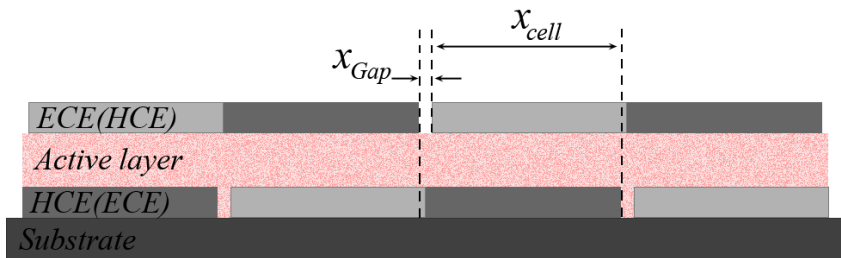


Figure 3-4: Schematic comparison between (a) module with stripe geometry, and (b) module with new geometry. In new geometry the shading losses become independent of the active area length and the interconnection losses are completely avoided.

Repeating from section 2.2.1.1, the components of resistive losses in stripe geometry are:

$$P_{Shad} = J_{max} V_{max} x_{shad}/x_{cell} \quad \text{Equation 10}$$

$$P_{BE} = (J_{max}^2 x_{cell}^2 R_{sheet})/3 \quad \text{Equation 11}$$

$$P_{Act} = J_{max}^2 \rho_{Act} t_{Act} \quad \text{Equation 12}$$

$$P_{connect} = J_{max}^2 R_{sheet} x_{cell} x_{connect} \quad \text{Equation 13}$$

Utilizing the new geometry, the shading loss (P_{Shad}) will be eliminated, therefore the total power loss per area of the module now will be:

$$P_{Total/Area} \cong \sum_N (P_{Act,i} + P_{B.Elec,i} + P_{Gap,i}) \quad \text{Equation 15}$$

Where P_{Gap} is the loss associated with the gap between electrodes (Figure 3-4). In an attempt to get a better understanding of losses in module with new geometry, first the module is split into its sub-cell units (Figure 3-5).

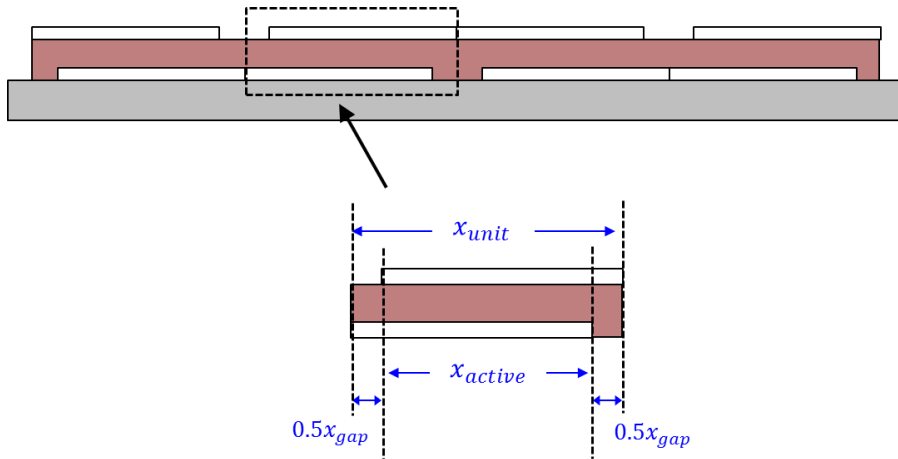


Figure 3-5: Schematic of the module and its sub-cell.

Where x_{unit} is the total sub-cell length including the gap, x_{gap} , and x_{active} represents the length of the unit cell where electrodes overlap ($x_{active} = x_{unit} - x_{gap}$). Rewriting the power losses per unit area, we have:

$$P_{BE} = (J_{max}^2 x_{active}^2 R_{sheet})/3 \quad \text{Equation 16}$$

$$P_{BE_gap} = (J_{max}^2 x_{active} x_{gap} R_{sheet})/2 \quad \text{Equation 17}$$

$$P_{BE_gap_no_gen} = \frac{V_{max}}{J_{max}} \frac{x_{gap}}{(x_{active} + x_{gap})} \quad \text{Equation 18}$$

Where P_{BE} is the resistive loss due to the bottom electrode. The top electrode is typically metallic with negligible losses. Since in this new geometry the photoactive layer is not patterned, and the gap areas are filled with photoactive material, the power loss due to the gaps between electrodes, P_{Gap} , is not easy to formulate. However in a simplified approach, losses associated with gap can be divided into two parts:

- 1) P_{BE_gap} is a resistive loss due to part of the bottom electrode that constitute half of the gap ($0.5x_{gap}$ in Figure 3-5), and
- 2) $P_{BE_gap_no_gen}$ which is a loss “presumably” due to no photocurrent generation (over two $0.5x_{gap}$ lengths in both side of the sub-cell in Figure 3-5). This is similar to loss model for shading loss in stripe geometry and very conservative. In reality the photoactive material inside the gap could possibly contribute to the overall current; particularly if the gap size is significantly reduced. This requires more experimental investigation.

3.4 Module Efficiency Definitions

To calculate the total area efficiency, all the sub-cell active areas (areas under the electrodes) and the dead areas (gaps) are included in calculation of current density. For module “active area efficiency” however the dead areas are excluded, which in turn results in a higher efficiency values.

CHAPTER 4: OPV MODULE MICROFABRICATION

4.1 Trial 1: OPV Module: Proof of Concept

To prove the concept of the design, first a 4-cell module was fabricated by using spin-coating and thermal evaporation through shadow-masks (shown in Figure 4-1). In this configuration Molybdenum oxide (MoO_x) is used instead of PEDOT:PSS as the hole transfer material, because it can be thermally evaporated and patterned through shadow mask. To pattern the PEIE layer, we used 2 mm-thick pieces of Polydimethylsiloxane (PDMS) film to protect the desired areas in the module, then spin-coated the PEIE.

The area of the sub-cells in this device was 1 cm^2 (0.5 cm by 2 cm) with gap size of $500\text{ }\mu\text{m}$ which resulted in a total area of 4.2 cm^2 (2.1 cm by 2 cm) for the four-cell module. The details of fabrication processes are described in the following section.

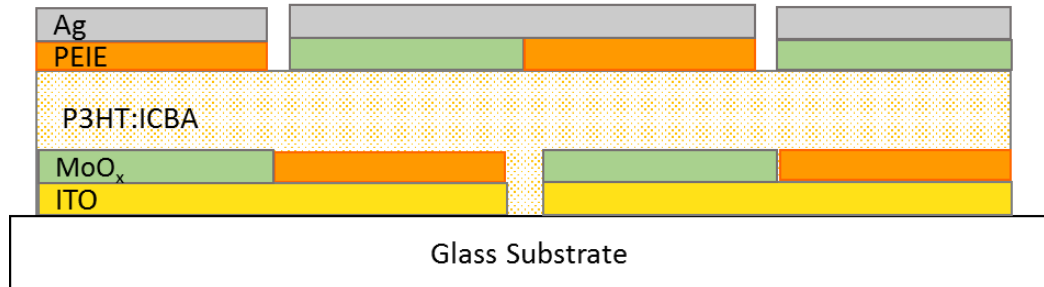


Figure 4-1: The proof of concept module using thermally evaporated MoO_x (through shadow mask) and spin-coated PEIE (patterned using PDMS film)

4.1.1 Microfabrication of Module

Step 1 (patterning ITO): An indium tin oxide (ITO)-coated glass (Colorado Concept Coatings LLC) with a sheet resistivity of c.a. $15 \Omega/\text{sq}$. was used as substrate. First, 10 nm of Ti, followed by 60 nm of Au were deposited on the substrate through shadow mask to serve as alignment marks. The ITO substrates then were patterned with photolithography and etched inside acid solution (4:2:1 by volume, HCl:H₂O:HNO₃) for 5 min at room temperature. The patterned substrates were cleaned in an ultrasonic bath of detergent water, rinsed with deionized water, and then cleaned in sequential ultrasonic baths of deionized water, acetone, and isopropanol. Nitrogen was used to dry the substrates after each of the last three baths. Then, the substrates were treated in a reactive ion etcher (Oxford End-point RIE) for 5 min at 100 W power and 100 sccm O₂ to remove any remaining organic contamination and to improve the surface wettability.

Step 2 (first PEIE): First the desired areas of the module were covered with pieces of 2 mm-thick Polydimethylsiloxane (PDMS) films. Then Polyethylenimine, 80% ethoxylated (PEIE) ($M_w = 70,000 \text{ g/mol}$) was dissolved in H₂O with a concentration of 35-40 wt.% when received from Aldrich. Then, it was diluted into 2-methoxyethanol to a weight concentration of 0.4 wt.%. Then the PEIE was spin-coated at a speed of 5000 rpm for 1 min and at an acceleration of 1000 rpm/s, then the PDMS films were removed and the sample was annealed at 120 °C for 10 min on a hot plate in ambient air. The thickness of PEIE was 5 nm determined by spectroscopic ellipsometry (J. A. Woollam Co., M-2000UI).

Step 3 (first MoO_x): The sample was covered by a shadow mask and loaded in to Spectros thermal evaporator (Kurt J. Lesker Co.) and a 20 nm-thick MoO_x film was deposited, through the shadow mask.

Step 4 (photoactive): The substrates were transferred into a N₂-filled glove box. The active layer of poly(3-hexylthiophene) (P3HT, 4002-E, Rieke Metals): Indene-C60 Bis-Adduct (ICBA, Lumtec) (1: 1, weight ratio) was filtered through 0.2- μ m-pore PTFE filters and spin-coated on each substrate from 40 mg/ml dichlorobenzene solution at a speed of 800 rpm for 30 s and an acceleration of 1000 rpm/s. Then the active layers were treated through solvent annealing for 4 hours and thermally annealed at 150 °C for 10 min on a hot plate inside the glove box. The thickness of the active layer was 200 nm, measured by spectroscopic ellipsometry.

Step 5 (second PEIE): first the sample was covered with pieces of PDMS film to cover the desire areas. Then it was treated with O₂-plasma for 1 s to improve the wettability of the P3HT:ICBA film. Then a layer of 0.05 wt% PEIE in 2-methoxyethanol was spin-coated at a speed of 5000 rpm for 1 min and at an acceleration of 1000 rpm/s. Then the PDMS films were removed and the sample was annealed at 120 °C for 10 min on a hot plate inside N₂-filled glove box.

Step 6 (second MoO_x): After sample cooled down for 30 min inside N₂-filled glove box, it was covered with the second shadow mask with extra caution not to damage the photoactive layer. The sample then was transferred back into Spectros thermal evaporator and a 20 nm-thick MoO_x film was deposited on top of the photoactive layer.

Step 7(top metal contact): Finally through the third shadow mask a 100-nm thick silver layer was deposited as a top contact using Spectros thermal evaporator.

4.1.2 Results and Discussion

Current density-voltage (J - V) characteristics were measured inside the N_2 -filled glove box by using a source meter (2400, Keithley Instruments, Cleveland, OH) controlled by a LabVIEW program. To test the solar cell properties under illumination, an Oriel lamp with an AM 1.5 filter and an irradiance of 100 mW/cm^2 was used as the light source. The result of a four-cell module measurement under illumination is shown in Figure 4-2. The module showed a V_{OC} of 2.71 V, which was equal to the sum of all the V_{OC} 's of the unit cells, J_{SC} of 0.91 mA/cm^2 , the FF of 0.46 and the PCE of 1.14%, thus validating the module design. Although the sub-cells performance is not uniform and overall not that impressive, the FF of the module appears to be equal and better than the FF of the sub-cells. This is a very important result because when a series connection of sub-cells should increase the overall series resistance, and consequently decrease the FF of the module.

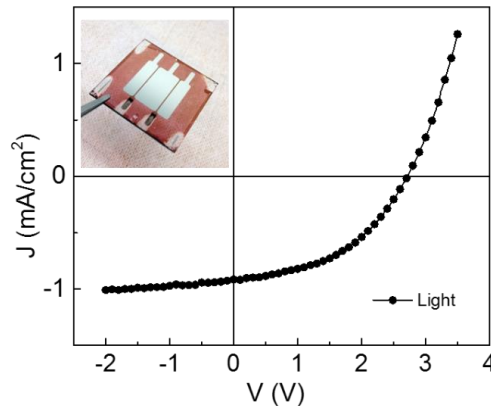


Figure 4-2: J - V characteristic of the proof-of-concept four-cell module under AM 1.5 100 mW/cm^2 illumination. The inset is a picture of the module.

Table 5 also summarizes the PV performance metrics of the sub-cells as well as of the module.

Table 5: PV performance of the four-cell module and its inverted (ITO/PEIE/P3HT:ICBA/MoOx/Ag) and conventional (ITO/MoOx/P3HT:ICBA/PEIE/Ag) sub-cells under AM 1.5 100 mW/cm² illumination.

Sample	V_{oc} (V)	J_{sc} (mA/cm ²)	FF	PCE (%)
Inverted single	0.82 ± 0.00	3.89 ± 0.04	0.45 ± 0.01	1.46 ± 0.01
Conventional single	0.52 ± 0.01	3.16 ± 0.06	0.36 ± 0.02	0.59 ± 0.03
Module (active area)	2.71	0.91	0.46	1.13
Module (total area)	2.71	0.89	0.46	1.11

4.2 Trial 2: OPV Module: Photolithography

Photolithography is the conventional technique used to pattern thin films in micro-fabrication of electronic devices. This technique offers great resolution and precise patterning for complex structures, and requires several steps of chemical wet processing (photoresist deposition, development, and removal) [100]. These standard photoresist chemistries are based on organic solvents and aqueous developers.

These solvents are generally incompatible with organic materials, due to high possibility of imposing damage and contamination to the organic films, therefore making standard lithographic processes unsuitable for manufacturing organic electronics. Nonetheless, resolution, registration, and yield that are offered by industry standard

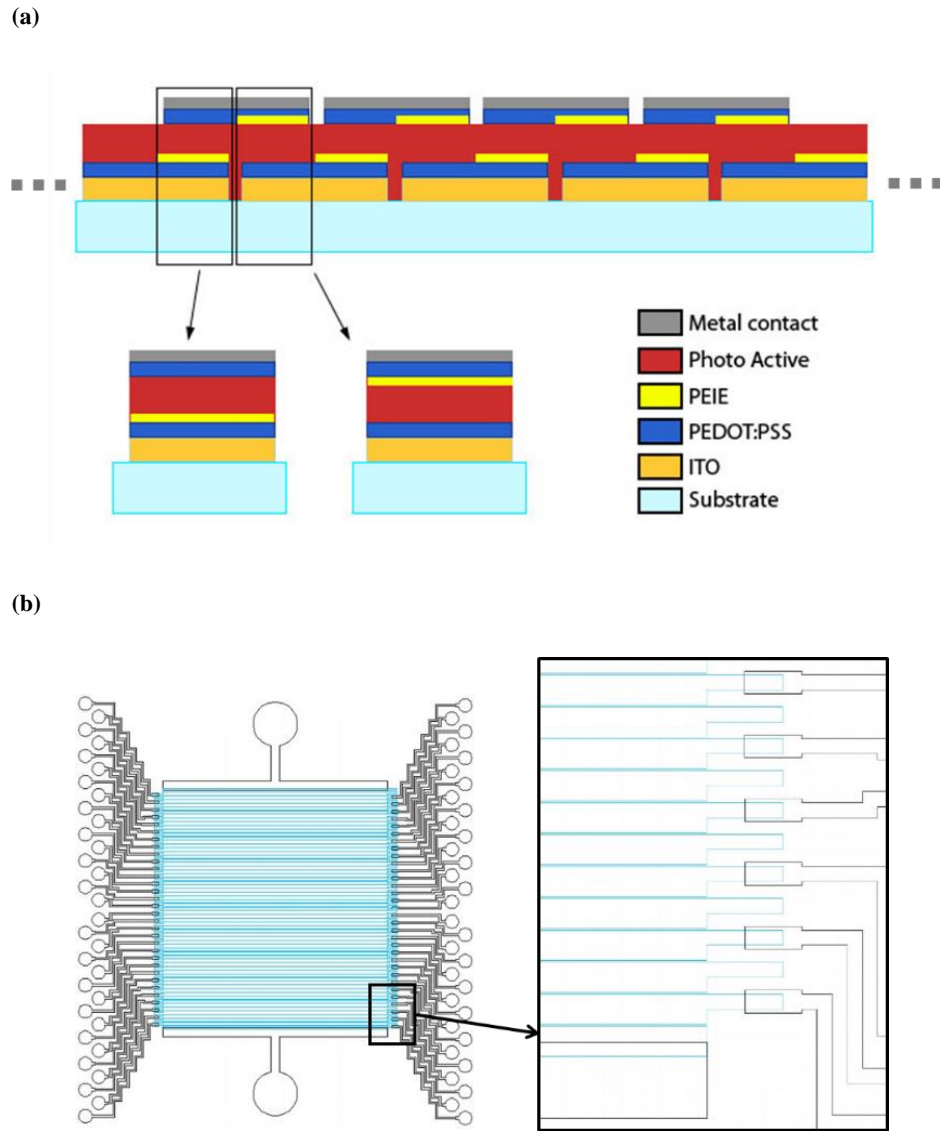


Figure 4-4: (a) The cross sectional schematic of the module structure designed for photolithography, and (b) the top view of the design.

As it is shown in Figure 4-4-a, this design is composed of 7 layers. To pattern these 7 layers, we required minimum of 8 photolithography steps (including patterning the alignment marks).

4.2.1 Photolithography Recipe for OSCoR 2312 Photoresist

Each photolithography layer, included multiple processing steps which are listed below:

Step 1 (spin-coating the photo-resist): spin-coating at 1000 rpm for 60 s with 1000 rpm/s gives a 1100 nm-thick film of photoresist.

Step 2 (soft baking): On a hot plate for 4 min at 90°C, followed by a 4 min cool down. This step is necessary to remove extra solvent from the film. By increasing (decreasing) the time or temperature of soft-baking step, the exposure time must be reduces (increased).

Step 3 (exposure): At 365 nm light for approximately 110 mJ/cm² for every 1 μm thickness of photoresist film.

Step 4 (post-backing): On hot plate, preferably covered, for 4 min at 75°C, followed by 4 min cool down.

Step 5 (developing): 4 min in developer solution with occasional stirring, after this time, the sample must be dried using N₂.

Step 6 (removal): after patterning the target film, the sample goes to remover for at least 60 s or until the photoresist is completely dissolved.

4.2.2 Patterning PEDOT:PSS Layer

After patterning the alignment marks and ITO contacts (through lithography steps), the next layer to pattern was PEDOT:PSS. The first attempt to pattern the PEDOT:PSS was via lift-off. In this process, first the pattern was transferred on the ITO layers by following sequential lithography steps (see section 4.2.1), then to remove possible residues of photoresist and to improve the wettability of the surface the sample was treated in a reactive ion etcher (Oxford End-point RIE) for 5 s at 100 W power and 100 sccm O₂.

Immediately after that, a layer of PEDOT:PSS with 5 wt% dimethyl sulfoxide (DMSO) was spin-coated on top of the photoresist pattern at a speed of 1000 rpm for 20 s and an acceleration of 1000 rpm/s. The thickness of PEDOT:PSS layer was about 100 nm. The film was then annealed on top of a hot-plate in ambient air at 100 °C for 10 min. It is worth to mention that the temperature and the time of the annealing both were intentionally decreased to reduce the chance of affecting the photoresist properties. Then the sample were let to cool down for at least 10 min following that, the sample were transferred into the stripper solution for 60 s with occasional stirring.

This process and the final result are shown in Figure 4-5.

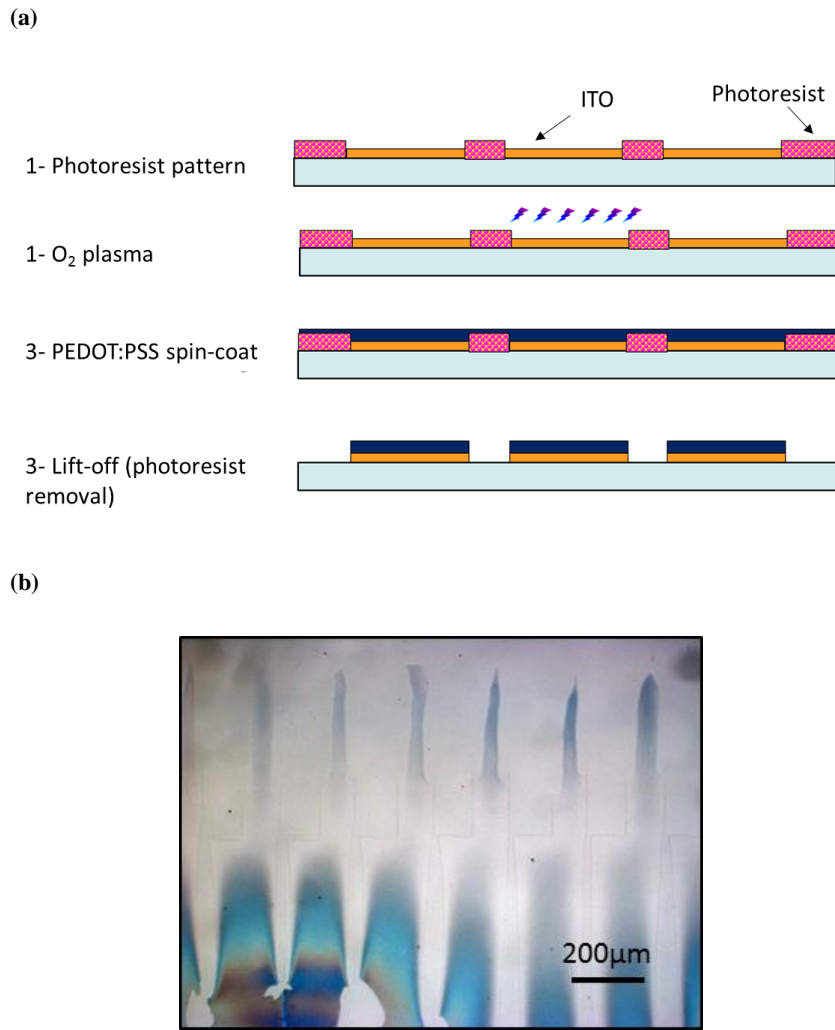


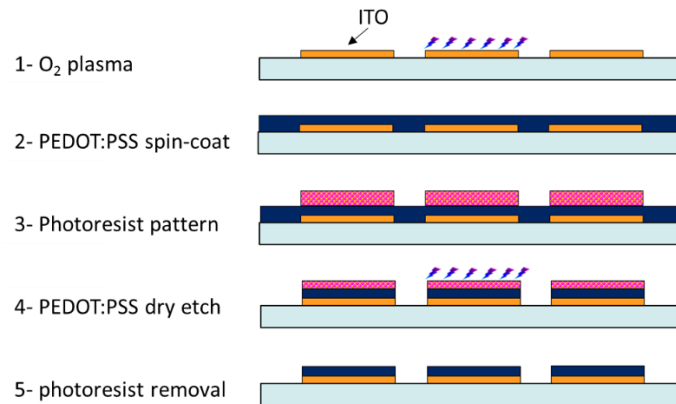
Figure 4-5: (a) Lift-off process for patterning PEDOT:PSS film using OSCoR 2312 Photoresist and (b) its final result.

The PEDOT:PSS is a water based dispersion while the photoresist film was extremely hydrophobic, therefore spin-coated PEDOT film on top of photoresist did not have a strong enough adhesion to the substrate, which resulted in peel-off of the PEDOT:PSS film during the lithography process as it is shown in Figure 4-5-b.

Dry etching was another alternative to lift-off. In this process, after patterning the alignment marks and ITO layer (through lithography), next to improve the wettability of the surface the sample was treated in a reactive ion etcher (Oxford End-point RIE) for 5 min at 200 W power and 100 sccm O₂. This also helped to remove any possible contamination on the surface of the substrate. Then, a layer of PEDOT:PSS with 5 wt.% dimethyl sulfoxide (DMSO) was spin-coated on top of patterned ITO at a speed of 1000 rpm for 20 s and an acceleration of 1000 rpm/s.

The thickness of PEDOT:PSS layer was about 100 nm. The film was then annealed on top of a hot-plate in ambient air at 120 °C for 20 min. The wetting and uniformity of the PEDOT:PSS film were very good due to the effect of O₂ plasma treatment of the substrate. After the sample was left to cool down for at least 10 min, a sequential lithography steps (see section 4.2.1) was performed to create the openings on top of the PEDOT:PSS film (refer to Figure 4-6-a). Then the sample was transferred into RIE and treated for 3 min of dry etching at 100 W power and 100 sccm O₂. Under these conditions, the etching rate of the PEDOT:PSS film was about 40-50 nm/min. Since the photoresist was thicker than the PEDOT:PSS film, an 30 s up to 1 min extra etching ensures the complete removal of the PEDOT:PSS films from the desired areas. After this step the sample was transferred into the photoresist stripper for 60 s, and finally dried using N₂. The final result is shown in Figure 4-6-b.

(a)



(b)

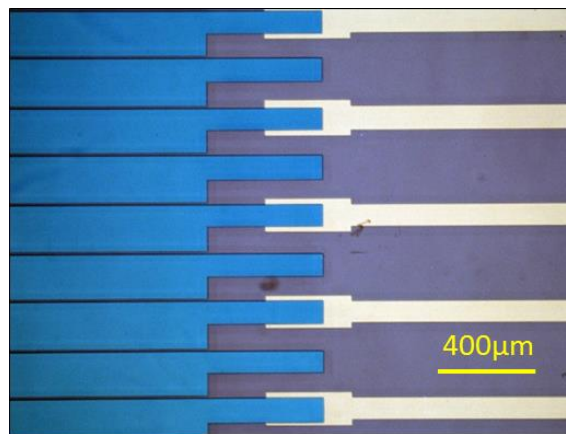


Figure 4-6: (a) dry-etching process for patterning PEDOT:PSS film using OSCoR 2312 Photoresist and (b) its final result. The blue stripes (pattern on the left) are PEDOT films on top of ITO, and the yellow stripes (patterns on the right) are ITO contact lines.

4.2.3 PEIE Layer and Contamination Issues

After successful patterning of the first PEDOT:PSS layer of the module, the next layer was the first PEIE (refer to Figure 4-4). As it was discussed before, a thin film of PEIE (typically < 5 nm) plays the critical role of work-function modification of the electrodes. Therefore any contamination – mainly due to photoresist contact – would

disrupt this work-function modification and consequently affect the OPV operation. Thus it is critical to examine the contaminations before proceeding with the patterning of the first PEIE layer.

To start, we first found out that 2-methoxyethanol appeared to be dissolving the photoresist. Considering that our original recipe for PEIE required to dissolve a Polyethylenimine, 80% ethoxylated (PEIE) ($M_w = 70,000$ g/mol) in H_2O with a concentration of 35-40 wt.% to be diluted into 2-methoxyethanol to a weight concentration of 0.4 wt.%. Therefore, we had to formulate the same concentration of PEIE solution in water instead of 2-methoxyethanol.

To perform this test, three dummy samples were prepared. One pristine PEDOT:PSS sample (100 nm-thick) without getting exposed to any photolithography process, one PEDOT:PSS sample treated with PEIE in water (100 nm-thick PEDOT:PSS with 5 nm of PEIE on top). The third sample went over a routine photolithography process (as described earlier) to create an opening pattern (a 1 cm x 1 cm square) on a photoresist film on top of a PEDOT:PSS layer. Then, the sample was treated with O_2 plasma at 100 W and 100 sccm O_2 for 5 s to remove possible photoresist residues inside the opening. Then PEIE was spin-coated on top of PEDOT:PSS/Photoresist pattern at a speed of 5000 rpm for 1 min and at an acceleration of 1000 rpm/s and annealed at 120 °C for 10 min on a hot plate in ambient air. Then, this sample was dipped into the photoresist stripper solution to remove the extra photoresist (lift off). Sample was finally dried with N_2 . All three samples then were transferred into XPS chamber to perform analysis. Figure 4-7 shows the result of XPS analysis. The strong fluorine 1s peaks in both areas of

PEDOT:PSS and PEDOT:PSS/PEIE are an indication of severe photoresist contamination.

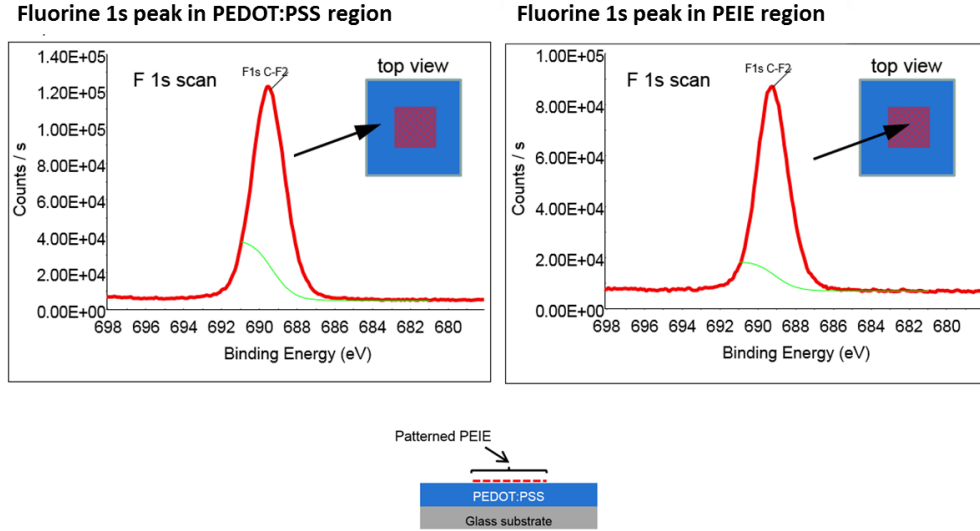


Figure 4-7: XPS analysis of PEDOT/PEIE film exposed to fluorinated photoresist. The strong fluorine 1s peak is an indication of severe photoresist contamination.

To see if this contamination had any effect on work-function modification functionality of PEIE, we also carried-out Kelvin probe test experiments on all three samples (Table 6). The results indicate that the contaminations due to photoresist residues eliminates the effect of PEIE in reducing the work function.

Table 6: Kelvin probe measurement results on three PEDOT:PSS films. The results indicates that the contaminations due to photoresist residues eliminates the effect of PEIE

Sample	Work Function (eV)
Reference PEDOT:PSS	4.5
Reference PEIE treated PEDOT:PSS	3.5
PEIE treated PEDOT:PSS after lithography	4.2

In standard photolithography, where most of the films are inorganic, it is a common practice to use UV-Ozone or RIE to strip away any possible organic contaminations such as solvent residues, photoresist, ink, from the substrate materials. These methods however are not compatible with organic materials. In this specific case, where we have an extremely thin film of PEIE, any exposure to O₃ plasma or UV-ozone would completely remove the PEIE from the surface. Therefore, despite a successful patterning of PEDOT:PSS, the contamination of PEIE with fluorine residues put an end to our photolithography trial.

4.3 Trial 3: OPV Module: Solution Processing

Solution processing of organic materials benefits from the ease of fabrication and it is compatible with large area applications (see section 2.3.2). In this regard, and as it was discussed in section 3.2, the next trial was to fabricate the proposed module geometry using solution processing. The final module configuration that we planned to fabricate is shown in Figure 4-8. This four-cell module composed of inverted (ITO/PEIE/P3HT:ICBA/PEDOT/Al) and conventional (ITO/PEDOT/P3HT:ICBA/PEIE/Al) sub-cells, fabricated on glass substrate.

Here, we use PEDOT:PSS and PEIE interlayers: PEDOT:PSS is used for hole collection because it has a high work function of 5.0 eV, and PEIE is used to lower the work function of conductors either on top of the conductors or beneath to facilitate the electron collection for corresponding electrodes.

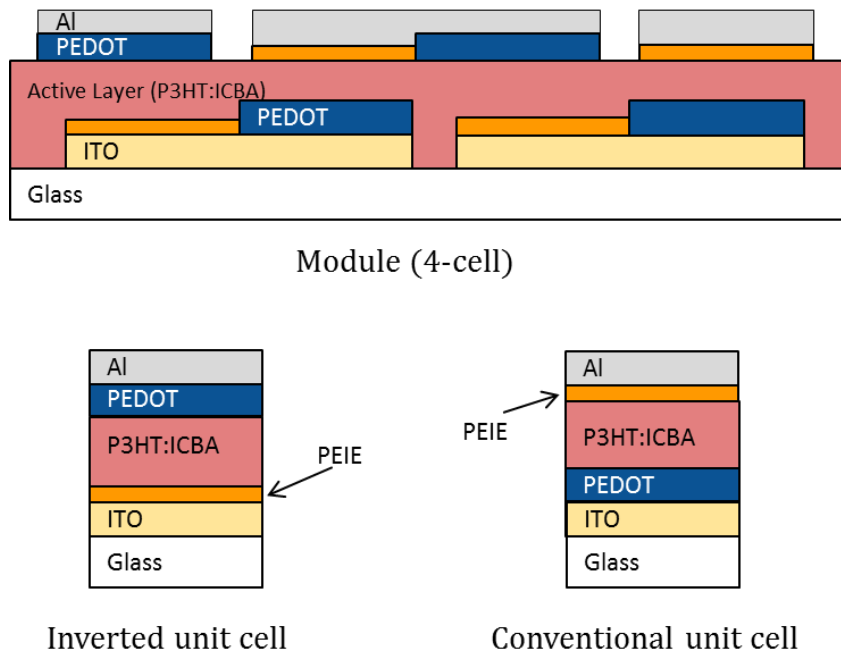


Figure 4-8: Schematic of the new geometry and its constituent inverted and conventional sub-cells for solution processing.

4.3.1 Single Cell Fabrication

First, we tested the single devices with inverted structure and conventional structure which will be assembled in the modules. As shown in Figure 4-8, for the inverted structure, ITO coated with PEIE was used as the electron-collecting electrode [60], and PEDOT:PSS with Al was used as the top electrode for collecting holes. For the conventional structure, TIO coated with PEDOT:PSS was used as hole collecting electrode, while a layer of PEIE between top Al electrode and photoactive layer, lower

the work function of Al and makes this electrode more efficient for electron collecting [99].

We started the fabrication with ITO glass substrates (Colorado Concept Coatings LLC) with a sheet resistivity of c.a. 15 Ω /sq. These substrates were patterned using acid etching and cleaned in sequential ultrasonic baths of detergent in deionized water, deionized water, acetone, and isopropanol. Nitrogen was used to dry the substrates.

For Inverted single cells: PEIE was spin-coated onto ITO substrates from a 0.2 wt.% 2-methoxyethanol solution at a speed of 5000 rpm for 1 min and at an acceleration of 1000 rpm/s and annealed at 120 °C for 10 min on a hot plate in ambient air. The effective thickness of PEIE was 5 nm determined by spectroscopic ellipsometry (J. A. Woollam Co.). Then the substrates were transferred into a N₂-filled glove box. The active layer of P3HT:ICBA (1: 1, weight ratio) was filtered through 0.2- μ m-pore PTFE filters and spin-coated on each substrate from 40 mg/ml dichlorobenzene solution at a speed of 800 rpm for 30 s and an acceleration of 1000 rpm/s. Then the active layers were treated through solvent annealing for 3 hours and thermally annealed at 150 °C for 10 min on a hot plate in the glove box. The thickness of the active layer was 200 nm, measured by spectroscopic ellipsometry (J. A. Woollam Co.). After samples cooled down for 20 min in the glove box, they were transferred in ambient air and treated by O₂ plasma treatment for 1 s to make the surface hydrophilic. Then a layer of PEDOT:PSS HTL Solar was spin-coated on top of the active layer at a speed of 5000 rpm for 1 min and an acceleration of 1000 rpm/s. The thickness of PEDOT:PSS layer was about 40 nm.

For conventional single solar cells: PEDOT:PSS 4083 was spin-coated onto ITO substrates at a speed of 5000 rpm for 1 min and at an acceleration of 1000 rpm/s and

annealed at 120 °C for 10 min on hot plate in ambient air. The thickness of PEDOT:PSS was 40 nm. The P3HT:ICBA active layers were prepared in the same condition as prepared in the inverted single cells. Then a thin layer of PEIE was spin-coated on top of plasma-treated active layer from a weight concentration of 0.04% at a speed of 5000 rpm for 1 min and an acceleration of 1000 rpm/s.

Current density-voltage (J - V) characteristics were measured inside the N_2 -filled glove box by using a source meter (2400, Keithley Instruments, Cleveland, OH) controlled by a LabVIEW program. To test the solar cell properties under illumination, an Oriel lamp with an AM 1.5 filter and an irradiance of 100 mW/cm² was used as the light source.

Measurement results: The inverted single cell devices exhibit good performance under illumination with $V_{OC} = 0.80 \pm 0.01$ V, $J_{SC} = 10.7 \pm 0.1$ mA/cm² and FF = 0.60 ± 0.01, yielding PCE = 5.2 ± 0.1%. The single cells with conventional structure also exhibit comparable performance under illumination with $V_{OC} = 0.83 \pm 0.01$ V, $J_{SC} = 9.4 \pm 0.2$ mA/cm² and FF = 0.59 ± 0.01, yielding PCE = 4.6 ± 0.1%, averaged over 4 devices. These results are summarized in Table 7.

Table 7: PV performance of inverted and conventional single cells under AM 1.5 100 mW/cm² illumination (averaged over 4 devices)

Sample	V_{OC} (V)	J_{SC} (mA/cm ²)	FF	PCE (%)
Inverted single cell	0.80 ± 0.01	11.0 ± 0.2	0.60 ± 0.01	5.3 ± 0.1
Conventional single cell	0.74 ± 0.01	9.3 ± 0.2	0.59 ± 0.01	4.5 ± 0.1

The J - V characteristics of these solution-processed inverted and single cells are shown in Figure 4-9.

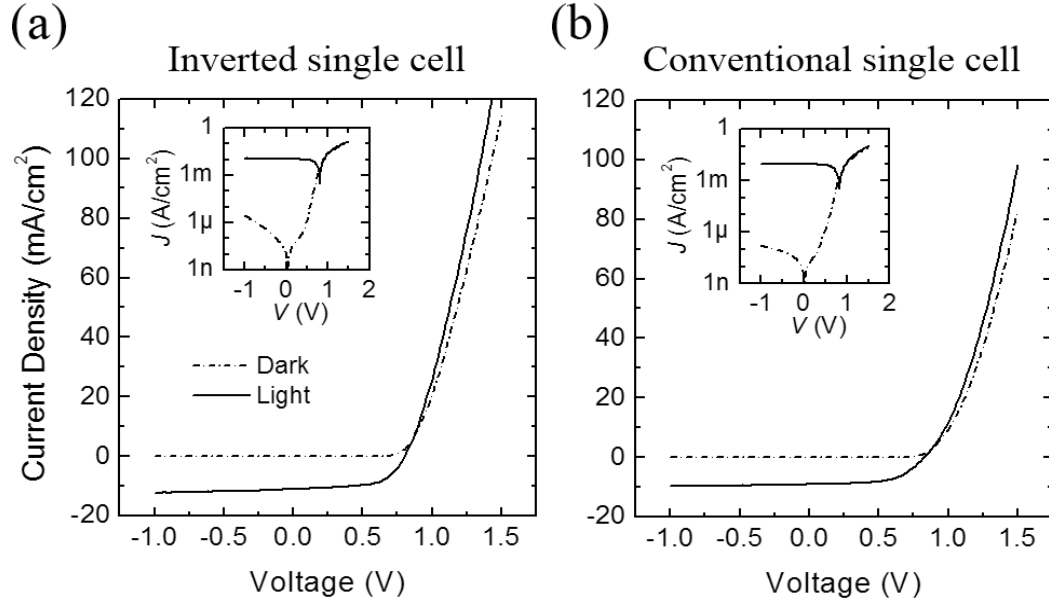


Figure 4-9: J - V characteristic of (a) an inverted single cell (glass/ITO/PEIE/P3HT:ICBA/ PEDOT:PSS/Al) and (b) a conventional single cell (glass/ITO/PEDOT:PSS/P3HT:ICBA/PEIE/Al) in the dark and under AM 1.5 100 mW/cm^2 illumination.

Based on these inverted (ITO/PEIE/P3HT:ICBA/PEDOT:PSS/Al) and conventional (ITO/PEDOT:PSS/P3HT:ICBA/PEIE/Al) solar cell geometries with alternating interlayers, we fabricated a four-cell module.

4.3.2 Four-Cell Module

For the module comprising of four cells with alternating electrical polarity, PEIE (0.2%) and PEDOT:PSS 4083 (CLEVIOUS PVP AL 4083) were spin-coated onto four parts of a patterned ITO substrate at a speed of 5000 rpm for 1 min and at an acceleration

of 1000 rpm/s. Narrow pieces of (0.5-1 mm) polydimethylsiloxane (PDMS) were put down onto the gaps prior to spin-coating of PEIE and PEDOT:PSS to keep PEIE and PEDOT:PSS only covering desired areas on ITO. After spin-coating, the PDMS films were peeled off and the samples were annealed at 120 °C for 10 min on a hot plate in ambient air. The active layers of P3HT:ICBA were prepared in the same condition as for single solar cells. Then a thin layer of PEIE from a weight concentration of 0.04% and a layer of PEDOT:PSS HTL Solar (CLEVIOS HTL Solar) were spin-coated on top of the plasma-treated active layer at a speed of 5000 rpm for 1 min and an acceleration of 1000 rpm/s. Prior to spin-coating, narrow pieces of PDMS films were put down on the active layer to separate the PEIE and PEDOT:PSS areas and to prevent intermixing during spin-coating.

All the samples were transferred into a N₂-filled glove box and annealed on a hot plate at 110 °C for 10 min to dry PEIE and PEDOT:PSS. Then, the samples were loaded into a vacuum thermal evaporation system (SPECTROS, Kurt J. Lesker) and a layer of Al (150 nm) was deposited onto all of the samples through a shadow mask. Area of module devices was 12 mm² not including the gap between the ITO electrodes.

Finally, the current density-voltage (*J-V*) characteristics were measured inside the N₂-filled glove box by using a source meter (2400, Keithley Instruments, Cleveland, OH) controlled by a LabVIEW program. To test the solar cell properties under illumination, an Oriel lamp with an AM 1.5 filter and an irradiance of 100 mW/cm² was used as the light source.

Figure 4-10 shows the *J-V* characteristics of a four-cell module. In the dark, the module shows very small reverse current. Under illumination, the module exhibits $V_{OC} =$

3.18 V, $J_{SC} = 2.3 \text{ mA/cm}^2$, $FF = 0.70$, and $PCE = 5.1\%$. It's should be noted that the gap areas between the cells without electrodes is not considered for current density and PCE calculation.

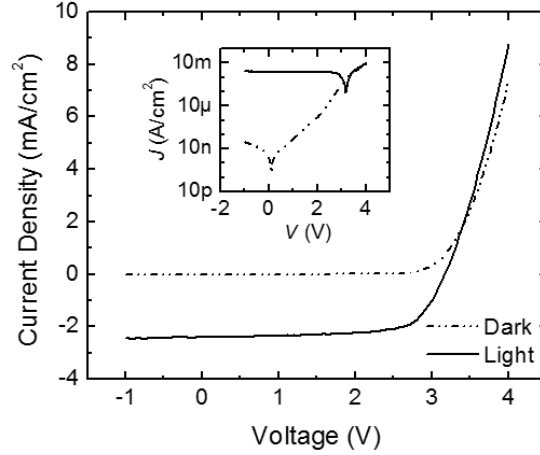


Figure 4-10: J - V characteristic of the solution processed four-cell module the in dark and under AM 1.5 100 mW/cm^2 illumination.

The V_{OC} of the module is close to the sum of the four single cells. The high PCE of the module is mainly attributed to its large FF, larger than the both conventional and inverted single cells. The summary of the results is shown in Table 8.

Table 8: Photovoltaic performance of solution processed four-cell module, and its inverted and conventional sub-cells, under AM 1.5 100 mW/cm^2 illumination.

Sample	V_{OC} (V)	J_{SC} (mA/cm ²)	FF	PCE (%)
Inverted single cell	0.80 ± 0.01	10.7 ± 0.2	0.60 ± 0.01	5.2 ± 0.1
Conventional single cell	0.83 ± 0.01	9.4 ± 0.2	0.59 ± 0.01	4.6 ± 0.1
Four-cell module	3.18	2.3	0.7	5.1

These results, once again, show that in this new geometry, the FF of the module is equal or higher than the FF of its sub-cells, which in turn result in a module PCE with values comparable to the PCE of the sub-cells. Having this successful solution processed module, in the next trial we modified the recipes for scalable fabrication methods.

4.4 Trial 4: OPV Module: Inkjet Printing

As it was previously discussed in details (section 2.3.2 Scalable Fabrication: Printed Electronics), inkjet printing is a “mask-less” and “non-contact” deposition technique that offers accurate deposition of wide range of organic materials for large-area and low cost electronic manufacturing.

In an attempt to investigate the scalability of the proposed module design, we decided to utilize an inkjet printer to assemble the new OPV module. For this trial, we used a Fuji Dimatix DMP-2831 printer. This printer was equipped with 16-nozzle cartridges with a typical drop size (volume) of 10 pl/drop per nozzle. To print the organic materials one first needs to formulate and optimize the organic material into a jet-able (print-able) solutions, or so-called “inks.”

4.4.1 PEDOT Ink Formulation

PEDOT is built from ethylenedioxythiophene (EDOT) monomers which are insoluble in many common solvents and rapidly oxidize in air, thus are unstable in their neutral state. To improve the processability, usually a polysulfonate solution (PSS) is added, and this results in an aqueous dispersion of Poly(3,4-ethylenedioxythiophene)

Polystyrene sulfonate, where PEDOT is in its oxidized state [101, 102]. This combination is referred to as PEDOT:PSS (Figure 4-11).

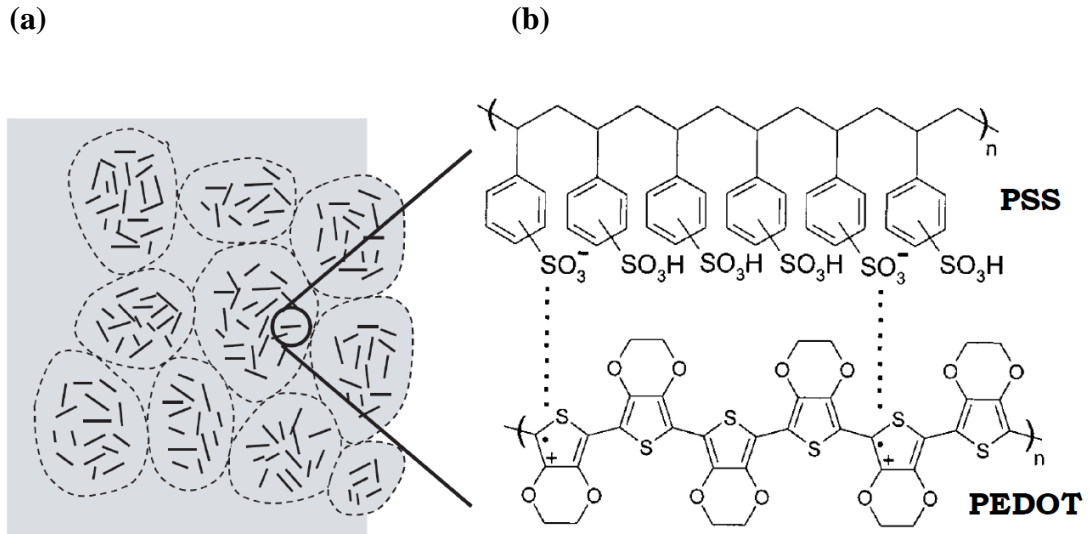


Figure 4-11: Schematic of (a) the morphology of a typical PEDOT:PSS thin-film, where PEDOT particles are shown as solid short lines, surrounded by PSS-rich surface layers (dashed lines), and (b) the chemical structure of PEDOT and PSS chains. (adopted from [101])

This aqueous dispersion of PEDOT:PSS has been widely used in variety of organic PV and organic light-emitting diodes (OLED) [101]. PEDOT/PSS can serve several key roles such as planarization of ITO surface, improving the wetting properties of the substrate for subsequent organic layer depositions, and increasing the contact work function to facilitate hole injection [83, 103].

In terms of processing, PEDOT:PSS films are mainly formed using spin-coating. Although spin-coating offers a very good control over the thickness and uniformity of the film, this technique is not quite compatible with large-area electronics manufacturing.

Therefore due to its unique offerings and applications in OPV devices, it is of great importance to enable PEDOT:PSS in high throughput manufacturing techniques for large-area electronics, such as printing.

PEDOT:PSS and PEIE layers are the two critical interlayers in the proposed OPV module. Therefore, to realize an inkjet printed OPV module, we needed to formulate PEDOT:PSS ink first. Commercially available PEDOT:PSS solutions are typically aqueous dispersions, and hold certain surface tensions and viscosity values that are not quite compatible with printing techniques. A large number of reports have been published in which researcher tried to modify these properties of PEDOT:PSS by mixing it with other additives such surfactants (compounds that lower the surface tension between two liquids or between a liquid and a solid) and solvents [104, 105] to turn it into an “ink.” However most of these reports are printer-specific and cannot be generalized for other printer. Therefore an in-house recipe needed to be developed.

To be able to print an ink, it must have a specific viscosity and surface tension that is determined by the specifications of the inkjet printer itself. Dimatix DMP-2831 inkjet printer requires inks to have a viscosity between 10-12 mPa.s, a surface tension between 30-35 mN/m, and a density of 1 gr/cm³.

The PEDOT:PSS (1:2.5 by weight) we used in this study was PH-1000 (CLEVIOS Heraeus), an aqueous dispersion with maximum 1.3 % solid content, with density of 1 g/cm³ (at 20°C), PH of 1.5-2.5 (at 20°C), viscosity of 50 mPa.s, and specific conductivity of 850 S/cm according to the manufacturer specs.

To confirm these values, first we measured a viscosity of 35 mPa.s for our pristine PEDOT:PSS PH1000, using MCR300 rheometer (by Anton Paar), and a surface tension

of 71 mN/m using a contact angle measurement tool (Ramé-hart Model 250). The surface tension vs. viscosity of water, PEDOT:PSS PH1000 and the acceptable range for Dimatix DMP-2831 inkjet printer are shown in Figure 4-12.

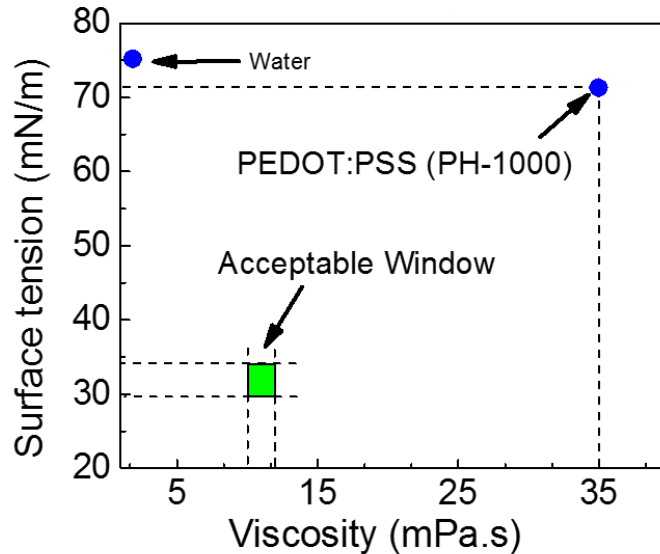


Figure 4-12: Surface tension vs. viscosity of water, PEDOT:PSS PH1000 and the acceptable range of these values for Dimatix DMP-2831 inkjet printer.

As it is evident from the data, PEDOT:PSS solution must be reformulated to have viscosity and surface tension values that are acceptable by this printer. To do so, a number of additives must be mixed with PEDOT:PSS solution. To find the right formulation for printing PEDOT, we used water to reduce the viscosity, and tried a variety of surfactants such as 2,5,8,11 Tetramethyl 6 dodecyn-5,8 Diol Ethoxylate (Dynol 604) and Ethylene glycol butyl ether (EGBE). To improve the conductivity of PEDOT:PSS we tried a number of solvents including Dimethyl sulfoxide (DMSO), Ethylene glycol (EG), and Glycerol. It is suggested that addition of these solvents

increases the conductivity of PEDOT:PSS by thinning of the insulating barrier of PSS surrounding conductive grains of PEDOT [101, 102, 104, 106, 107]. The summary of different solutions along with their measured surface tension and density values are shown in Table 9.

Table 9: List of different modified PEDOT:PSS PH1000 solutions. Water was the main additive to decrease the viscosity, while the surfactants were used to reduce the surface tension, and solvents were used to improve the conductivity of PEDOT:PSS.

No.	Solution	Density (gr/ml)	Surface tension (mN/m)
1	PEDOT:PSS PH1000 (referred to PEDOT for	0.857	63
2	PEDOT:water (1:1)	0.992	64
3	PEDOT:water (2:1)	0.996	67
4	PEDOT:water (1:2)	0.917	66
5	PEDOT + 0.2wt% EGBE	1.014	65
6	PEDOT + 6wt% Glycerol	1.016	69
7	PEDOT + 7wt% EG	1.011	68
8	PEDOT + 5wt% DMSO	0.964	64
9	PEDOT:water (1:1) + 5wt% DMSO	1.016	69
10	PEDOT:water (1:1) + 0.5wt% DMSO + 0.01wt%	0.998	36
11	PEDOT + 0.5wt% DMSO	0.897	65
12	PEDOT:water (1:1) + 0.5wt% DMSO	0.997	70
13	PEDOT:water (1:1) + 0.01wt% DYNOL	1.015	36
14	PEDOT:water (1:1) + 6wt% Glycerol + 0.01wt%	0.992	35
15	PEDOT:water (1:1) + 7wt% EG + 0.01wt% DYNOL	0.992	35
16	PEDOT:water (1:1) + 5wt% DMSO + 0.01wt%	0.992	35

Figure 4-13 shows the viscosity vs. shear graphs for some of the PEDOT:PSS formulations from Table 9.

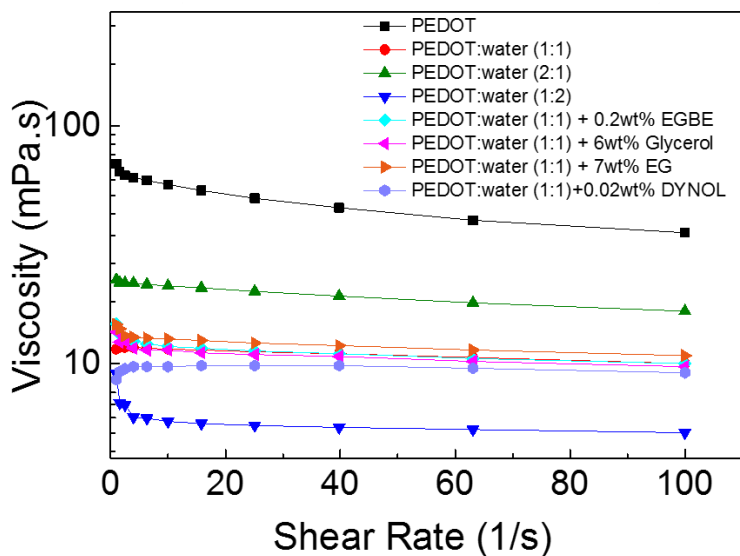


Figure 4-13: Viscosity vs. shear rate for a number of PEDOT:PSS formulations for Dimatix DMP-2831 inkjet printer.

The final PEDOT:PSS formulation was prepared by first making a diluted solution of PEDOT:PSS by adding 1:1 (weight ration) of deionized (DI) water, then adding 7 wt% ethylene glycol. Then a separate solution of 0.2 wt% Dynol in isopropanol was prepared and then 0.01 wt% of this solution (with respect to the ink solution) was added to the PEDOT:PSS solution. This reformulated PEDOT:PSS solution – or ink - had a viscosity of 11 mPa.s (measured by MCR300 rheometer) and surface tension of 35 mN/m (Raméhart Model 250), both perfectly meet the requirements of Dimatix DMP-2831 inkjet printer.

To print, first the PEDOT ink was sonicated for 60 min, then the 10 pl cartridge was filled up with 1.5 ml of the ink. The temperature of the cartridge was set at 28°C and a variety of different printing conditions such as different drop spacing, pulse waveforms, ambient humidity and temperatures were tried. An example of printed PEDOT:PSS patterns are shown in Figure 4-14.

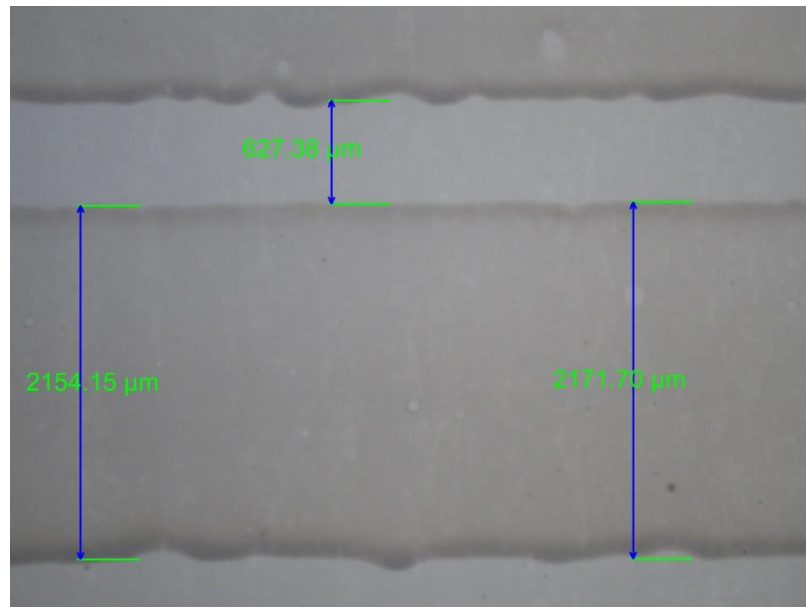


Figure 4-14: An example of a printed PEDOT:PSS pattern on Polyethersulfone (PES) substrate using in-house formulated PEDOT:PSS ink and Dimatix DMP-2831 inkjet printer.

4.4.2 OPV Module with Printed PEDOT:PSS Layer

Using the formulated PEDOT:PSS ink, we modified our four-cell module fabrication process to incorporate interlayers of inkjet printed PEDOT. The schematic of this module is shown in Figure 4-15. Due to resolution limitation of the inkjet printer, we

planned for a module composed of four 5mm by 20 mm sub-cells with 500 μm gaps between them. This design had a total area of 440 mm^2 (400 mm^2 active area).

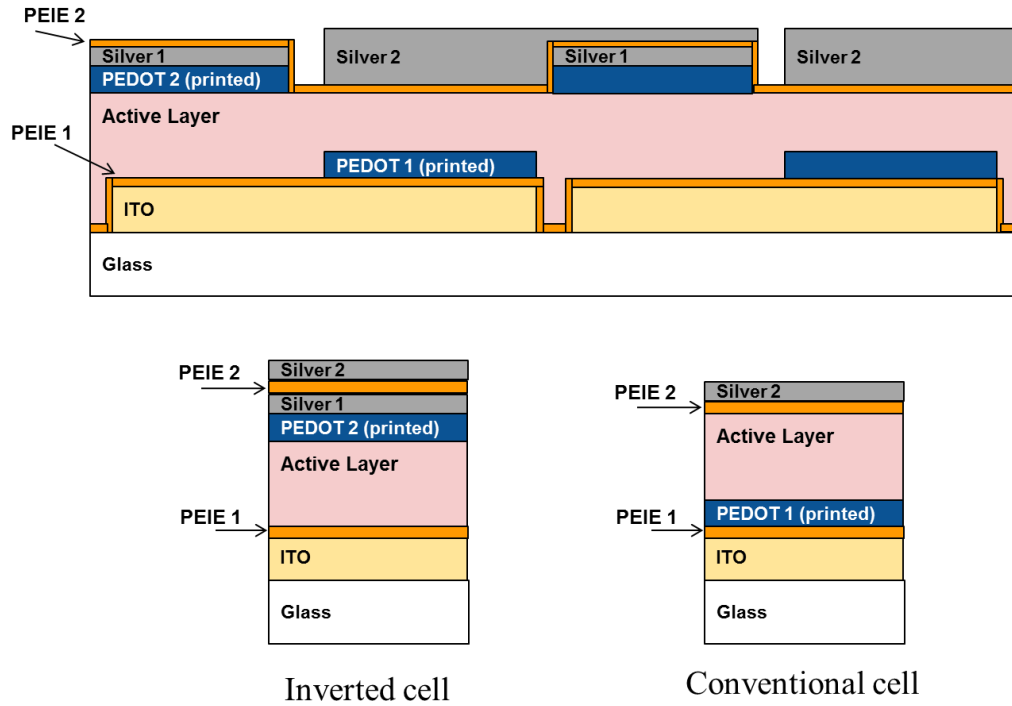


Figure 4-15: Schematic of the modified design of a four-cell module with inkjet printed PEDOT:PSS interlayers, along with its constituent inverted and conventional sub-cells.

As it is shown in Figure 4-15, the PEIE layer in this design was spin-coated. Despite all the effort that we put in formulating PEDOT ink and successful printing of test patterns, the printed PEIE layers had a considerably high thickness ($> 50 \text{ nm}$). This value was much higher than what we needed (approximately 5 nm) and it was hard to

reduce, and due to this reason, several trials of making single cells with printed PEIE failed. Therefore to simplify the design we spin-coated PEIE everywhere.

We started the fabrication by patterning ITO-coated glass (Colorado Concept Coatings LLC) with a sheet resistivity of c.a. $15 \Omega/\text{sq}$. First, 10 nm of Ti, followed by 60 nm of Au were deposited on the substrate through shadow mask to serve as alignment marks. The ITO substrates then were patterned with photolithography and etched inside acid solution (4:2:1 by volume, $\text{HCl}:\text{H}_2\text{O}:\text{HNO}_3$) for 5 min at room temperature. The patterned substrates were cleaned in an ultrasonic bath of detergent water, rinsed with deionized water, and then cleaned in sequential ultrasonic baths of deionized water, acetone, and isopropanol. Nitrogen was used to dry the substrates after each of the last three baths. Then the substrates were treated in a reactive ion etcher (Oxford End-point RIE) for 5 min at 100 W power and 100 sccm O_2 to remove any remaining organic contamination and to improve the surface wettability.

Then Polyethylenimine, 80% ethoxylated (PEIE) ($M_w = 70,000 \text{ g/mol}$) was dissolved in H_2O with a concentration of 35-40 wt.% when received from Aldrich. Then, it was diluted into 2-methoxyethanol to a weight concentration of 0.4 wt.%. Then the PEIE was spin-coated at a speed of 5000 rpm for 1 min and at an acceleration of 1000 rpm/s and annealed at $120 \text{ }^\circ\text{C}$ for 10 min on a hot plate in ambient air. The thickness of PEIE was 5 nm determined by spectroscopic ellipsometry (J. A. Woollam Co., M-2000UI). This PEIE layer was then patterned through a shadow mask in RIE for 3 s at 100 W power and 50 sccm O_2 .

Then using inkjet printer we deposited (printed) a layer of PEDOT:PSS ink. The thickness of PEDOT:PSS layer was about 120 nm measured by a Dektak Profilometer.

The roughness of this film was around 25 nm measured by atomic force microscope (AFM). The thickness of edges was close to 1 μm in most of the areas. The film then was annealed on top of hot-plate in ambient air at 120 $^{\circ}\text{C}$ for 15 min.

Then the substrates were transferred into a N_2 -filled glove box. The active layer of P3HT:ICBA (1: 1, weight ratio) was filtered through 0.2- μm -pore PTFE filters and spin-coated on each substrate from 40 mg/ml dichlorobenzene solution at a speed of 800 rpm for 30 s and an acceleration of 1000 rpm/s. Then the active layers were treated through solvent annealing for 5 hours and thermally annealed at 150 $^{\circ}\text{C}$ for 10 min on a hot plate inside the glove box. The thickness of the active layer is 200 nm, measured by spectroscopic ellipsometry.

Then samples were taken out of the glove-box. Using the inkjet printer we deposited (printed) the PEDOT:PSS layer of top of the photoactive layer. The film then was annealed on top of hot-plate in ambient air at 100 $^{\circ}\text{C}$ for 10 min.

To protect the PEDOT:PSS layer and prevent it from peeling-off during spin-coating of PEIE, due to thickness of the edges and weak adhesion (compare to spin-coating films), first a 50 nm-thick of Al was deposited on top of this printed at a rate of 1 $\text{\AA}/\text{s}$ through shadow mask, using a vacuum thermal evaporation system (PVD-75).

Then, the sample was transferred into RIE for 1 s treatment with O_2 plasma (50 W, 50 sccm O_2) to improve the surface wettability of P3HT:ICBA film. Then, a layer of 0.05 wt.% PEIE in 2-methoxyethanol was spin-coated at a speed of 5000 rpm for 1 min and at an acceleration of 1000 rpm/s and annealed at 100 $^{\circ}\text{C}$ for 10 min on a hot plate.

At the end, using a separate shadow mask, a 100 nm of Ag was deposited on top at a rate of 1 Å/s through shadow mask, using a vacuum thermal evaporation system (PVD-75). Also Figure 4-16 shows a picture of the final device.

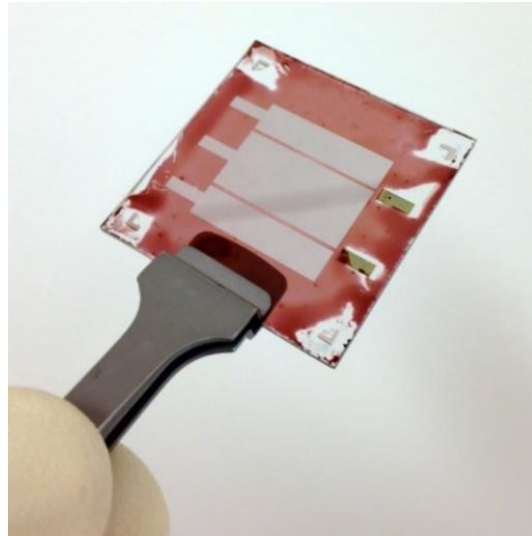


Figure 4-16: Picture of the four-cell module with printed PEDOT:PSS interlayers on glass.

Current density-voltage (J - V) characteristics were measured inside the N_2 -filled glove box by using a source meter (2400, Keithley Instruments, Cleveland, OH) controlled by a LabVIEW program. To test the solar cell properties under illumination, an Oriel lamp with an AM 1.5 filter and an irradiance of 100 mW/cm^2 was used as the light source.

Under illumination, the module exhibits $V_{OC} = 3.11 \text{ V}$, total area $J_{SC} = 0.95 \text{ mA/cm}^2$ (active area $J_{SC} = 1.05 \text{ mA/cm}^2$), $FF = 0.29$, and 0.89% module total area

efficiency (0.98% active area efficiency). Figure 4-17 shows the J - V characteristics of this four-cell module.

Measurement results show that the V_{OC} of the four-cell module is equal to the sum of the V_{OC} 's of its sub-cells.

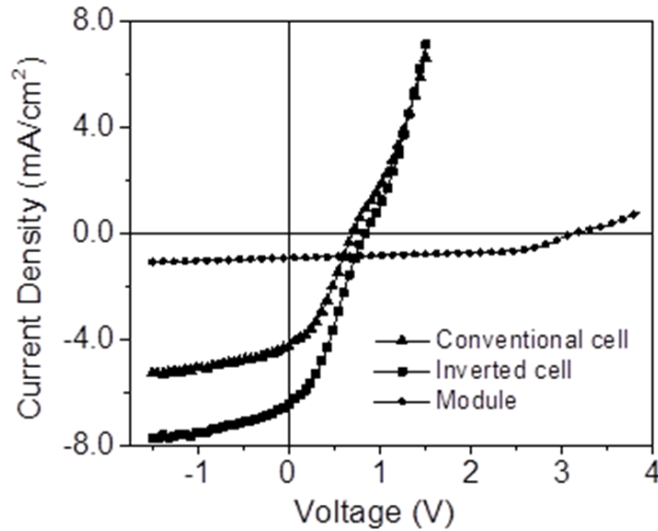


Figure 4-17: J - V characteristics of the printed four-cell module under AM 1.5 100 mW/cm^2 illumination. The active area of the module is 400 mm^2 and the total area is 440 mm^2 (four 5 mm by 20 mm cells, with $500 \mu\text{m}$ gaps between them)

The results are summarized in Table 10.

Table 10: Photovoltaic performance of the four-cell module with its inverted and conventional sub-cells (printed PEDOT:PSS interlayer)

Sample	V_{OC} (V)	J_{SC} (mA/cm^2)	FF	PCE (%)
Inver. single	0.84 ± 0.01	6.3 ± 0.2	0.29 ± 0.01	1.5 ± 0.1
Conv. single	0.71 ± 0.02	4.0 ± 0.1	0.35 ± 0.02	1.0 ± 0.1
Module (total area)	3.11	0.95	0.29	0.88

4.4.3 Discussion

Compared to previous trials, this module displays a low performance for a number of reasons. The *s*-shape *J-V* characteristic of the module and its sub-cells is an indication of poor charge carrier collection at the electrodes. The quality of the printed PEDOT:PSS interlayer is the main reason for this low performance.

First, the high roughness of the printed PEDOT:PSS film can be assigned to its morphology. As it was discussed in the introduction chapter, the morphology of organic films play a critical role in functionality of organic devices. Not to mention that this roughness was more severe at the edges of the printed patterns.

Second, in this trial we could not reduce the thickness of the PEDOT:PSS layer (120 nm), due to the limitation of the printing parameters and conditions, while in other trials the spin-coated PEDOT:PSS layer had a thickness of less than 40 nm. This in turn, reduces the light absorption in the sub-cells, resulting in an overall lower current density values.

Last but not least, the printing and the rest of the processing steps (except deposition of photoactive layer) were performed in air. This could partially affect the performance of the device as well by possible photo oxidation of the active layer for example.

Nonetheless, in this module - despite its low performance values – the V_{OC} was equal to the sum of the V_{OC} values of its sub-cells. Also the FF was equal, but not higher, than the sub-cell with the lowest FF.

These two results illustrates that this module design has the potential and can be used with more scalable techniques such as inkjet printing, however more ink and printing modification is required to improve the quality of the printed layers.

4.5 Trial 5: OPV Module: Reactive Ion Etching (RIE)

In previous trial we utilized solution processing to deposit the films, however for the patterning of PEDOT:PSS and PEIE we used PDMS films. Although these methods served our purpose and resulted in a working module with acceptable performance, the PDMS patterning technique, as we performed it, was not necessarily as easy to control or a scalable method. In this trial we used shadow masking and dry-etching to pattern the PEDOT:PSS and PEIE in the module structure.

Because of using dry-etching to pattern the PEDOT and PEIE layers in this trial, we needed to modify the design. As it is shown in Figure 4-18, in this new design there is an extra PEDOT:PSS layer on top of PEIE layer in sub-cells with conventional structure. This is due to the fact that dry etching of top PEDOT:PSS layer on top of active layer required at least 30 s to 1 min of O₂ plasma. Such a long plasma could definitely remove the PEIE layer also potentially damage the photoactive layer. As a solution to this issue, we patterned the top PEDOT:PSS layer after the deposition of both electrodes.

Also to protect the top electrodes (Ag) from possible damage due to O₂ plasma, we needed to cap the electrodes with a more stable metal, such as gold (not shown here for simplicity). It is worth to mention that we changed the top electrodes from Al to Ag due to the deposition toll (PVD-75 Filament evaporator) issues with Al deposition recipes.

Our previous experience proved that there was no performance differences between devices with top electrodes of Ag vs. Al [99].

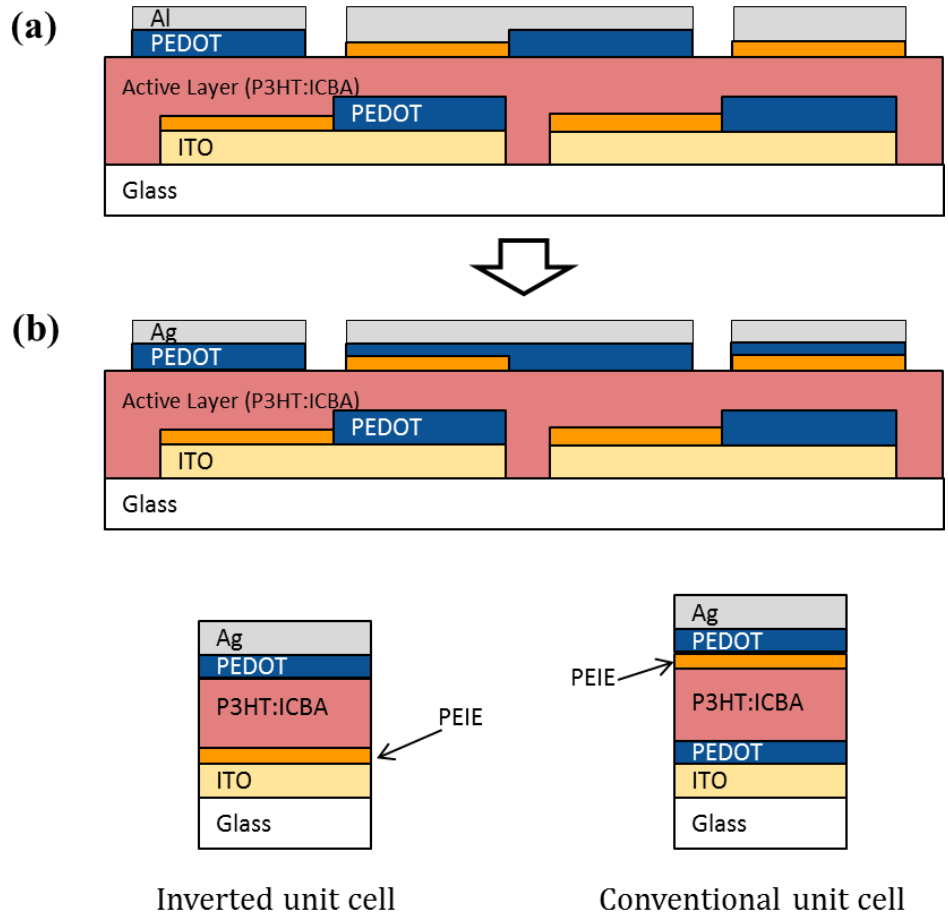


Figure 4-18: Schematic of the new geometry four-cell module and its inverted and conventional sub-cells for scalable fabrication.

4.5.1 Single Cell Fabrication

Before fabricating the module, and to examine the effect of extra PEDOT:PSS layer in conventional structure, we fabricated and optimized a set of single-cell devices with inverted and conventional structures. For the inverted structure (Figure 4-18) the fabrication steps were the same as what we did for solution processed module (section 4.3.1), except here we deposited 150-nm thick layer of Ag as the top electrodes.

For fabrication of the conventional cells, after deposition of the PEIE layer on top of P3HT:ICBA layer, a layer of PEDOT:PSS (Heraeus CLEVIOS P CPP105D) was spin-coated at a speed of 5000 rpm for 1 min and an acceleration of 1000 rpm/s. The thickness of PEDOT:PSS layer was about 40 nm, and finally we deposited 150 nm-thick layer of Ag as the top electrode.

Current density-voltage (J - V) characteristics were measured inside the N_2 -filled glove box by using a source meter (2400, Keithley Instruments, Cleveland, OH) controlled by a LabVIEW program. To test the solar cell properties under illumination, an Oriel lamp with an AM 1.5 filter and an irradiance of 100 mW/cm^2 was used as the light source.

In this test trial, the conventional devices exhibit good performance with $V_{OC} = 0.79 \pm 0.01 \text{ V}$, $J_{SC} = 10.35 \pm 0.27 \text{ mA/cm}^2$ and $FF = 0.60 \pm 0.01$, yielding $PCE = 5.05 \pm 0.11\%$, averaged over 6 devices. The inverted devices exhibit good performance with $V_{OC} = 0.82 \pm 0.01 \text{ V}$, $J_{SC} = 8.63 \pm 0.18 \text{ mA/cm}^2$ and $FF = 0.58 \pm 0.01$, yielding $PCE = 4.10 \pm 0.08\%$, averaged over 6 devices. These measurement results are summarized in Table 11

and the J - V characteristics of both conventional and inverted cells are shown in Figure 4-19.

Table 11: Photovoltaic performance of inverted and conventional single cells under AM 1.5 100 mW/cm² illumination. (averaged over 6 devices)

Sample	V_{OC} (V)	J_{SC} (mA/cm ²)	FF	PCE (%)
Inverted single	0.79 ± 0.01	10.35 ± 0.27	0.60 ± 0.01	5.05 ± 0.11
Conventional single	0.82 ± 0.01	8.63 ± 0.18	0.58 ± 0.01	4.10 ± 0.08

As it is evident from the results, the performance of these single cell devices is very much similar to the result of solution processed single cell devices (see Table 7).

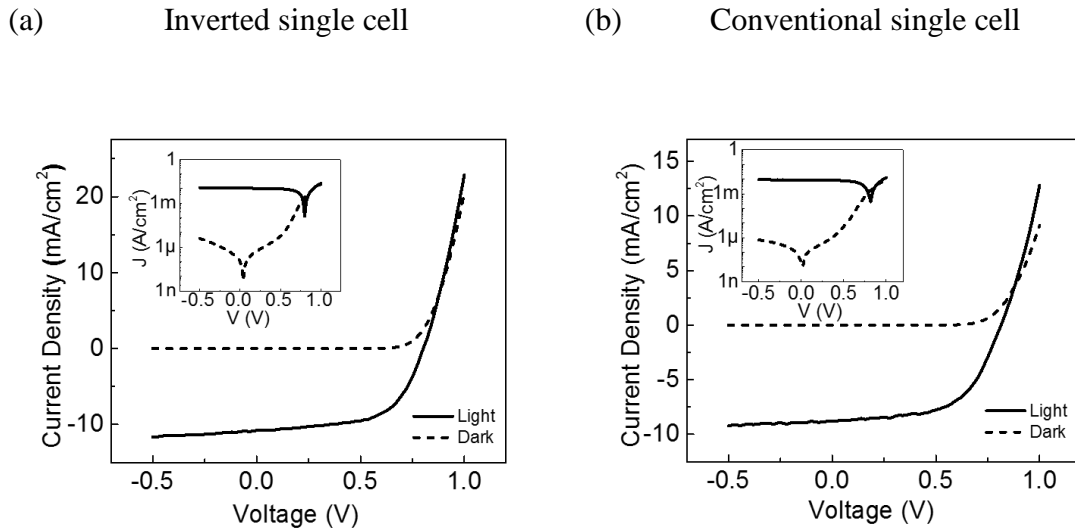


Figure 4-19: J - V characteristic of (a) an inverted single solar cell (glass/ITO/PEIE/P3HT:ICBA/ PEDOT:PSS/Ag) and (b) a conventional solar cell (glass/ITO/PEDOT:PSS/P3HT:ICBA/PEIE/PEDOT:PSS/Ag) in the dark and under AM 1.5 100 mW/cm² illumination.

To put in test the scalability of this method, next we designed and fabricated a four-cell and an eight-cell module.

4.5.2 Four-Cell Module

We first designed and fabricated a four-cell module with total area of 90 mm² (80 mm² active area) where the sub-cells were 2 mm by 10 mm large, with 500 μm gaps between them.

An ITO-coated glass (Colorado Concept Coatings LLC) with a sheet resistivity of c.a. 15 Ω/sq. was used as substrate. First, 10 nm of Ti, followed by 60 nm of Au were deposited on the substrate through shadow mask to serve as alignment marks. The ITO substrates then were patterned with photolithography and etched inside acid solution (4:2:1 by volume, HCl:H₂O:HNO₃) for 5 min at room temperature. The patterned substrates were cleaned in an ultrasonic bath of detergent water, rinsed with deionized water, and then cleaned in sequential ultrasonic baths of deionized water, acetone, and isopropanol. Nitrogen was used to dry the substrates after each of the last three baths. Then the substrates were treated in a reactive ion etcher (Oxford End-point RIE) for 5 min at 100 W power and 100 sccm O₂ to remove any remaining organic contamination and to improve the surface wettability.

Then a layer of PEDOT:PSS with 5 wt% dimethyl sulfoxide (DMSO) was spin-coated on top of the patterned ITO at a speed of 5000 rpm for 1 min and an acceleration of 1000 rpm/s. The thickness of PEDOT:PSS layer was about 40 nm. The film was then annealed on top of hot-plate in ambient air at 120 °C for 15 min. The PEDOT:PSS layer

was then patterned through a shadow mask in RIE for 1 min at 100 W power and 100 sccm O₂.

Polyethylenimine, 80% ethoxylated (PEIE) ($M_w = 70,000$ g/mol) was dissolved in H₂O with a concentration of 35-40 wt.% when received from Aldrich. Then, it was diluted into 2-methoxyethanol to a weight concentration of 0.4 wt.%. Then the PEIE was spin-coated at a speed of 5000 rpm for 1 min and at an acceleration of 1000 rpm/s and annealed at 120 °C for 10 min on a hot plate in ambient air. The thickness of PEIE was 5 nm determined by spectroscopic ellipsometry (J. A. Woollam Co., M-2000UI). This PEIE layer was then patterned through a shadow mask in RIE for 3 s at 100 W power and 50 sccm O₂.

Then the substrates were transferred into a N₂-filled glove box. The active layer of P3HT:ICBA (1: 1, weight ratio) was filtered through 0.2- μ m-pore PTFE filters and spin-coated on each substrate from 40 mg/ml dichlorobenzene solution at a speed of 800 rpm for 30 s and an acceleration of 1000 rpm/s. Then the active layers were treated through solvent annealing for 5 hours and thermally annealed at 150 °C for 10 min on a hot plate inside the glove box. The thickness of the active layer is 200 nm, measured by spectroscopic ellipsometry.

After samples cooled down for 30 min in the glove box, they were transferred into RIE for 1 s treatment with O₂ plasma (50 W, 50 sccm O₂) through a shadow mask to improve the surface wettability of P3HT:ICBA film. Then, samples were transferred in to the N₂-filled glove box and a layer of 0.05 wt% PEIE in 2-methoxyethanol was spin-coated at a speed of 5000 rpm for 1 min and at an acceleration of 1000 rpm/s and annealed at 120 °C for 10 min on a hot plate.

Then a layer of PEDOT:PSS (Heraeus CLEVIOS P CPP105D) was spin-coated on top of the active layer at a speed of 5000 rpm for 1 min and an acceleration of 1000 rpm/s. The thickness of PEDOT:PSS layer was about 40 nm. After drying in ambient air at room temperature, then the substrates were transferred to N₂ filled glove box and annealed at 120°C on hot plate for 10 min.

Then a 150 nm of Ag followed by a 50 nm of Au was deposited on top of the PEDOT layer at a rate of 1 Å/s through shadow mask, using a vacuum thermal evaporation system (PVD-75). The substrates then were transferred into RIE and treated for 1 min of dry etching at 100 W power and 100 sccm O₂. The Au layer was deposited to cover and protect the Ag electrodes from O₂ dry etching. This last step of dry etching was necessary to pattern the top PEDOT:PSS layer.

All the major steps of this fabrication process is summarized in Figure 4-20.

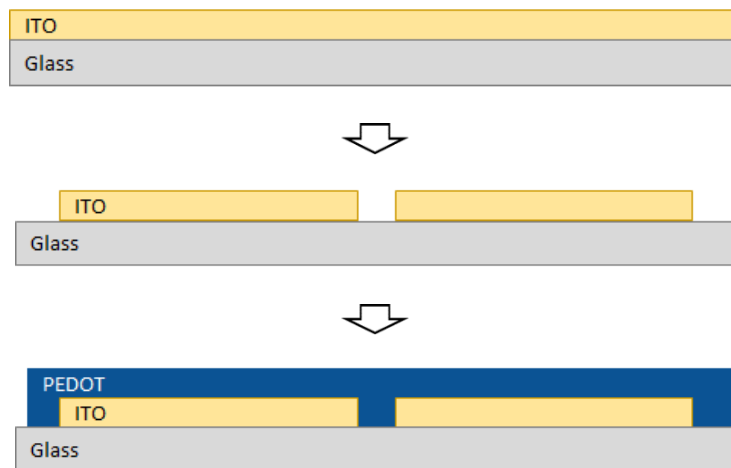


Figure 4-20: Illustration of major fabrication steps for four-cell and eight-cell OPV module

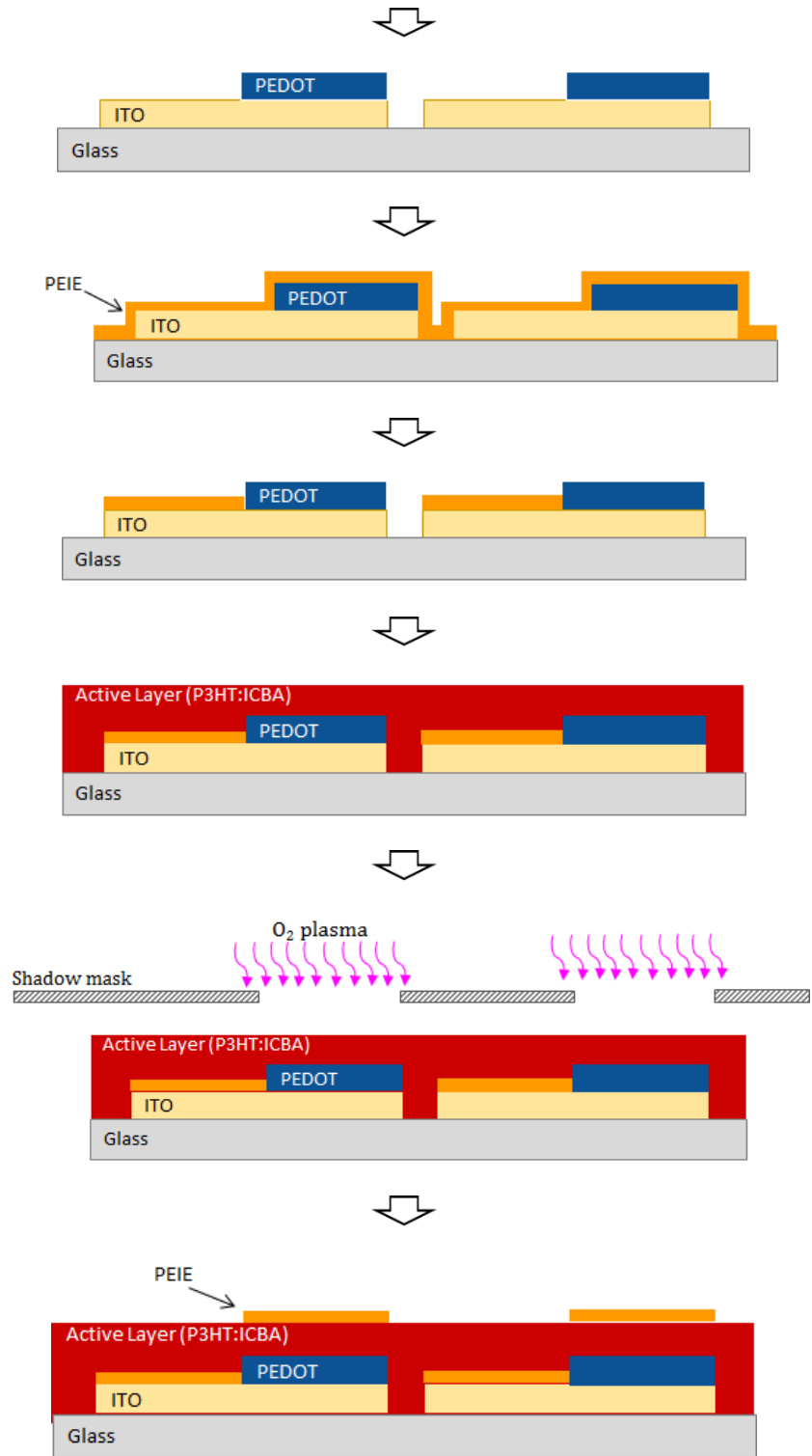
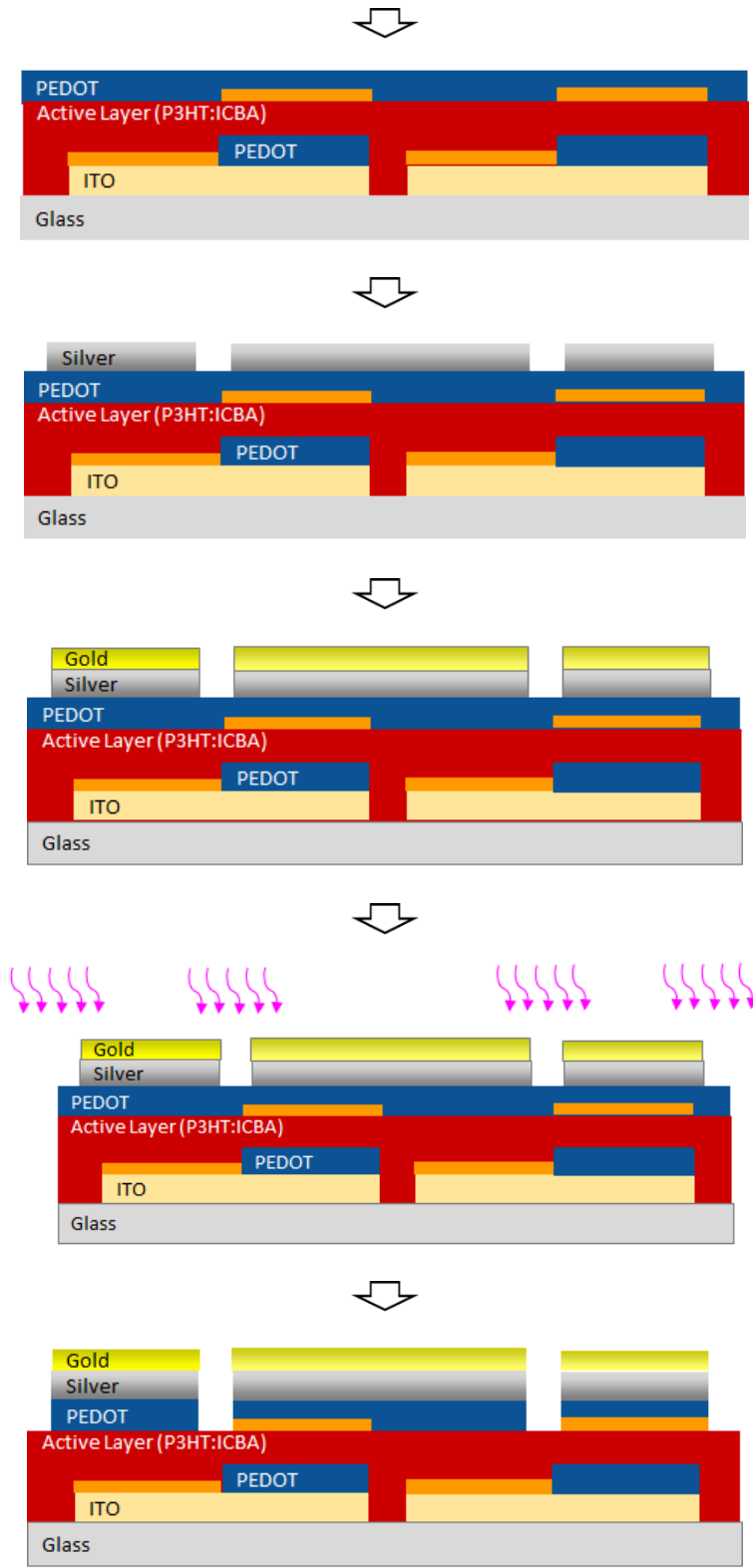


Figure 4-20 (continued)



Module (4-cell)

Figure 4-20 (continued)

Also Figure 4-21 shows a picture of the final device.



Figure 4-21: Picture of the four-cell module fabricated on a glass substrate.

Current density-voltage (J - V) characteristics were measured inside the N_2 -filled glove box by using a source meter (2400, Keithley Instruments, Cleveland, OH) controlled by a LabVIEW program. To test the solar cell properties under illumination, an Oriel lamp with an AM 1.5 filter and an irradiance of 100 mW/cm^2 was used as the light source.

Under illumination, the module exhibits $V_{OC} = 3.15 \text{ V}$, total area $J_{SC} = 2.04 \text{ mA/cm}^2$ (active area $J_{SC} = 2.30 \text{ mA/cm}^2$), $FF = 0.69$, and 4.44% module total area efficiency (5.01% active area efficiency). Figure 4-22 shows the J - V characteristics of this four-cell module.

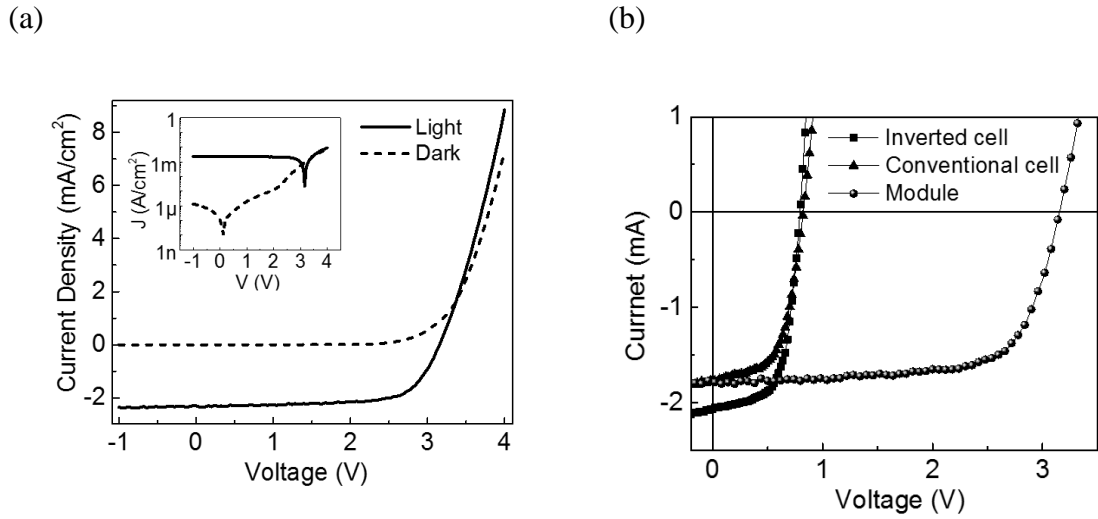


Figure 4-22: (a) J - V characteristics of a four-cell module in the dark and under AM 1.5 100 mW/cm^2 illumination. Inset displays the J - V characteristics of the module in the dark and under AM1.5 100 mW/cm^2 illumination in semi logarithmic scale. (b) I - V characteristics of inverted and conventional sub-cells and the four-cell module under illumination. The active area of the module is 80 mm^2 and the total area is 90 mm^2 (four 2 mm by 10 mm cells, with $500 \text{ }\mu\text{m}$ gaps between them)

Measurement results show that the V_{OC} of the four-cell module is equal to the sum of the V_{OC} 's of its sub-cells. These results are summarized in Table 12. More importantly the FF of the module is better than the FF of both its inverted and conventional sub-cells. This high FF could be attributed to the high V_{OC} of this module and the shape of the J - V curve. Due to such a high FF, this module also gives a considerably high PCE.

Table 12: PV performance of the four-cell module and its inverted and conventional sub-cells under AM 1.5 100 mW/cm^2 illumination

Sample	V_{OC} (V)	J_{SC} (mA/cm^2)	FF	PCE (%)
Inverted single	0.80 ± 0.01	10.50 ± 0.27	0.60 ± 0.01	5.16 ± 0.01
Conventional single	0.82 ± 0.01	8.83 ± 0.06	0.57 ± 0.01	4.17 ± 0.03
Module (active area)	3.15	2.30	0.69	5.01
Module (total area)	3.15	2.04	0.69	4.44

Shown in Table 12 are the “active area” and “total area” efficiency values. As it is shown, the active area efficiency of this module is similar to the PCE values of its inverted sub-cell which have a higher PCE than conventional ones. Contribution of the gaps is the main reason for lowering the total area efficiency (compare to active area efficiency). Of course in this trial we did not intended to decrease the size of the gap, and stayed in the limitation of shadow-masking method.

4.5.3 Eight-Cell Module

Next, we designed and fabricated an eight-cell module with total area of 180 mm² (160 mm² active area) where the sub-cells were 2 mm by 10 mm large, with 500 μm gaps between them. The fabrication steps for this eight-cell module was identical to what we did for four-cell module (see section 4.5.2). A picture of this eight-cell module is shown in Figure 4-23.

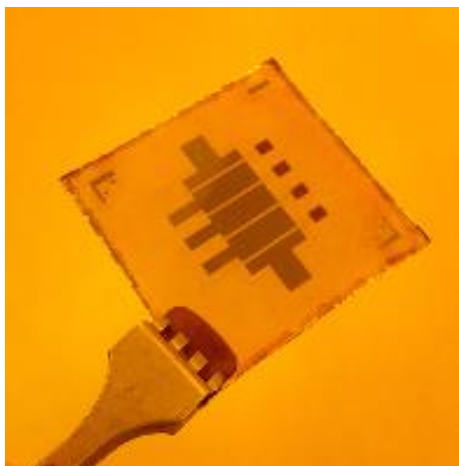


Figure 4-23: Picture of the eight-cell module fabricated on a glass substrate.

Under illumination (AM 1.5, and irradiance of 100 mW/cm^2), the module exhibits $V_{OC} = 6.39 \text{ V}$, total area $J_{SC} = 1.07 \text{ mA/cm}^2$ (active area $J_{SC} = 1.20 \text{ mA/cm}^2$), $FF = 0.63$, and 4.31% module total area efficiency (5.06% active area efficiency). Figure 4-24-a shows the J - V characteristic of this eight-cell module in the dark and under illumination (AM 1.5 100 mW/cm^2). Figure 4-24-b also shows the I - V characteristic of the modules and its sub-cells under illumination.

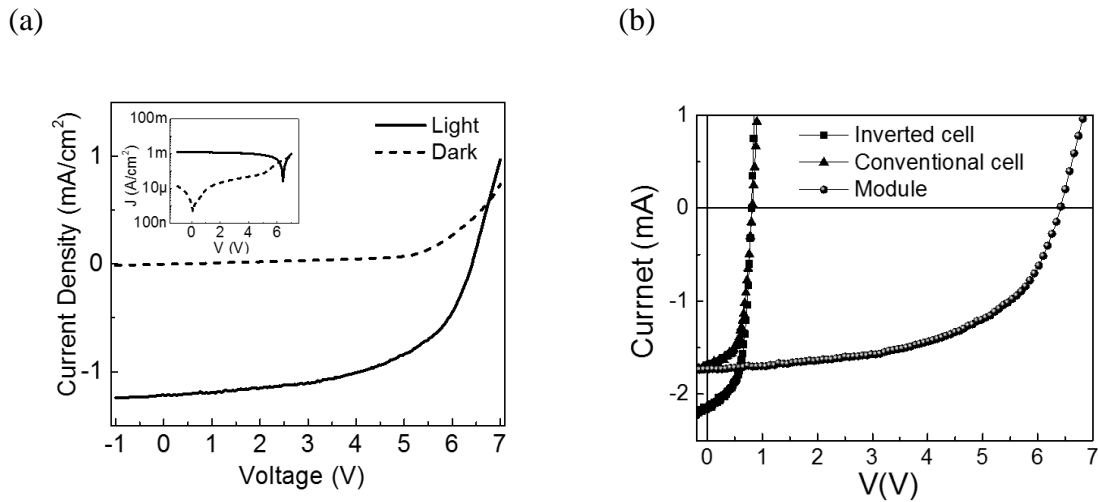


Figure 4-24: (a) J - V characteristics of an eight-cell module in the dark and under AM 1.5 100 mW/cm^2 illumination. Inset displays the J - V characteristics of the module in the dark and under AM1.5 100 mW/cm^2 illumination in semi logarithmic scale. (b) I - V characteristics of inverted and conventional sub-cells and the eight-cell module under illumination. The active area of the module is 160 mm^2 and the total area is 180 mm^2 (eight 2 mm by 10 mm cells, with $500 \text{ }\mu\text{m}$ gaps between them)

Measurement results show that the V_{OC} of the eight-cell module is equal to the sum of the V_{OC} 's of its sub-cells. These results are summarized in Table 13. Similar to four-

cell module, here the FF of the eight-cell module is higher than the FF of both its inverted and conventional sub-cells. These high FF results in a considerably high PCE for this eight-cell module with respect to PCE of its sub-cells.

Table 13: PV performance of the eight-cell module and its inverted and conventional sub-cells under AM 1.5 100 mW/cm² illumination.

Sample	V_{OC} (V)	J_{SC} (mA/cm ²)	FF	PCE (%)
Inverted single	0.78 ± 0.01	10.26 ± 0.38	0.60 ± 0.01	5.01 ± 0.08
Conventional single	0.81 ± 0.02	8.53 ± 0.13	0.58 ± 0.01	4.06 ± 0.07
Module (active area)	6.39	1.20	0.69	5.06
Module (total area)	6.39	1.07	0.69	4.31

As it is evident from data in Table 13, the “total area” efficiency (4.31%) is lower than the active area efficiency (5.06) due to contribution of the gaps. The size of the gap (500 μm) is in the limitation of shadow-masking method and we did not intend to reduce that due to possibility of misalignment and shorting of cells.

4.5.4 Discussion

In both cases The V_{OC} of each module is equal to the sum of the V_{OC} ’s of its sub-cells. Using the J - V characteristics to calculate the shunt and series resistances of each module, the 4-cell module shows a shunt resistance $R_{sh} = 705 \text{ k}\Omega.\text{cm}^2$ and a series resistance $R_s = 240 \text{ }\Omega.\text{cm}^2$, and the 8-cell module shows a shunt resistance $R_{sh} = 68 \text{ k}\Omega.\text{cm}^2$ and a series resistance $R_s = 2.38 \text{ k}\Omega.\text{cm}^2$. Based on these numbers, the shunt resistance decreases and the series resistance increases by one order of magnitude as the module size increases from 4-cell to 8-cell. The large FF of the modules can also be

attributed to the larger V_{OC} of the modules which partially alleviates the effect of series resistance on the overall shape of the J - V characteristics. Besides the effect of FF, the unpatterned photoactive layer in the gap areas potentially could also contribute to the overall module current which in turn could possibly improve the efficiency of the module. These speculations however require further investigations. Table 14 summarizes the performance comparison between our module and state-of-the-art OPV modules in the literature.

Table 14: Performance comparison between current state-of-the-art OPV modules

	Ref.	Single Cell				Module				OPV material used
		J_{sc} (mA/cm ²)	V_{oc} (V)	FF	PCE (%)	J_{sc} (mA/cm ²)	V_{oc} (V)	FF	PCE (%)	
Stripe Geometry	[108]	8.69	0.58	0.63	3.14	0.63	7.97	0.61	3.07	P3HT: PCBM
	[109]	7.61	1.35	0.60	6.12	2.25	3.92	0.65	5.70	OPV12: P ₆₀ CBM & pDPP5T: P ₇₀ CBM (tandem)
Proposed Geometry	[89]*	10.2 (8.9)	0.86 (0.87)	0.56 (0.57)	4.9 (4.5)	1.82	3.48	0.60	3.81 (4.4)	PCDTBT: PC ₇₀ BM
	U _s *	10.5 (8.83)	0.80 (0.82)	0.60 (0.57)	5.16 (4.17)	2.04	3.15	0.69	4.44 (5.0)	P3HT: ICBA

* The first row of data shows the active area values and the second row data shows the module area values.

The majority of OPV module research has been primarily focused on the optimization of the stripe geometry with the goal of reducing power losses introduced by dead-areas and optimizing fabrication methods. Kubis at al. [108], and Spyropoulos at al. [109] each have demonstrated modules with the highest efficiencies reported in the literature as of today. In both demonstrations they have used ITO-silver-ITO films for bottom electrodes to tackle the parasitic resistance, and high-energy ultrafast laser ablation techniques to pattern the layers in an effort to minimize the dead-areas. Although the performance of the reported modules are promising, the methods could have a considerable effect on the levelized cost of energy (LCOE).

On the other hand, modules reported by Lee at al. [89] as well as this demonstration, have been fabricated with much less expensive yet scalable techniques. Also as it was mentioned before the proposed geometry has several advantages over the stripe geometry. As it is shown in Table 14, by taking advantage of surface engineering and work-function tuning, our modules have less structural complexity, yet much better performance metric. The performance of the proposed structure can be further improved by utilizing other surface modifiers, reducing the gap size, optimizing the interlayers, and using more efficient photo-active semiconductors.

CHAPTER 5: CONCLUSION

In conclusion, this work reports on the design, micro-fabrication, and characterization of a state-of-the-art OPV module with a novel design and high performance. This new OPV module geometry can lead to future near-zero loss large-area OPV modules with total area efficiency that is close to efficiency of the sub-cells.

In the reported OPV modules, exclusive patterning of the interlayers allowed for engineering the work function of electrodes, to enable the hole and electron collection in adjacent areas of the same electrode, and resulted in unit cells with alternating electrical polarities where each sub-cell shares electrodes with neighboring cells. This resulted in no need for patterning the active layer, therefore the shading losses become independent of the active area, and interconnection losses are greatly minimized.

We reported on 4-cell and 8-cell modules, based on P3HT:ICBA photoactive material, wherein the measured fill-factors (FF) and PCE of the constituent sub-cells and of the modules are almost identical. The 4-cell module, with a total area of 0.8 cm^2 , exhibits an open-circuit voltage (V_{OC}) of 3.15 V, a short circuit-current density (J_{SC}) of 2.3 mA/cm^2 and a FF of 0.69, yielding a PCE of 5.01%. The 8-cell module, with a total area of 1.6 cm^2 , exhibits a V_{OC} of 6.39 V, a J_{SC} of 1.2 mA/cm^2 and a FF of 0.63, yielding a PCE of 5.06%.

In an effort to move toward a more scalable manufacturing technique, we demonstrated different rounds of fabrication trials, from single cell devices, to proof-of-

concept module, and finally to 4-cell and 8-cell modules with record-high total area efficiency. To put in test the scalability of this new module design, we also formulated and developed PEDOT:PSS ink, developed a recipe and fabricated 4-cell modules with inkjet printed PEDOT:PSS interlayer. Although module with inkjet printed PEDOT:PSS showed lower performance compared to modules with spin-coated PEDOT:PSS, the observation of similar FF and PCE values between modules and sub-cells, is a compelling proof-of-principle that the proposed module design is compatible with all-additive fabrication technique and could lead to OPV modules with unprecedented performance.

5.1 Recommendations for Future Work

5.1.1 Design: Reducing the Gap Size

In the module design demonstrated we did not attempt to reduce the size of the inter-cell gap much below 500 μm in part to stay consistent between different trials and techniques used. Reducing the gap further will increase the “total area” efficiency of the module and, esthetically be very appealing for building integrated photovoltaics, in particular if transparent electrodes were used.

5.1.2 Material: Other Photoactive Materials

In this module, we used P3HT:ICBA as the active area material and achieved performance comparable with the best single cell devices in the literature. However, in recent years the organic photoactive materials have been reported displaying PCE values

larger than 10%. As these, and even more, efficient materials become commercially available (Solarmer's PffBT4T-2OD with 10.8% PCE, and PBDTT-FTTE 10.3% PCE), it would be important to continue to adapt and fine tune the appropriate interfacial materials to demonstrate modules with the proposed new geometry.

5.1.3 Material: Other Interlayers

In this work we used PEIE and PEDOT:PSS as the main interlayers for the solution processed module. High efficiency donor polymer would nonetheless require hole collecting interlayers with larger work function values than PEDOT:PSS. Organic dopant molecules and/or physisorbed polymers leading to surface dipoles that could increase the work function will be necessary to realize high efficiency modules. The wide range of air-stable conductors with low work function values enabled by PEIE or PEI makes it a compelling solution for the electron collecting side. The use of n-dopants should however not be neglected as a possible path towards optimizing the electron collection in OPV modules and could constitute a direction worth looking for future work.

5.1.4 Fabrication Method: Other Printing Methods

Our inkjet printing trial was a very basic attempt to test the scalability of the new module design. This module was composed of at least 7 layers: ITO, PEIE, P3HT:ICBA, PEDOT and top electrode. Develop functional inks of these and other materials need to reach high PCE values and that are suitable to other scalable all additive printing

methods such as gravure printing, slot-die coating, would be a valuable task with a wide impact in the field of printed electronics.

REFERENCES

- [1] J. Phillips, "Determining the sustainability of large-scale photovoltaic solar power plants," *Renewable & Sustainable Energy Reviews*, vol. 27, pp. 435-444, Nov 2013.
- [2] (March 2015). *International Energy Agency Photovoltaic Power Systems Program* [Website]. Available: <http://www.iea-pvps.org/>
- [3] (2015, March 2015). *U.S. Energy Information Administration: International Energy Outlook* [Website]. Available: www.eia.gov
- [4] T. Tsoutsos, N. Frantzeskaki, and V. Gekas, "Environmental impacts from the solar energy technologies," *Energy Policy*, vol. 33, pp. 289-296, Feb 2005.
- [5] A. Cherp and J. Jewell, "The concept of energy security: Beyond the four As," *Energy Policy*, vol. 75, pp. 415-421, Dec 2014.
- [6] A. Goldthau, "Governing global energy: existing approaches and discourses," *Current Opinion in Environmental Sustainability*, vol. 3, pp. 213-217, Sep 2011.
- [7] O. Ellabban, H. Abu-Rub, and F. Blaabjerg, "Renewable energy resources: Current status, future prospects and their enabling technology," *Renewable & Sustainable Energy Reviews*, vol. 39, pp. 748-764, Nov 2014.
- [8] P. Würfel, *Physics of Solar Cells*, 2nd ed. Weinheim, Germany: Wiley-VCH, 2009.
- [9] J. Nelson, *The Physics of Solar Cells*, 1st ed. London, UK: Imperial College Press, 2003.

- [10] S. B. Darling and F. Q. You, "The case for organic photovoltaics," *Rsc Advances*, vol. 3, pp. 17633-17648, 2013.
- [11] E. M. Becquerel, "Memoire sur les effets electriques produits sous L'influence des raynos solaries," *C. R. Acad. Sci.*, vol. 9, pp. 561-567, 1839.
- [12] D. M. Chapin, C. S. Fuller, and G. L. Pearson, "A new silicon p-n junction photocell for converting solar radiation into electrical power," *Journal of Applied Physics*, vol. 25, pp. 676-677, 1954.
- [13] B. Kippelen and J. L. Bredas, "Organic photovoltaics," *Energy & Environmental Science*, vol. 2, pp. 251-261, 2009.
- [14] L. El Char, L. A. Lamont, and N. El Zein, "Review of photovoltaic technologies," *Renewable & Sustainable Energy Reviews*, vol. 15, pp. 2165-2175, Jun 2011.
- [15] M. A. Green, *Solar Cells*, 1st ed. Kensington, NSW: University of New South Wales, 1998.
- [16] B. Y. H. Liu and R. C. Jordan, "The interrelationship and characteristic distribution of direct, diffuse and total solar radiation," *Solar Energy*, vol. 4, pp. 1-19, 1960.
- [17] Thekaeka.Mp, R. Kruger, and C. H. Duncan, "Solar irradiance measurements from a research aircraft," *Applied Optics*, vol. 8, pp. 1713-1732, 1969.
- [18] S. Yoo, B. Domercq, and B. Kippelen, "Intensity-dependent equivalent circuit parameters of organic solar cells based on pentacene and C-60," *Journal of Applied Physics*, vol. 97, May 2005.
- [19] A. Luque and S. Hegedus, *Handbook of Photovoltaic Science and Engineering*, 2nd ed. West Sussex, UK: John Wiley & Sons, 2011.
- [20] (May 2014). *NREL: National Renewable Energy Laboratory* [website]. Available: www.nrel.gov

- [21] M. A. Green, K. Emery, Y. Hishikawa, W. Warta, and E. D. Dunlop, "Solar cell efficiency tables (Version 45)," *Progress in Photovoltaics*, vol. 23, pp. 1-9, Jan 2015.
- [22] X. T. Wang, L. Kurdgelashvili, J. Byrne, and A. Barnett, "The value of module efficiency in lowering the levelized cost of energy of photovoltaic systems," *Renewable & Sustainable Energy Reviews*, vol. 15, pp. 4248-4254, Dec 2011.
- [23] K. Branker, M. J. M. Pathak, and J. M. Pearce, "A review of solar photovoltaic levelized cost of electricity," *Renewable & Sustainable Energy Reviews*, vol. 15, pp. 4470-4482, Dec 2011.
- [24] C. J. Mulligan, C. Bilen, X. J. Zhou, W. J. Belcher, and P. C. Dastoor, "Levelised cost of electricity for organic photovoltaics," *Solar Energy Materials and Solar Cells*, vol. 133, pp. 26-31, Feb 2015.
- [25] K. A. Mazzio and C. K. Luscombe, "The future of organic photovoltaics," *Chemical Society Reviews*, vol. 44, pp. 78-90, 2015.
- [26] S. Zanoni and L. Mazzoldi, *Long Term Analysis of Energy Payback Time for PV Systems* vol. 414, pp. 395-401, 2013.
- [27] E. Alsema, *Energy Payback Time and CO2 Emissions of PV Systems*: Springer, 2012.
- [28] S. H. Sevilgen, H. H. Erdem, B. Cetin, A. V. Akkaya, and A. Dagdas, "Effect of economic parameters on power generation expansion planning," *Energy Conversion and Management*, vol. 46, pp. 1780-1789, Jul 2005.
- [29] (2014, March 2015). *Panasonic HIT® Solar Cell: World's Highest Energy Conversion Efficiency* [Website]. Available: <http://news.panasonic.com/press/news/official.data/data.dir/2014/04/en140410-4/en140410-4.html>
- [30] (2014, March 2015). *Trina Solar: Record high efficiency poly-crystalline silicon solar cell* [Website]. Available: <http://ir.trinasolar.com/phoenix.zhtml?c=206405&p=irol-newsArticle&ID=1990091>

- [31] V. V. Tyagi, N. A. A. Rahim, N. A. Rahim, and J. A. L. Selvaraj, "Progress in solar PV technology: Research and achievement," *Renewable & Sustainable Energy Reviews*, vol. 20, pp. 443-461, Apr 2013.
- [32] J. E. Carle and F. C. Krebs, "Technological status of organic photovoltaics (OPV)," *Solar Energy Materials and Solar Cells*, vol. 119, pp. 309-310, Dec 2013.
- [33] M. Helgesen, J. E. Carle, and F. C. Krebs, "Slot-die coating of a high performance co-polymer in a readily scalable roll process for polymer solar cells," *Advanced Energy Materials*, vol. 3, pp. 1664-1669, Dec 2013.
- [34] G. Li, R. Zhu, and Y. Yang, "Polymer solar cells," *Nature Photonics*, vol. 6, pp. 153-161, Mar 2012.
- [35] N. Kaur, M. Singh, D. Pathak, T. Wagner, and J. M. Nunzi, "Organic materials for photovoltaic applications: Review and mechanism," *Synthetic Metals*, vol. 190, pp. 20-26, Apr 2014.
- [36] T. M. Razykov, C. S. Ferekides, D. Morel, E. Stefanakos, H. S. Ullal, and H. M. Upadhyaya, "Solar photovoltaic electricity: Current status and future prospects," *Solar Energy*, vol. 85, pp. 1580-1608, Aug 2011.
- [37] C. J. Brabec, "Organic photovoltaics: technology and market," *Solar Energy Materials and Solar Cells*, vol. 83, pp. 273-292, Jun 2004.
- [38] H. Klauk, *Organic Electronics: Material, Manufacturing and Applications*, 1st ed. Weinheim, Germany: Wiley-VCH, 2006.
- [39] S.-S. Sun and L. R. Dalton, *Introduction to Organic Electronic and Optoelectronic Materials and Devices*, 1st ed. Boca Raton, FL, USA: CRC Press, 2008.
- [40] H. Hoppe and N. S. Sariciftci, "Organic solar cells: An overview," *Journal of Materials Research*, vol. 19, pp. 1924-1945, Jul 2004.
- [41] C. J. Mulligan, M. Wilson, G. Bryant, B. Vaughan, X. J. Zhou, W. J. Belcher, *et al.*, "A projection of commercial-scale organic photovoltaic module costs," *Solar Energy Materials and Solar Cells*, vol. 120, pp. 9-17, Jan 2014.

- [42] J. Kalowekamo and E. Baker, "Estimating the manufacturing cost of purely organic solar cells," *Solar Energy*, vol. 83, pp. 1224-1231, Aug 2009.
- [43] P. Kopola, T. Aernouts, R. Sliz, S. Guillerez, M. Ylikunnari, D. Cheyns, *et al.*, "Gravure printed flexible organic photovoltaic modules," *Solar Energy Materials and Solar Cells*, vol. 95, pp. 1344-1347, May 2011.
- [44] M. Tuomikoski, P. Kopola, H. Jin, M. Ylikunnari, J. Hiitola-Keinanen, M. Valimaki, *et al.*, "Roll-to-roll manufacturing of organic photovoltaic modules," in *2009 European Microelectronics and Packaging Conference*, ed New York: Ieee, pp. 217-220, 2009.
- [45] D. Kearns and M. Calvin, "Photovoltaic effect and photoconductivity in laminated organic systems," *Journal of Chemical Physics*, vol. 29, pp. 950-951, 1958.
- [46] C. W. Tang, "2-layer organic photovoltaic cell," *Applied Physics Letters*, vol. 48, pp. 183-185, Jan 1986.
- [47] Y.-W. Su, S.-C. Lan, and K.-H. Wei, "Organic photovoltaics," *Materials Today*, vol. 15, pp. 554-562, 2012.
- [48] Z. C. He, C. M. Zhong, S. J. Su, M. Xu, H. B. Wu, and Y. Cao, "Enhanced power-conversion efficiency in polymer solar cells using an inverted device structure," *Nature Photonics*, vol. 6, pp. 591-595, Sep 2012.
- [49] J. B. You, L. T. Dou, K. Yoshimura, T. Kato, K. Ohya, T. Moriarty, *et al.*, "A polymer tandem solar cell with 10.6% power conversion efficiency," *Nature Communications*, vol. 4, pp. 1-10, Feb 2013.
- [50] A. K. K. Kyaw, D. H. Wang, D. Wynands, J. Zhang, T. Q. Nguyen, G. C. Bazan, *et al.*, "Improved Light Harvesting and Improved Efficiency by Insertion of an Optical Spacer (ZnO) in Solution-Processed Small-Molecule Solar Cells," *Nano Letters*, vol. 13, pp. 3796-3801, Aug 2013.
- [51] B. E. Lassiter, J. D. Zimmerman, A. Panda, X. Xiao, and S. R. Forrest, "Tandem organic photovoltaics using both solution and vacuum deposited small molecules," *Applied Physics Letters*, vol. 101, Aug 2012.

- [52] T. R. Andersen, H. E. Dam, B. Andreasen, M. Hosel, M. V. Madsen, S. A. Gevorgyan, *et al.*, "A rational method for developing and testing stable flexible indium- and vacuum-free multilayer tandem polymer solar cells comprising up to twelve roll processed layers," *Solar Energy Materials and Solar Cells*, vol. 120, pp. 735-743, Jan 2014.
- [53] S.-S. Sun and N. S. Sariciftci, *Organic Photovoltaics: Mechanisms, Materials, and Devices*, 1st ed. Boca Raton, FL, USA: CRC Press, 2005.
- [54] J. L. Bredas, "Mind the gap!," *Materials Horizons*, vol. 1, pp. 17-19, Jan 2014.
- [55] D. A. Neamen, *Semiconductor Physics and Devices*, 3rd ed.: McGraw-Hill, 2003.
- [56] V. Coropceanu, J. Cornil, D. A. da Silva, Y. Olivier, R. Silbey, and J. L. Bredas, "Charge transport in organic semiconductors," *Chemical Reviews*, vol. 107, pp. 926-952, Apr 2007.
- [57] C. Deibel and V. Dyakonov, "Polymer-fullerene bulk heterojunction solar cells," *Reports on Progress in Physics*, vol. 73, Sep 2010.
- [58] V. I. Arkhipov, P. Heremans, and H. Bassler, "Why is exciton dissociation so efficient at the interface between a conjugated polymer and an electron acceptor?," *Applied Physics Letters*, vol. 82, pp. 4605-4607, Jun 2003.
- [59] M. Koehler, M. C. Santos, and M. G. E. da Luz, "Positional disorder enhancement of exciton dissociation at donor/acceptor interface," *Journal of Applied Physics*, vol. 99, Mar 2006.
- [60] Y. H. Zhou, C. Fuentes-Hernandez, J. Shim, J. Meyer, A. J. Giordano, H. Li, *et al.*, "A universal method to produce low-work function electrodes for organic electronics," *Science*, vol. 336, pp. 327-332, Apr 20 2012.
- [61] R. G. Little, M. J. Nowlan, K. W. Matthei, and G. Darkazalli, "Low-cost solar module manufacturing," *Solar Energy Materials and Solar Cells*, vol. 47, pp. 251-257, Oct 1997.
- [62] B. Azzopardi, C. J. M. Emmott, A. Urbina, F. C. Krebs, J. Mutale, and J. Nelson, "Economic assessment of solar electricity production from organic-based

photovoltaic modules in a domestic environment," *Energy & Environmental Science*, vol. 4, pp. 3741-3753, Oct 2011.

- [63] Y. Galagan, I. G. de Vries, A. P. Langen, R. Andriessen, W. J. H. Verhees, S. C. Veenstra, *et al.*, "Technology development for roll-to-roll production of organic photovoltaics," *Chemical Engineering and Processing*, vol. 50, pp. 454-461, May-Jun 2011.
- [64] F. C. Krebs, N. Espinosa, M. Hosel, R. R. Sondergaard, and M. Jorgensen, "25th Anniversary Article: Rise to Power - OPV-Based Solar Parks," *Advanced Materials*, vol. 26, pp. 29-39, Jan 2014.
- [65] R. Tipnis, J. Bernkopf, S. J. Jia, J. Krieg, S. Li, M. Storch, *et al.*, "Large-area organic photovoltaic module-Fabrication and performance," *Solar Energy Materials and Solar Cells*, vol. 93, pp. 442-446, Apr 2009.
- [66] (April 2014). *United States Naval Research Laboratory: Vanguard Project* [website]. Available: <http://www.nrl.navy.mil/accomplishments/rockets/vanguard-project/>
- [67] H. K. Lyu, S. Jeong, J. H. Sim, S. Woo, K. P. Kim, J. K. Shin, *et al.*, "Electrical power loss model for large-area monolithic organic photovoltaic module," *Current Applied Physics*, vol. 11, pp. S166-S170, Jan 2011.
- [68] H. K. Lyu, J. H. Sim, S. H. Woo, K. P. Kim, J. K. Shin, and Y. S. Han, "Efficiency enhancement in large-area organic photovoltaic module using theoretical power loss model," *Solar Energy Materials and Solar Cells*, vol. 95, pp. 2380-2383, Aug 2011.
- [69] R. Steim, P. Schilinsky, S. A. Choulis, and C. J. Brabec, "Flexible polymer photovoltaic modules with incorporated organic bypass diodes to address module shading effects," *Solar Energy Materials and Solar Cells*, vol. 93, pp. 1963-1967, Nov 2009.
- [70] S. Choi, W. J. Potscavage, and B. Kippelen, "Area-scaling of organic solar cells," *Journal of Applied Physics*, vol. 106, Sep 2009.
- [71] H. K. Lyu, J. H. Sim, S. Jeong, S. H. Woo, J. K. Shin, and Y. S. Han, "The influence of active cell design on a monolithic organic photovoltaic module:

fabrication and simulation," in *Thin Film Solar Technology Iii*. vol. 8110, L. A. Eldada, Ed., ed Bellingham: Spie-Int Soc Optical Engineering, 2011.

- [72] T. L. Benanti and D. Venkataraman, "Organic solar cells: An overview focusing on active layer morphology," *Photosynthesis Research*, vol. 87, pp. 73-81, Jan 2006.
- [73] G. Li, V. Shrotriya, J. S. Huang, Y. Yao, T. Moriarty, K. Emery, *et al.*, "High-efficiency solution processable polymer photovoltaic cells by self-organization of polymer blends," *Nature Materials*, vol. 4, pp. 864-868, Nov 2005.
- [74] W. L. Ma, C. Y. Yang, X. Gong, K. Lee, and A. J. Heeger, "Thermally stable, efficient polymer solar cells with nanoscale control of the interpenetrating network morphology," *Advanced Functional Materials*, vol. 15, pp. 1617-1622, Oct 2005.
- [75] T. Aernouts, P. Vanlaeke, W. Geens, J. Poortmans, P. Heremans, S. Borghs, *et al.*, "Printable anodes for flexible organic solar cell modules," *Thin Solid Films*, vol. 451, pp. 22-25, Mar 2004.
- [76] S. Yoo, W. J. Potscavage, B. Domercq, J. Kim, J. Holt, and B. Kippelen, "Integrated organic photovoltaic modules with a scalable voltage output," *Applied Physics Letters*, vol. 89, Dec 2006.
- [77] W. J. Potscavage, S. Yoo, B. Domercq, J. Kim, J. Holt, and B. Kippelen, "Integrated organic photovoltaic modules - art. no. 66560R," in *Organic Photovoltaics Viii*. vol. 6656, Z. H. Kafafi and P. A. Lane, Eds., ed Bellingham: Spie-Int Soc Optical Engineering, 2007, pp. R6560-R6560.
- [78] B. Zimmermann, M. Glatthaar, M. Niggemann, M. K. Riede, A. Hirsch, and A. Gombert, "ITO-free wrap through organic solar cells - A module concept for cost-efficient reel-to-reel production," *Solar Energy Materials and Solar Cells*, vol. 91, pp. 374-378, Mar 2007.
- [79] B. Zimmermann, H. F. Schleiermacher, M. Niggemann, and U. Würfel, "ITO-free flexible inverted organic solar cell modules with high fill factor prepared by slot die coating," *Solar Energy Materials and Solar Cells*, vol. 95, pp. 1587-1589, Jul 2011.

- [80] J. Lewis, J. Zhang, and X. M. Jiang, "Fabrication of organic solar array for applications in microelectromechanical systems," *Journal of Renewable and Sustainable Energy*, vol. 1, Jan 2009.
- [81] J. A. Hauch, P. Schilinsky, S. A. Choulis, R. Childers, M. Biele, and C. J. Brabec, "Flexible organic P3HT:PCBM bulk-heterojunction modules with more than 1 year outdoor lifetime," *Solar Energy Materials and Solar Cells*, vol. 92, pp. 727-731, Jul 2008.
- [82] M. Niggemann, B. Zimmermann, J. Haschke, M. Glatthaar, and A. Gombert, "Organic solar cell modules for specific applications - From energy autonomous systems to large area photovoltaics," *Thin Solid Films*, vol. 516, pp. 7181-7187, Aug 2008.
- [83] J. H. Lee, W. S. Chung, N. G. Park, and K. Kim, "Wiper coating method for PEDOT:PSS film on fabricating organic photovoltaic modules," *Current Applied Physics*, vol. 10, pp. E185-E188, Nov 2010.
- [84] J. D. Servaites, S. Yeganeh, T. J. Marks, and M. A. Ratner, "Efficiency enhancement in organic photovoltaic cells: consequences of optimizing series resistance," *Advanced Functional Materials*, vol. 20, pp. 97-104, Jan 2010.
- [85] H. Kim, S. Lee, D. Han, and S. Yoo, "High-density organic photovoltaic modules: Mask-free fabrication using nozzle jet printing and oblique deposition," *Solar Energy Materials and Solar Cells*, vol. 120, pp. 561-565, Jan 2014.
- [86] J. L. Yang, D. Vak, N. Clark, J. Subbiah, W. W. H. Wong, D. J. Jones, *et al.*, "Organic photovoltaic modules fabricated by an industrial gravure printing proofer," *Solar Energy Materials and Solar Cells*, vol. 109, pp. 47-55, Feb 2013.
- [87] K. S. Liao, S. Dias, N. J. Alley, S. D. Yambem, A. Haldar, and S. A. Curran, "Design and fabrication of linear pixel arrays for organic photovoltaic modules to achieve scalable power output," *Thin Solid Films*, vol. 519, pp. 3264-3267, Mar 2011.
- [88] N. S. Kang, B. K. Ju, and J. W. Yu, "Module structure for an organic photovoltaic device," *Solar Energy Materials and Solar Cells*, vol. 116, pp. 219-223, Sep 2013.

- [89] J. Lee, H. Back, J. Kong, H. Kang, S. Song, H. Suh, *et al.*, "Seamless polymer solar cell module architecture built upon self-aligned alternating interfacial layers," *Energy & Environmental Science*, vol. 6, pp. 1152-1157, Apr 2013.
- [90] Y. Aleeva and B. Pignataro, "Recent advances in upscalable wet methods and ink formulations for printed electronics," *Journal of Materials Chemistry C*, vol. 2, pp. 6436-6453, Aug 2014.
- [91] F. C. Krebs, "Fabrication and processing of polymer solar cells: A review of printing and coating techniques," *Solar Energy Materials and Solar Cells*, vol. 93, pp. 394-412, Apr 2009.
- [92] F. C. Krebs, S. A. Gevorgyan, and J. Alstrup, "A roll-to-roll process to flexible polymer solar cells: model studies, manufacture and operational stability studies," *Journal of Materials Chemistry*, vol. 19, pp. 5442-5451, 2009.
- [93] S. E. Shaheen, R. Radspinner, N. Peyghambarian, and G. E. Jabbour, "Fabrication of bulk heterojunction plastic solar cells by screen printing," *Applied Physics Letters*, vol. 79, pp. 2996-2998, Oct 2001.
- [94] H. A. D. Nguyen, C. Lee, and K. H. Shin, "A mathematical model to predict surface roughness and pattern thickness in roll-to-roll gravure printed electronics," *Robotics and Computer-Integrated Manufacturing*, vol. 29, pp. 26-32, Aug 2013.
- [95] L. Gonzalez-Macia, A. Morrin, M. R. Smyth, and A. J. Killard, "Advanced printing and deposition methodologies for the fabrication of biosensors and biodevices," *Analyst*, vol. 135, pp. 845-867, 2010.
- [96] Z. T. Xiong and C. Q. Liu, *The Application of Inkjet Direct Writing in Solar Cell Fabrication: An Overview*. New York: Ieee, 2011.
- [97] B. Kippelen, C. Fuentes-Hernandez, Y. H. Zhou, A. Kahn, J. Meyer, J. Shim, *et al.*, "System and methods for producing low work function electrodes," Patent No.: US 2014/0131868 A1, Published: May 15, 2014, Filed: May 16, 2012.
- [98] J. Halls and J. S. Huang, "Photovoltaic modules," International Patent No.: WO 2011/148176 A2, Published: Dec. 1, 2011, Filed: May 25, 2011.

- [99] T. M. Khan, Y. H. Zhou, A. Dindar, J. W. Shim, C. Fuentes-Hernandez, and B. Kippelen, "Organic photovoltaic cells with stable top metal electrodes modified with polyethylenimine," *Acs Applied Materials & Interfaces*, vol. 6, pp. 6202-6207, May 2014.
- [100] C. Mack, *Fundamental Principles of Optical Lithography: The Science of Microfabrication*: Wiley, 2007.
- [101] M. M. de Kok, M. Buechel, S. I. E. Vulto, P. van de Weijer, E. A. Meulenkaamp, S. de Winter, *et al.*, *Modification of PEDOT:PSS as hole injection layer in polymer LEDs*. Oxford: Blackwell Science Publ, 2006.
- [102] A. M. Nardes, M. Kemerink, M. M. de Kok, E. Vinken, K. Maturova, and R. A. J. Janssen, "Conductivity, work function, and environmental stability of PEDOT : PSS thin films treated with sorbitol," *Organic Electronics*, vol. 9, pp. 727-734, Oct 2008.
- [103] M. P. de Jong, L. J. van Ijzendoorn, and M. J. A. de Voigt, "Stability of the interface between indium-tin-oxide and poly(3,4-ethylenedioxythiophene)/poly(styrenesulfonate) in polymer light-emitting diodes," *Applied Physics Letters*, vol. 77, pp. 2255-2257, Oct 2000.
- [104] A. Keawprajak, W. Koetnuyom, P. Piyakulawat, K. Jiramitmongkon, S. Pratontep, and U. Asawapirom, "Effects of tetramethylene sulfone solvent additives on conductivity of PEDOT:PSS film and performance of polymer photovoltaic cells," *Organic Electronics*, vol. 14, pp. 402-410, Jan 2013.
- [105] O. P. Dimitriev, D. A. Grinko, Y. V. Noskov, N. A. Ogurtsov, and A. A. Pud, "PEDOT:PSS films-Effect of organic solvent additives and annealing on the film conductivity," *Synthetic Metals*, vol. 159, pp. 2237-2239, Nov 2009.
- [106] S. L. Lai, M. Y. Chan, M. K. Fung, C. S. Lee, and S. T. Lee, "Concentration effect of glycerol on the conductivity of PEDOT film and the device performance," *Materials Science and Engineering B-Solid State Materials for Advanced Technology*, vol. 104, pp. 26-30, Nov 2003.
- [107] I. Cruz-Cruz, M. Reyes-Reyes, M. A. Aguilar-Frutis, A. G. Rodriguez, and R. Lopez-Sandoval, "Study of the effect of DMSO concentration on the thickness of the PSS insulating barrier in PEDOT:PSS thin films," *Synthetic Metals*, vol. 160, pp. 1501-1506, Jul 2010.

- [108] P. Kubis, L. Lucera, F. Machui, G. Spyropoulos, J. Cordero, A. Frey, *et al.*, "High precision processing of flexible P3HT/PCBM modules with geometric fill factor over 95%," *Organic Electronics*, vol. 15, pp. 2256-2263, Oct 2014.
- [109] G. D. Spyropoulos, P. Kubis, N. Li, D. Baran, L. Lucera, M. Salvador, *et al.*, "Flexible organic tandem solar modules with 6% efficiency: combining roll-to-roll compatible processing with high geometric fill factors," *Energy & Environmental Science*, vol. 7, pp. 3284-3290, Oct 2014.